Statistical analysis methods for time varying nanoscale imaging problems

Dissertation

zur Erlangung des mathematisch-naturwissenschaftlichen Doktorgrades

"Doctor rerum naturalium"

der Georg-August-Universität Göttingen

im Promotionsprogramm ProPhys

der Georg-August University School of Science (GAUSS)

vorgelegt von

Oskar Laitenberger

aus Tschirtschik

Göttingen, 2018

Betreuungsausschuss

PD Dr. Alexander Egner, Optische Nanoskopie, Laser-Laboratorium Göttingen e.V.

Prof. Dr. Tim Salditt, Institut für Röntgenphysik, Georg-August-Universität Göttingen

Mitglieder der Prüfungskommission

Referent/in: PD Dr. Alexander Egner, Optische Nanoskopie, Laser-Laboratorium Göttingen e.V.

Korreferent/in: Prof. Dr. Tim Salditt, Institut für Röntgenphysik, Georg-August-Universität Göttingen

Weitere Mitglieder der Prüfungskommission:

Prof. Dr. Axel Munk, Institut für Mathematische Stochastik, Georg-August-Universität Göttingen

Dr. Florian Rehfeldt, III. Physikalisches Institut, Georg-August-Universität Göttingen

Prof. Dr. Stefan Jakobs, Abtl. NanoBiophotonik, Max-Planck-Institut für biophysikalische Chemie

Prof. Dr. Claus Ropers, Courant Forschungszentrum Physik, Georg-August-Universität Göttingen

Tag der mündlichen Prüfung: 29.06.2018

Contents

Abstract

Microscopy is an important tool in the life sciences. For a long time its resolution was thought to be fundamentally limited by diffraction as described by Abbe's resolution formula. However, this formula is solely based on diffraction effects. The breakthrough to high-resolution microscopy was accomplished by including optically switchable transitions into the imaging process. Especially transitions between bright and dark states. An important group of high-resolution microscopy techniques switch randomly selected individual molecules into a bright state while all other molecules in their surrounding remain dark. Therefore they are subsumed under the term single molecule switching (SMS) microscopy

This thesis covers qualitative and quantitative aspects of SMS microscopy. The qualitative part deals with the detection and compensation of sample drift which usually occurs within the measurement time of several minutes and may significantly degrade the image quality. The other part deals with the development of quantitative SMS microscopy, hence the counting of molecule numbers.

Because SMS microscopy is based on randomly switching molecules to a bright state and the photophysics of a molecule can be described by a time-discrete Markov chain, statistical methods are excellently suited to analyze and tackle both questions. Here we present two methods and demonstrate their applicability by means of real SMS data: First, a drift correction method, which not only deblures the image, but also specifies the uncertainty of the drift estimate. Second, an extremely general counting model based on a time-discrete Markov chain which can be adaptable to any fluorescent probe and requires neither fluorescence standards nor a priori knowledge of transition rates is presented. In addition, it can determine low and high numbers of molecules, a challenging task that no other method has been able to accomplish so far.

Chapter 1

Introduction

Since the invention of the first microscope, microscopy has established itself as an indispensable tool in the life sciences, because it allows to observe or image an object considerably magnified [1, p. 351]. The magnification allows to resolve structures which are not discernable with the naked eye. However, even at the largest magnification a microscope does not have an arbitrarily high resolution. Ernst Abbe formulated this limit as [2, p. 418-419]

$$\Delta r \approx 0.61 \frac{\lambda_0}{\mathrm{NA}}.$$

Here NA is the numerical aperture of the objective lens and λ_0 is the vacuum wavelength of the light used for imaging. The numerical aperture is a property of the objective lens and characterizes the range of angles over which it can accept or emit light. Abbe formulated the resolution limit by taking into account the diffraction of light inside the microscope's optical system. That is necessary, because diffraction is a fundamental property of propagating waves. In order to achieve highest possible resolution the NA has therefore to be increased to its technically feasible limit. Nowadays this limit amounts to 1.47 using oil immersion lenses. Therefore, the resolution also depends decisively on the chosen wavelength λ_0. This results in a limit of ca. 200 nm for light in the visible spectrum. The obvious way to increase the resolution further is to use shorter wavelengths, as it is the case for instance in electron microscopy or X-ray microscopy [3]. However, the inherently associated high photon energies damage living tissue and can therefore only be employed to a limited extent in life science applications [4].

The emergence of high-resolution optical microscopy therefore closed a gap by facilitating the observation of living samples on the nanometer scale with wavelengths that are mostly harmless. This significant improvement compared to conventional microscopy is achieved by exploiting the photophysical properties of fluorescent probes and has been successfully implemented into numerous high-resolution techniques. However, all these techniques are based on the same basic principle [5]: Fluorescent markers in their bright state can be distinguished from markers in their dark states. The specific technique defines how this distinction, more precisely the switching between these states, is made. Thus, these methods can be roughly divided into two large groups according to their switching

mode: Targeted switching and stochastic switching.

Targeted switching techniques use well-designed light distributions to switch many molecules on and off at predefined locations. Prominent representatives of this group are stimulated emission depletion (STED) [6, 7], ground state depletion (GSD) [8], reversible saturable optical fluorescence transitions (RESOLFT) [9, 10, 11, 12], saturated structured illumination microscopy (SSIM) [13] and saturated patterned excitation microscopy (SPEM) [14]. Stochastic switching techniques, on the other hand, switch randomly selected molecules individually to the bright state while all other molecules in their immediate surrounding populate dark states. Since the location of the bright molecules is not known, they have to be identified, localized and registered. Widely known techniques of this kind are stochastic optical reconstruction microscopy (STORM) [15], direct STORM (dSTORM) [16], ground state depletion microscopy followed by individual molecule return (GSDIM) [17], photoactivated localization microscopy (PALM) [18], PALM with independently running acquisition (PALMIRA) [19] and fluorescence photoactivation localization microscopy (FPALM) [20]. Because this group of techniques is based on switching single molecules we refer to them as SMS (single molecule switching) microscopy. This work deals with both qualitative and quantitative aspects of SMS microscopy.

The qualitative part of this thesis deals with the determination and correction of sample induced movements. Although the time needed for a SMS measurement has been significantly reduced by now it is, in most applications, still in the range of several minutes. Thus uncontrolled movement (drift) of the sample can compromise the resolution of the image. It loses its quality. When we started this work, two methods already addressed this problem: Fiducial marker tracking and cross correlation analysis [21]. The former is laborious to use because additional marking structures have to be incorporated into the sample. The latter detects the drift exclusively on the SMS data, but can only correct for a translational drift. Furthermore, neither of the two correction methods provides any information about the quality of the drift estimation. Therefore, a correction method which operates exclusively on the SMS data, recognizes complex sample movements and is able to deliver a statement about the uncertainty of the drift estimation as well as the corrected image was urgently needed [22, 23]. The second aspect addressed in this thesis is to extend SMS microscopy from a rather qualitative to a quantitative technique, which means counting the number of fluorescent molecules within the structure imaged with high-resolution. Considerable efforts have already been made to solve this counting problem. Unlike in targeted switching applications, the frequency of simultaneously detected photons [24] cannot be used because, correctly executed, the measured photons within a diffraction limited spot stem from a single molecule.Widely used approaches so far are stepwise photobleaching [25] and ratio-comparison to a fluorescence standard [26]. However, the former has an upper limit for the number of countable molecules and the latter relies on trustworthy fluorescence standards. The photophysics of a molecule depend strongly on its immediate environment, so that a fluorescence standard is not a reliable indication within a complex structure. Other methods work directly on the time-

registered events. As the same molecule can be registered several times due to blinking overcounting is a common error source. On the other hand, a molecule may also never light up during the measurement and will therefore never be registered, hence causing an undercounting error. Undercounting can also be caused by events of higher order, which means that more than one molecule are registered within a single event. One approach tries to balance over- and undercounting by means of a photophysical model obtained in a standard sample [27]. However, this requires that the photophysics of the dye does not change between different samples. An approach to overcome this limitation deals with the stochastic nature of photophysical effects by means of a continuous time aggregated Markov model [28]. This method is not only able to determine the number of molecules but also the corresponding kinetic constants. This also holds true for other Markov-based approaches [29, 30]. All these approaches to counting molecules are based on the analysis of switching events. Therefore, they are always prone to errors if individual events are not recognized. This is especially the case when many molecules are present within a diffraction limited region or when switching takes place on time scales that are faster or in the range of the image acquisition rate. Therefore, a counting method for SMS Microscopy that does not rely on fluorescence standards, can be adapted to different photophysical models, takes into account environmental influences on the marker and is able to count low as well as high numbers of molecules was still required.

All tasks to be solved within the scope of this thesis can be excellently approached by means of stochastics. The drift problem can be seen as a random process in which in many independent steps a small number of random molecules is drawn from a population. Although the molecules are randomly chosen, they originate from the density distribution of the overall molecule population. The temporal change of that distribution can be estimated by a statistical analysis. The counting problem can be seen as a sequence of dependent measurements of photon numbers which further depend on the number of underlying molecules. Here an analysis based on a discrete-time Markov chain allows to estimate the molecule number [31]. The main task of this work was to develop experimental methods and to measure relevant data which could be used to verify the mathematical framework on which the data analysis is based. Further tasks, included the identification and correction of experimental error sources as well as adaptions of the underlying photophysical model during the active development of the statistical data analysis.

Chapter 2

From standard to high resolution microscopy

2.1 Standard microscopy and resolution

The optical system of a common light microscope consists of an objective lens and an eyepiece[1, p. 351]. The objective lens gathers the light from an object in its focal plane and produces a magnified image. This image is then observed through the eyepiece and further magnified is thereby such that the total magnification of the microscope M is given by

$$M = M_{obj} M_e.$$

Often the objective lens is coupled with a tube lens. In that case we denote the combined magnification of both lenses as M_{obj}. If the image is observed by a camera the optical system within an eye has to be replaced with a system placed in front of the camera. In this way an image is projected onto the camera sensor. The total magnification has again two contributors, the magnification of the objective lens and that of the subsequent lens system which projects the image onto the camera sensor:

$$M = M_{obj} M_r. \tag{2.1}$$

Furthermore, the total magnification defines the physical area imaged by a camera pixel.

The resolution of a microscope is limited by diffraction at its optical components and apertures. Therefore, it is well explained by diffraction theory [2, p. 418-419,396]: The following explanation refers to fig. 2.1.1. Consider the case the microscope exhibits just one lens and would sharply image two point like objects P and Q into the image plane O$'$. In the focal plane O of the objective lens the objects have a distance of Y and the emitted light intersects the circular aperture of radius a' in the back focal plane F$'$. We want to find an expression for the minimal distance $|Y|$ such that the objects in the image plane are still distinguishable from each other. Since in the paraxial approximation the angle θ'

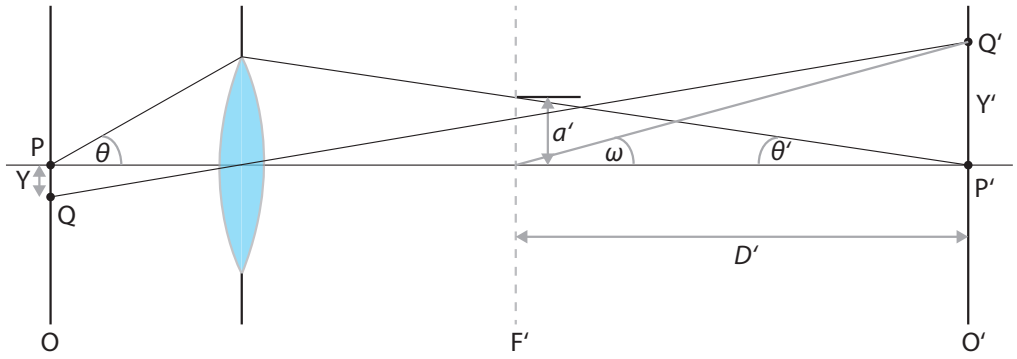

Figure 2.1.1: Abbe diffraction limit of a lens. Two point like objects P,Q are sharply imaged into the image plane O' at which the propagating waves are diffracted at a circular aperture of radius $a^{'}$. From its known diffraction pattern $y(x^{'})$ in conjunction with the Rayleigh criterion follows the Abbe resolution limit.

is small it is given by

$$\theta^{'} = \frac{a'}{D'}.$$

In the paraxial approximation the distance Y' between both objects is small, too. Therefore,

$$Y^{'} = \sin(\omega)D^{'} = \omega D^{'}.$$

The diffraction pattern of a point like object diffracted at a circular aperture is given by the function y

$$y(x) = \Big(\frac{2J_1(x)}{x}\Big)^2$$

where J_1 is the Bessel function of the first kind and first order. The first minimum of y defines the radius of the Airy disk and is usually defined as the width of the paraxial point-spread function (PSF) [32, p. 90]. Let λ and $\lambda^{'}$ be the wavelength of the emitted light in the object and in the image spaces, n and $n^{'}$ the corresponding refractive indexes and λ_0 the vacuum wavelength. The first minimum of y for the image of P is then found under the angle $\omega = 0.61\lambda^{'}/a^{'}$. Thus, the distance $Y^{'}$ is given through

$$Y^{'} = 0.61\frac{\lambda^{'}D^{'}}{a'} = 0.61\frac{\lambda^{'}}{\theta'} = 0.61\frac{\lambda_0}{n'\theta'}.$$

Because the objects are imaged sharply into the image plane they must fulfill the following sine condition

$$nY\sin\theta = -n^{'}Y^{'}\sin\theta^{'}.$$

Due to the paraxial approximation the angles are small such that $\theta = \theta^{'}$. With that condition the Abbe diffraction limit (1873) follows as

$$|Y| \approx 0.61\frac{\lambda_0}{n\sin\theta}.$$

The Abbe limit states the smallest resolved distance between two point like objects such that the first diffraction minimum of one point intersects the maximum of the other in the image plane (Rayleigh criterion). Since this approach does not account for the nature of the imaged objects and the circumstances of the image acquisition it may change. For instance, the result is still valid in the case of two parallel dipoles oriented perpendicular to the optical axis as P and Q. However, it changes if the dipoles are oriented parallel to the optical axis [33, 34][32, p. 86]. If the objects do not emit light themselves but are illuminated with coherent light the theoretical limit changes again [2, p. 419]. Moreover, diffraction is not limited to a confining aperture as in the given example, e.g. reflection at a mirror of radius $a^{'}$ produces the same PSF [35, p. 319].

Finally, the theoretical resolution limit in direction of the optical axis is given through [32, p. 98]

$$|Z| \approx 2\frac{\lambda_0}{n\sin^2\theta}$$

and is larger than the lateral resolution $|Y|$ for standard microscopy.

2.2 Circumvent diffraction - the principle of bright and dark

Diffraction is an inherent characteristic of waves and therefore always occurs. But Abbe's resolution limit does not account for all possible circumstances during image acquisition. Thus, it is not a fundamental limit of resolution as believed for long time. The fundamental principle behind super resolution microscopy is to exploit the molecular properties of fluorescent markers which can be switched between a dark and a bright state. Reversible switching is not mandatory. In the bright state dye molecules are detected while molecules in the dark state are not. If this principle is applied correctly, the position of molecules in the bright state can be determined in the nm regime. Meanwhile there exist various methods in super resolution microscopy which exploit this principle in their own way, e.g. STED [6, 7], GSD [8], GSDIM [17], RESOLFT [9, 10, 11, 12], PALM [18], PALMIRA [19].

Fluorophores have proven to be an excellent choice for super resolved microscopy. They can be labeled specifically to the target of interest and they deliver a high signal-to-noise ratio in the imaging process [36, p. 10]. Therefore, we discuss the effect of fluorescence in detail which is clearly presented in a Jablonski diagram [32, p. 283] depicted in fig. 2.2.1. The lowest electronic energy transition appears between the highest occupied molecular orbital (HOMO) and the lowest unoccupied molecular orbital (LUMO). Due to vibrational motions of the heavy nuclei the electronic states exhibit a manifold of vibrational states because the low mass electrons are considered to follow the motion immediately. Furthermore, at room temperature thermal energy is insufficient to excite a higher vibrational state. Therefore, electrons start in the HOMO. We consider a two electron system because it is the simplest case of a multiple electron system. Their two spins $\mathbf{s}$=1/2 may arrange antiparallel such that the total spin S = 0 and $m = 0$ or parallel resulting in S = 1 and $m = \{1, 0, -1\}$. The first case is denoted as singlet states S_n while the latter

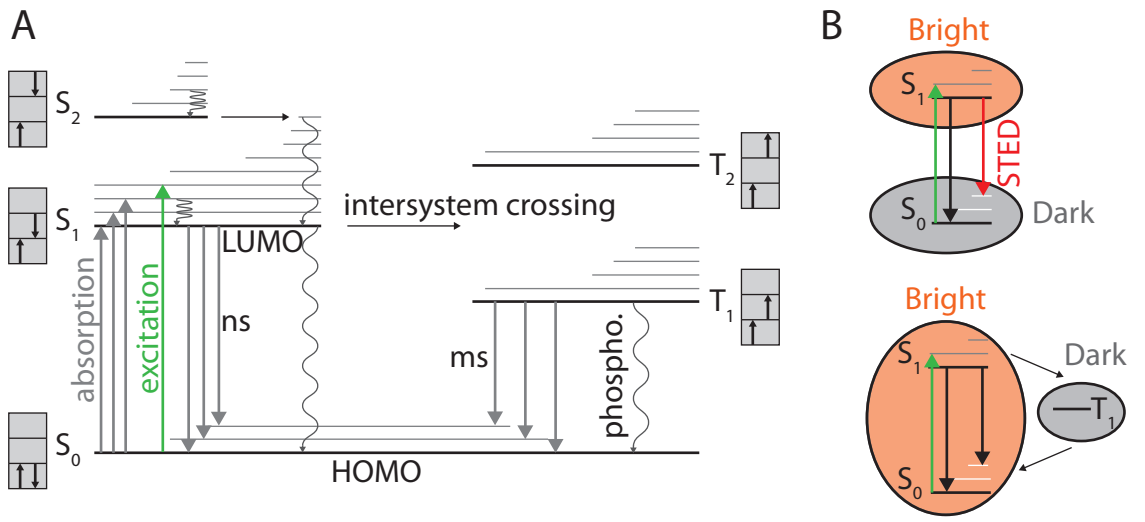

Figure 2.2.1: A: Jablonski diagram. Depicted are the energy levels within a typical fluorophore. The highest unoccupied molecular orbital (HOMO) is the ground state of the two electron system. Because the nuclei of the fluorophore can vibrate each orbital posses a manifold of vibrational states. An electron is excited from the ground state in higher orbitals which can be the lowest unoccupied molecular orbital (LUMO), higher orbitals and the vibrational states of these orbitals. From vibrational states an electron relaxes fast to the lowest energy level of the orbital (Kasha rule). Fluorescence occurs between transitions from LUMO to vibration states of HOMO. Therefore, it is observed as a red shifted frequency band relative to the excitation frequency (Stokes shift). With low probability an electron flips a spin due to spin orbit coupling (intersystem crossing). Thereby, the electron enters a triplet state which has a long lifetime (ms) compared to LUMO (ns) because the transition in the ground state (phosphorescense) is forbidden. B: The bright and dark state principle of high resolution microscopy in conjunction with the energy states from the Jablonski diagram for STED (top) and GSDIM and GSD (bottom).

one is denoted as triplet states T_n due to its multiplicity of three. Excitation can be resonant from S_0 to S_1 but usually excites a vibrational state of S_1 which is followed by a fast vibrational relaxation (Kasha rule). Thereby, energy dissipates as heat. For efficient fluorophores this decay ends in the vibrational ground state of S_1. From there fluorescence photons are emitted by a transition to one of the various vibrational states of S_0. These photons are red shifted relative to the excitation which is called Stokes shift. An electron may also execute a spin flip known as intersystem crossing. This is allowed because not the total spin S but **J**=**L**+**S** must be conserved where **L** is the angular momentum of the electron orbital. However, the probability for such an event is small compared to the probability for fluorescence. Because a transition from a triplet state into the ground state is forbidden the triplet states exhibit a much longer lifetime (µs-ms) than the excited singlet states (ns) at which the lifetimes strongly depend on the environment [8, 37]. Free oxygen quenches the lifetime of triplet states for many dyes [38]. That led to the common use of an oxygen scavenging system (GLOX) for applications in need of long living dark states [39]. One important transition is not stated in the diagram. After excitation fluorophores may irreversibly cease to fluoresce with a certain probability also called photobleaching. The process is not well understood because it depends on the environment and the structure of the fluorophore itself. One source for photobleaching is molecular

oxygen [40, p. 690-702][41]. A fluorophore in its triplet state has a long time span (ms) to react with molecular oxygen which results in the generation of damaging oxygen radicals. This further increases the importance of an oxygen scavenging system. Another source of bleaching is a high excitation power such that the fluorophores reach higher excited states $S_{n>1}$ from which an increased bleaching rate, for example, for rhodamines was observed [42].

Which states are used as bright and dark states depends on the specific highresolution method. Two examples are depicted in fig. 2.2.1 for STED and GSDIM. Note, that more states than depicted can be involved in the real photophysical process. In STED applications the triplet state's lifetime may be quenched by medium buffer ingredients to increase the stability of the fluorescence signal [37]. For GSDIM on the other hand prolonged dark times are desired which means that a long lifetime of the triplet state or other intentionally generated dark states is favorable. For instance, for many dyes a thiolated dark state with a long lifetime is induced by the buffer ingredient β-mercaptoethanol (βME) [38, 39, 43]. Furthermore, both applications serve as examples for a general classification into targeted switching and stochastic switching methods.

2.3 Targeted switching

The targeted switching applications use well designed spatial light distributions such that fluorescent markers at predefined target areas in the specimen have a high probability to populate the bright state meanwhile their immediate vicinity has a high probability to populate a dark state. Super resolution is then achieved by confining the targeted areas to widths d which are much smaller than the Abbe resolution limit

$$d \ll 0.61 \frac{\lambda_0}{n \sin\theta}.$$

A well known application of this kind is STED, a synonym for stimulated emission depletion. It uses an excitation beam to excite molecules to the higher orbital S_1 from which they will subsequently fluoresce (fig. 2.2.1B.top). The width of that beam alone is at best diffraction limited and not sufficient to achieve high resolution. Therefore, it is overlain by a doughnut shaped beam whose central intensity is ideally zero. Furthermore, the frequency of the doughnut beam is far red shifted relative to the excitation such that it depopulates the excited state S_1 by stimulated emission, a transition to a vibrational level of the ground state S_0. In that way molecules in the bright state are depleted at locations illuminated by the STED beam, except at its zero intensity center. The far red shift of its wavelength allows for using a dichroic mirror to separate the stimulated photons from the detection band within the fluorescence spectrum. The width of the remaining bright spot was found to follow [5, 44]

$$d \geq \frac{\lambda}{2n \sin\theta \sqrt{1 + a \frac{I_{\max}}{I_{\text{sat}}}}}$$

where $a > 0$ depends on the shape of the STED beam, $I_{\max}$ is its maximum intensity and I_{sat} is a value which scales inverse proportional with the life time τ of the excited state S_1. The equation is an expansion of the Abbe formula. Theoretically an arbitrarily high resolution can be achieved for infinitly high STED intensities but experiments are hindered by the maximum power of a laser system, possible photodamage of the specimen [45] and the photo-stability of the fluorophore. All these problems can be minimized by choosing dyes with a long natural lifetime τ which implicates a small I_{sat}. Even when these problems are avoided the equation is inappropriate when the resolution reaches the size of the fluorophore. A very similar concept which exploits low saturation intensities through long living dark states is called GSD, Ground State Depletion [8, 46]. Here the doughnut beam and excitation beam have the same wavelength. The doughnut shaped beam excites fluorophores by a $S_0 - S_1$ transition. They can subsequently fluoresce or populate the triplet state by inter system crossing (fig. 2.2.1A). Due to its comparably long lifetime fluorophores can be seen as trapped in this dark state (fig. 2.2.1B.bottom). Once all fluorophores are trapped a second diffraction limited beam of the same frequency reads out the remaining bright fluorophores in the center of the doughnut beam. While STED needs laser intensities of 100 MW/cm^2, several kw/cm^2 are already sufficient for GSD due to the long lifetime of the dark state.

Tomographic STED Microscopy nearly halved the necessary depletion power by introducing a one dimensional depletion pattern which is rotated several times during image acquisition Thereby, locally higher intensities in the pattern are achieved. [47]. The advantage of lower STED power is payed for with a subsequent analysis of the data.

If GSD and STED are expanded to reversibly activatable proteins and organic fluorophores it is called RESOLFT [9, 10, 12], reversible saturable optical fluorescence transitions, which exploits conformational changes of the dye molecule to switch between dark and bright state.

Saturated patterned excitation microscopy (SPEM) [14] and saturated structured illumination microscopy (SSIM)[13] use a standing wave interference pattern to saturate the bright state. Its fluorescence is imaged by a camera and subsequently analyzed in the Fourier domain. The analysis in conjunction with the a priori knowledge of the pattern frequency reveals structures below the Abbe resolution limit. To achieve a super resolved image in 2D the pattern has to be rotated and scanned over the specimen because the resolution improvement is perpendicular to the minima pattern.

2.4 Stochastic Switching

Instead of switching molecules at predefined positions within the sample switching can also be performed stochastically under two conditions: First only one dye molecule within the width of its PSF occupies the bright state at any time. While the single molecule occupies the bright state it emits a high number $N \gg 1$ photons which are detected with an area detector. The first condition is based on the fact that single molecules can be

localized by estimating the center of their diffraction limited patterns on the detector. This can be done reliably by fitting a Gaussian distribution to the PSF. If the photon distribution stems from more than one molecule a single Gaussian fit will result in a wrong localization. This condition also implicates that the high resolution is achieved by time sequential localization of many molecules since the majority must populate the dark state during image acquisition. The second condition is needed because the estimation precision Δr of the center was found to be proportional to $1/\sqrt{\mathrm{N}}$ [48, 49]

$$\Delta r \approx \frac{\lambda}{2n \sin\theta \sqrt{N}}. \tag{2.2}$$

Three similar concepts were realized nearly simultaneously. Photoactivated localization microscopy (PALM) [18] exploits photoactivable fluorescent proteins as well as fluorescence photoactivation localization microscopy (FPALM) [20]. The other concept is called stochastical reconstruction microscopy (STORM) [15] and uses two photochromic dyes at which one dye is a facilitator. The acquisition time in both concepts took up to 10 hours which required very stable microscopes. This problem was highly reduced by photo activated localization microscopy with independent running acquisition (PALMIRA) [19]. Here, the switching is performed asynchronous to image acquisition which reduced the measurement time to several minutes.

The stochastic concept of GSD is called ground state depletion followed by individual molecule return (GSDIM) [17]. Here, unlike the other stochastic methods so far all molecules start in the bright state and are first pumped into a dark state before the localization process (fig. 2.2.1B.bottom). The initially visible fluorescence is an advantage because it allows to preselect structures within the specimen. Also no further switching laser for activation is needed.

The generalization of STORM is called direct STORM (dSTORM) [16] and is no longer restricted to a facilitator dye for activation. Points accumulation for imaging in nanoscale topography (PAINT) [50] uses sequentially activated dye molecules which are activated by binding to a structure.

All these concepts switch single molecules to the bright state. Therefore, they are subsumed under the term single marker switching (SMS) as from now on.

2.5 SMS microscopy

Because this work focuses on SMS applications, we discuss the process of data acquisition, localization procedure and image representation in detail.

2.5.1 Data acquisition

We consider a specimen at which the target of interest, e.g. α-tubulin, is labeled with switchable fluorophores which have at least a dark and a bright state (fig. 2.2.1B.bottom). Furthermore, we consider a GSDIM application at which fluorescence is imaged by a EMCCD camera. The specimen is illuminated in wide field mode which means that the

light field can be (ideally) assumed as plane waves within the specimen. Note, distortions from this assumption are in general not crucial because SMS microscopy does not depend on spatially designed light fields. Since fluorophores start in the bright state they have to be pumped into the dark state meanwhile the raw structure of the specimen is revealed by the initial fluorescence. Pumping continues until nearly all dye molecules populate the dark state and the detected diffraction limited patterns of single bright molecules do not overlap. The specimen has become 'sparse' as depicted in fig. 2.5.1.

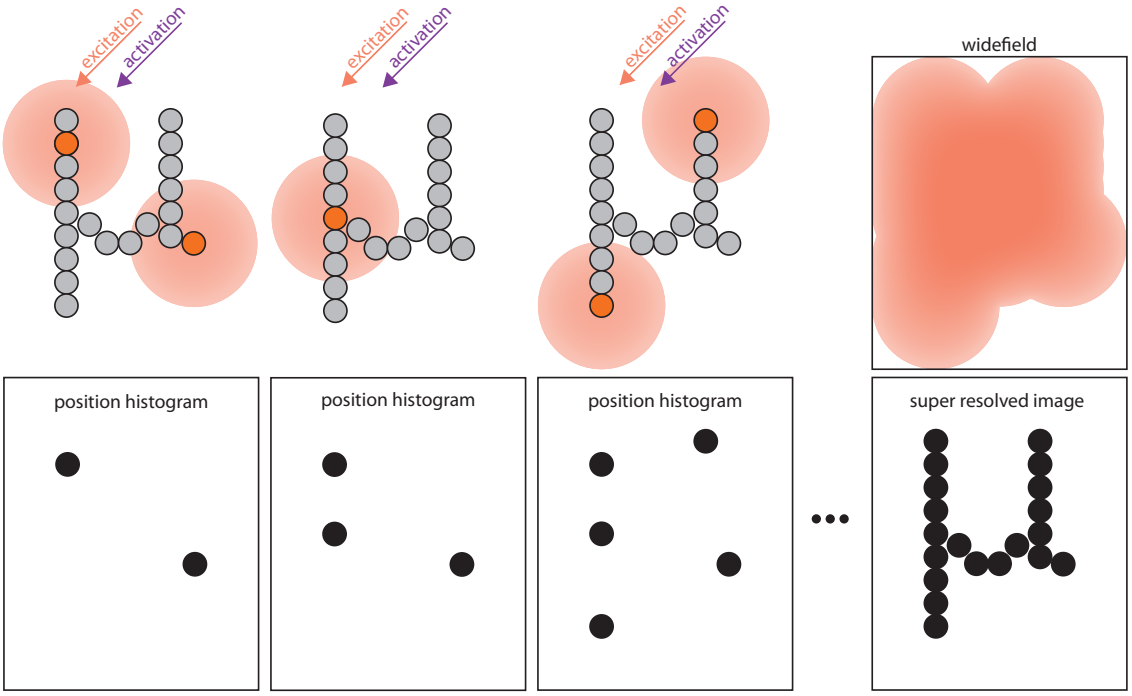

Figure 2.5.1: SMS microscopy. A specimen labeled with switchable markers, e.g. fluorophores, is imaged with an EMCCD camera. Markers populate either a dark state (grey) or the bright state (orange) in which they are detected. The density of bright markers is either determined by spontaneous transitions or can be controlled by UV light in many applications (activation). Emitted photons of a single marker are distributed within diffraction limited patterns, the PSF, sketched as diffuse orange areas. In each recorded frame the center of the PSF is localized and drawn into a position histogram. Correctly executed the patterns never overlap on the camera because it would result in wrong localizations. If done for a sufficient number of frames the position histogram resembles a super resolved image of the imaged structure. The temporal unmixing of the maker signals becomes visible if all detected patterns are added up which resembles a view through a standard wide field microscope.

From this point on the density of bright fluorophores is either determined by spontaneous transitions from the dark state to the bright state or can be controlled via irradiation with UV light, e.g. 371 nm or 405 nm. On the one hand it is important to avoid high densities because overlapping fluorescence patterns are a source of error in the subsequent localization procedure. On the other hand a very low density increases the acquisition time and hence a possible error due to drift. This error will be discussed in detail later. The sparse specimen is imaged for several minutes which results in thousands of frames. In each frame the centers of the recorded PSFs are localized and drawn in a position histogram. If executed for a sufficient amount of frames the position histogram will re-

semble a super resolved image of the imaged structure. This temporal unmixing of the fluorescence signals of thousands of fluorophores becomes visible if all recorded patterns are added up. The added up image resembles the view through a standard wide field microscope (fig. 2.5.1). As mentioned before the localization precision is proportional to $1/\sqrt{N}$ where N is the number of detected photons within a diffraction pattern on the camera. Therefore, it is advantageous to gather all detected photons stemming from one uninterrupted occupation of the bright state within one frame and not distribute them over several frames. The uninterrupted stream of photons from a single molecule is called 'burst'. The detected diffraction pattern on the camera sensor during one frame is called an event. Unfortunately, not all bursts can be imaged within one frame because the number of emitted photons during one burst is a random variable Y. Its distribution is given by a geometrical distribution

$$\mathrm{Geom}(Y = N|q) = (1-q)^N q \tag{2.3}$$

where q denotes the probability for a transition into the dark state and $p = 1 - q$ the probability to stay in the bright state. To emit N photons the fluorophore must stay N times in the bright state and finish this process with a transition to the dark state. Simply increasing the recording time of a frame, also known as exposure time, is not recommended because it will first reduce the signal-to-noise ratio and second increase the chance to record overlapping diffraction patterns (double events). Therefore, the best exposure time is a trade off. Besides the number of detected photons the size of the camera pixels affect the resolution which is adjusted by the total magnification M_{tot} of the microscope (eq. 2.1). A good choice as pixel size is the standard deviation of the PSF. A bigger size causes a loss of information and a smaller one decreases the signal-to-noise ratio. Detailed information can be found in [51]. Furthermore, the acquisition theme in this work follows PALMIRA [19] which proposed an independently running acquisition. It means, that activation is not synchronized with the camera frames and fluorophores are activated stochastically in time.

2.5.2 Localization procedure and its precision

In order to obtain a high resolution image from the recorded diffraction patterns the position of the molecules have to be determined. The localization procedure often uses a two dimensional Gaussian distribution which is fitted to each registered event

$$\mathrm{PSF} = A \exp \frac{(x - x_c^2) + (y - y_c)^2}{2\sigma^2} \tag{2.4}$$

where σ is its standard deviation and x_c, y_c the position of the marker. In this work the events are registered in two steps. First the inhomogeneous background is removed by smoothing a raw frame I_{raw} with a two dimensional Gaussian. This resembles a low pass filter, all visible structures are removed in the smoothed frame I_{sm}. Then it is subtracted from the raw frame to receive the filtered frame I_{fil}. Second in the filtered frame all events are found by listing values bigger than a defined threshold T and the corresponding

evaluation boxes containing this values are defined. In these boxes eq. 2.4 is fitted to the detected photons to estimate the marker position. A more detailed description of the localization routine can be found in [36, p. 25-27].

The localization precision of a SMS microscope is given by eq. 2.2

$$\Delta r \approx \frac{\lambda}{2n \sin\theta \sqrt{N}} \tag{2.5}$$

where N denotes the number of detected photons in the event. The photon dependence becomes reasonable if you see each photon as an independent measurement of the PSF. Hence its localization becomes more accurate with more detected photons. A more rigorous analysis of the localization precision takes the thresholding act of the localization procedure into account which cuts of the expected geometric photon distribution presented in eq. 2.3. Then the localization precision is given by [52]

$$\Delta r \geq \frac{\lambda}{2n \sin\theta} \sqrt{\frac{\Phi(\frac{N}{N+1}, 1, T)}{N+1}}.$$

Here, Φ is Lerch's-Φ-transcendent which describes the stochastic spread, hence the photon values above the threshold T. For most applications, including this work, this rigorous equation is not necessary. Instead of using the FWHM the localization precision can also be defined by the standard deviation

$$\sigma = \frac{\Delta r}{2\sqrt{2 \ln 2}}$$

differing by a constant factor. The considerations so far neglect other noise sources than shot noise, eg. dark counts, readout noise, pixelation noise and background noise which can be reviewed in [51]. The multiplication register of an EMCCD camera introduces additional noise, mathematically described by the excess noise factor $f = \sqrt{2}$ [53]. It is explained in detail in section 4.3.7. This noise has an impact on the localization accuracy given through

$$\Delta r_{EMCCD} = f \cdot \Delta r = \frac{\lambda}{2n \sin\theta \sqrt{N/2}}. \tag{2.6}$$

Although it introduces additional noise an EMCCD camera practically removes the read-out noise for large total gain factors. It runs at low chip temperature, therefore it also has very low dark count errors caused by dark current. Furthermore, it has a high duty cycle, which means it images frames very fast resulting in reduced measurement times. This qualities outweigh the disadvantage of excess noise and make it well suited for SMS microscopy. Because we image with an EMCCD camera the localization precision for this work is given through eq. 2.6. Background noise can be removed by optical filters or additional evaluation routines like the smoothing step during the localization procedure.

2.5.3 Image representation

The localized events in each frame form a long list but not an image. Besides the coordinates (x_c, y_c) the list also contains the information on the number of detected photons N

for each event. There are several methods to present the information in the list, each has its advantages and disadvantages. The histogram view creates a xy-pixel-grid at which the pixel size equals roughly half the expected average resolution according to eq. 2.6 and the size of the grid equals the size of the imaged frame. Each pixel receives a value equal to the number of events located within its borders. If a marker is localized many times its effective PSF will be nicely resolved in the histogram. However, the information of the detected photon numbers is lost in this presentation. The 'Gaussian' view plots a Gaussian function at the listed location. Each Gaussian has a standard deviation σ depending on the number of detected photons N according to eq. 2.5. This results in a broader effective PSF than in the histogram view [52]. Furthermore, it feigns a larger dynamic range to the eye. The brightness view is similar to the histogram view but the pixel values equal to the sum of all photons corresponding to localized events within the borders of a pixel. This presentation loses the information on the number of registered events. Because each of this views does not depict all available information it is appropriate to choose a view according to the specific experiment. A deeper description of the different representations is given in [54].

Besides the representation there are other ways to influence the final image. Note, although the high resolution image is adaptable it does not mean the result is arbitrary. One opportunity is the photon threshold T. Higher threshold values discard dimer events which have a larger localization precision due to a larger number of photons within an event. This may increase the overall resolution within an superresolved image but it discards a lot of events which can result in a 'spotty' image. In such a spotty image structures may not be recognizable anymore, thereby contradicting the gain in localization precision. Within certain limits SMS images can be adapted to the needs of the experiment because the threshold value can also account for systematic effects, e.g. a change of the average emitted photons due to the marker's environment. Furthermore, an upper threshold prevents the registering of events of higher order (double events etc.) because such events typically come with higher photon numbers. Besides photon thresholding shape and time dependent analysis of the recorded shape are opportunities to influence the super resolved image. If an event of higher order is recorded its photon distribution on the camera sensor may differ strongly from the expected PSF, thereby delivering a criterion to discard it. The time analysis can be used in two ways. If events are recorded at the same location for many subsequent frames, e.g. twice the average time of a single molecule burst, it is likely they stem from more than one molecule and can be discarded. Thus, a time threshold τ can be introduced. The other way is to concatenate events belonging to one burst into a single event, thereby increasing the localization accuracy. On the one hand time thresholding is easily executed but to choose a scientific justified threshold is not straightforward and highly depends on the marker [27]. On the other hand the concatenate procedure may result in a spotty image like photon thresholding.

Chapter 3

Stochastic data based correction method for rigid motion in SMS microscopy

SMS microscopy trades speed for spatial resolution due to the temporal spatial unmixing of the fluorescence signal as shown in fig. 2.5.1. Thereby, typical measurement times are several minutes in which the mechanical stability of the microscope becomes a limiting factor for the quality of the super resolved image [21]. Instabilities may significantly decrease the resolution of the final image. Especially relative movements between objective lens and specimen have a strong influence on the super resolved image because the corresponding movement in the camera plane depends on the total magnification of the microscope M_{tot}. In constrast, a comparable movement of an optical part after the objective lens only experiences the typically much smaller magnification of the remaining optical system and has therefore less impact on the image. However, even if the microscope and the specimen show no relative motion at all SMS microscopy may still be challenged by living specimens because cell movement also blurs the super resolved image.

In the following, the term drift is used for any unwanted movement of the imaged structure during data acquisition. Several methods for drift estimation and correction have been established. A widely used method is fiducial marker tracking. The idea is that the movement of single bright and photo-stable emitters in the sample represents the actual movement of the structure. For this, typically bright fluorescent beads are randomly incorporated into the sample, e. g. by incubating the sample with a diluted bead solution. The localized position of one or more fiducial markers in each frame will then be used to derive the actual estimated sample movement, which is - in the simplest case - a global translational movement. Though the concept of fiducial marker tracking is very simple, there are several practical challenges. First, they are randomly distributed in the specimen. Therefore, often too few or too many markers are found next to an interesting structure. Second, the fiducials often outshine the fluorophore signal in their neighborhood causing voids within the superresolved image. Third, they have to be chosen

carefully according to the experimental conditions. In the beginning of a measurement they must not saturate the camera sensor which would prevent their localization. Also they must not bleach too fast since all frames without visible fiducials cannot be corrected. Fourth, they may show own drift relative to the specimen. Therefore, it is advantageous to use more than one fiducial for correction. Overall their application is laborious and a drift correction method based purely on the recorded stochastic SMS data itself is preferable.

Such a published correction approach bins the localized events not in one position histogram, but in several sparse subimages. All subimages are then correlated with all other to estimate the drift. This method has proven its reliability by producing similar results as fiducial marker tracking [21]. But it does not deliver a quality seal for the estimated super resolved image and the drift estimation.

Here we present a method, composed of a semi parametric model and a drift estimator for rigid drift taken from [23] which is based on [22]. The estimater was expanded from soley translational drift estimation to additional rotation and scaling correction. Rigid means, that in the image plane at the camera sensor the frame is shifted as a whole and not just a part or several different parts of it. The estimator is used to correct the final image and it is shown that this purely statistical method is competitive with fiducial marker tracking. Moreover, a simple bootstrap algorithm allows to quantify the precision on the motion estimate and its effect on the final image estimation. The practicability of our method is demonstrated by SMS application. The scope of this work is to generate reliable experimental SMS data which is blurred by controlled translational and rotational motion and to estimate the 'true' image by means of fiducial marker tracking. Thus, the result of our drift estimator method are verifiable. Such movements could also have been subsequently added to drift free SMS data. However, this approach would not have differed fundamentally from a pure simulation, since drift would not have been part of the experiment. We have therefore decided against it in order to test our method as close to its application as possible.

3.1 Setup - Generating controlled motion in a SMS application

The setup exhibits a wide range of excitation lasers at wavelengths of 639 nm, 560 nm, 532 nm and 488 nm in order to be applicable to many different fluorophores (fig. 3.1.1). The laser beams are superimposed by means of dichroic mirrors and their widths are adjusted by several telescopes to match the entrance aperture (1.5 mm) of an acousto-optical tunable filter (AOTF). The tunable filter allows to control the laser power transferred to the remaining optical system. Furthermore, we use it to switch on the laser reliably within a time window several 10 µs. This window is caused by a jitter between the signaling PC and the receiving radio frequency driver of the AOTF. The beams are then imaged by two telescopes such that they are centered in the field of view (FOV) of the objective lens and their radius is ca. 38 µm. The FOV in the sample is typically chosen such that it confines

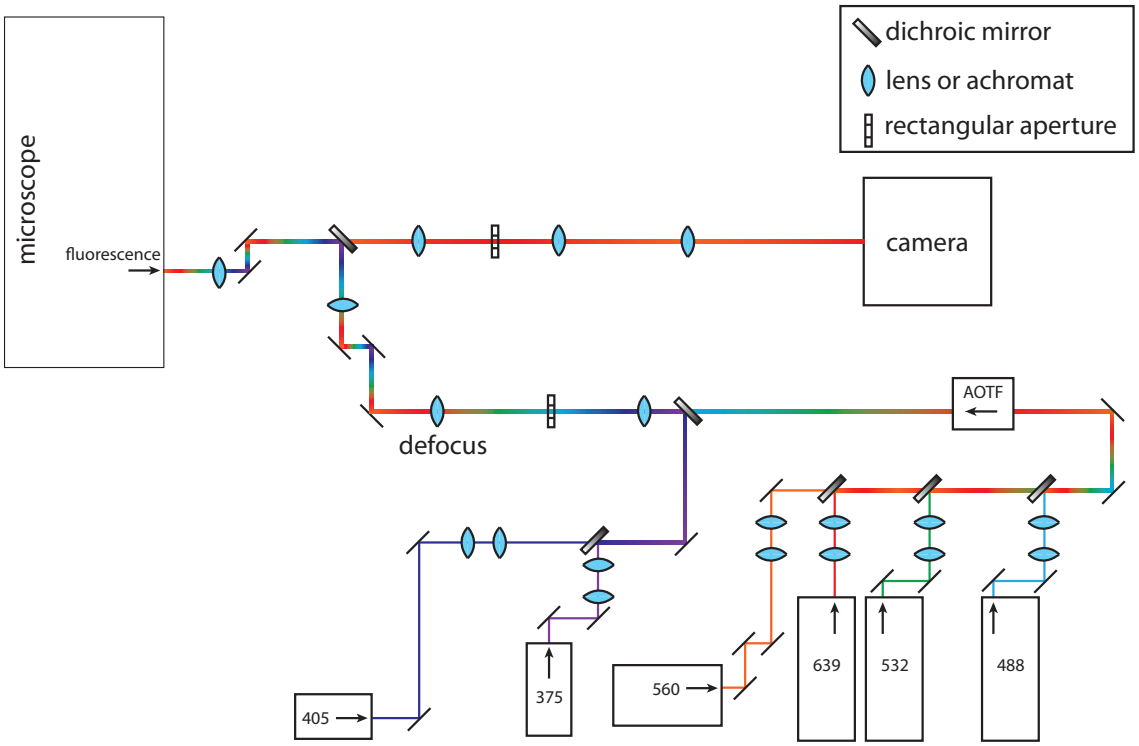

Figure 3.1.1: SMS setup. A wide range of excitation wavelengths allow to image many dyes (639 nm, 560 nm, 532 nm, 488 nm). UV-Laser (405 nm, 371 nm) transfer dyes from the dark state in the bright state (activation). All beams are overlain by dichroic mirrors and adjusted to the same beam width by telescopes. An acousto-optical tunable filter (AOTF) switches excitation beams reliably on and off in several 10 µs. The illumination beam is not focused in the back focal plane of the objective lense but ca. 10 mm below it (defocus). A modified highly stable microscope hosts a tube lens, the objective lens and several stages to move the specimen holder. The optical detection system exhibits an EMCCD camera and two telescopes in a $4f$ arrangement which magnify the image. Furthermore, a rectangular aperture in an intermediate image plane allows to modify the detected image on the EMCCD camera. An other aperture in an intermediate image plane of the illumination system confines excitation and UV power within a selectable field of view of the objective lens.

only the inner part of the Gaussian laser beam. Thus, the excitation intensity in the FOV is sufficiently homogeneous. Still fluorophores in the inner part of the FOV emit in average more photons than at the edges due to the Gaussian beam shape. This behavior has to be considered for quantitative measurements, see section 4.3.6. Ideally you would adjust illumination such that a collimated beam leaves the objective lens and the wavefield in the focal plane can be approximated as planar waves. This adjustment leads to an easy understanding of the wavefield inside the specimen and avoids stray light. This is achieved by focusing the beam in the back focal plane of the objective lens. Unfortunately, the back focal plane of the used Olympus 100x oil objective lies inside the objective lens. Thus, a beam focus at the back focal plane can damage the objective due to the high energy density. Therefore, we introduced a defocus which focuses the excitation beam ca. 10 mm before the entrance pupil. Hence, our excitation beam is not collimated inside the specimen but still provides sufficient intensities in the FOV. Furthermore, before the defocus is applied the beams are overlain with two UV laser beams of 405 nm and 371 nm wavelength

which have been adjusted to the same beam radius. Shutters allow to control the UV light independent from the excitation light. Fluorescence is separated from excitation light by a dichroic mirror and detected by an Andor iXon X_3 EMCCD-camera. It exhibits a fast imaging speed and a low noise, since its read out noise is rendered negligible by electron multiplication, see section 4.3.7. If the full sensor of 512×512 pixel is read out the exposure time of the camera is at least 33 ms. However, often using the full sensor for imaging is not necessary and a faster imaging speed desirable. Most measurements of this work have an exposure time of 15 or 20 ms and use a fraction of the sensor for imaging which allows the faster imaging speed due to reduced readout time. In this mode it is necessary to shield the unused part of the sensor because it is still generating photoelectrons which are not completely transferred to the readout register before the beginning of the next frame. Thereby, this signal adds to the background noise. The shielding is executed by an adjustable rectangular aperture placed in an intermediate image plane of the optical detection system. Another rectangular safe guard slit located at an intermediate image plane of the optical illumination system shields the unimaged parts of the specimen from excitation and UV-light. This is important in our quantitative counting measurements, see section 4.3.1. The detection system exhibits the objective lens, tube lens and two additional telescopes. These telescopes allow to adjust the effective pixel size of the camera to the desired value (section 2.1), in our case 130 nm, and to place optical surfaces like dichroic mirrors far away from intermediate image planes.

Objective lens and tube lens are incorporated in the modified body of a Leica DM IRE2 microscope (fig. 3.1.2.A). The body offers the advantage to observe a specimen through the integrated eyepiece. Its modification had two intentions. First the goal was to apply controlled translational and rotational sample movement to verify the results of the drift estimator. Second we modified the microscope for high stability such that the controlled movement is not disturbed. Two orthogonally placed piezo elements (SmarAct SLC-1720) apply x- and y-movement to the specimen holder with an accuracy of 1 nm and a rotation stage (Newport RVS80CC) applies rotational movement with a step accuracy of 10 mdeg. High accuracy is necessary because it would result in a non smooth motion otherwise.

As mentioned before overall stability is crucially determined by relative drift between objective lens and specimen. The original design exhibited considerable drift during a typical measurement time (fig. 3.1.3.A). We achieved high stability (fig. 3.1.3.B) by connecting the objective lens holder (fig. 3.1.2.B) and all equipment needed for the controlled movement (fig. 3.1.2.A) to the same base plate which was not the case in the original design of the body. Thereby, drift of the base plate does now not result in a relative movement between objective lens and specimen. For the same reason a drift stemming from the microscope body is negligible.

Furthermore, we carefully designed the system to place the center of rotation within the FOV of several 10 µm since an observed rotational drift caused by a far placed rotation axis would appear as a translational movement and thereby contradict its purpose.

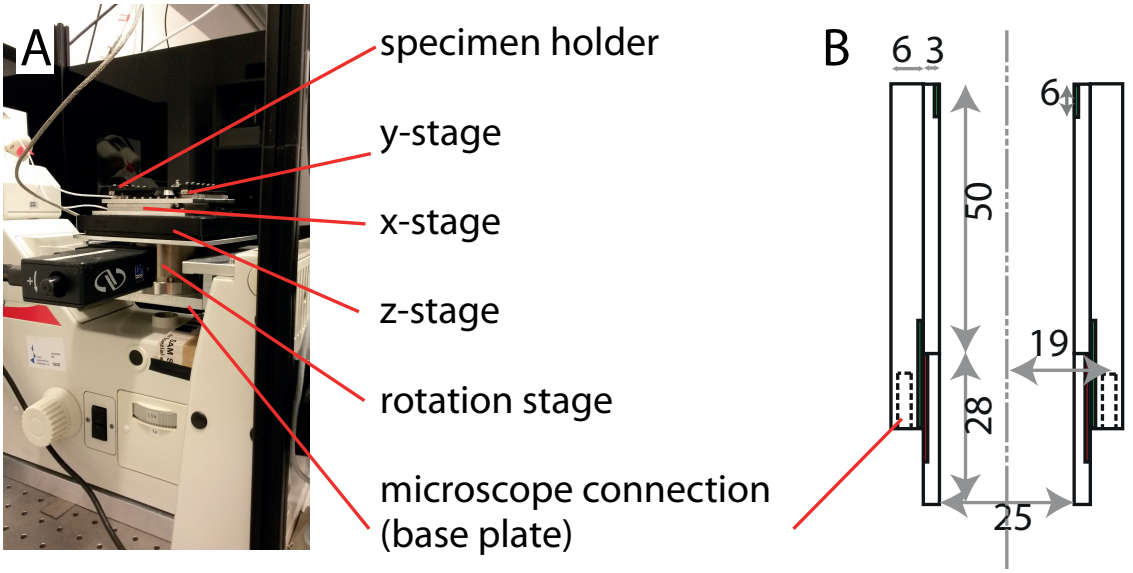

Figure 3.1.2: A: Modified microscope body. Depicted is the base plate, rotation stage, z-stage, x-stage (piezo element), y-stage (piezo element) and specimen holder from bottom to top, respectively. The rotation stage applies controlled movement with an accuracy of 10 mdeg, x- and y-stage apply translational movement with an accuracy of 1 nm. The z-stage adjusts the specimen in the focal plane of the objective lens which is barely visible because it is surrounded by the named equipment. The equipment is fixed to the baseplate. The black plate in the background is part of a protection cage which is closed during a measurement to shield objective lens and specimen from the environment. B: Shown is the objective lens holder which is placed within the rotation stage. The symmetric line depicts the rotation axis. The holder itself is a tube containing one sliding tube (top) and a threaded tube (bottom). The position of the threaded tube can be adjusted at which the sliding tube changes its position accordingly. The resting tube carries the objective lens and can additionally be fixed by a not depicted screw.

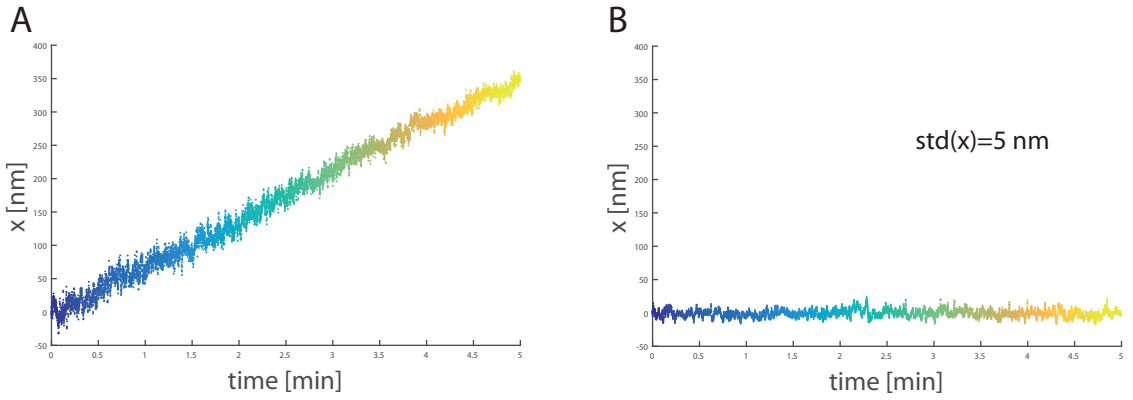

Figure 3.1.3: A: Stability measurement for unmodified microscope by fiducial marker tracking. Two markers which showed no relative movement to each other were imaged for 5 minutes and subsequently localized in each image. Depicted is the x-trajectory of one fiducial. Because the fiducials did not move relative to each other the trajectory depicts the drift of the unmodified microscope. During a typical measurement time for SMS microscopy the unmodified microscope drifted more than 300 nm which is unacceptable in our task to generate controlled movement. B: Stability measurement for modified microscope by fiducial marker tracking. Depicted is the trajectory of a fiducial marker measured in the modified setup. Again we assured it is no movement of the marker itself as in A. The microscope is stable on a scale of 10 nm since the standard deviation of the drift is 5 nm.

3.2 Fiducial marker tracking as reference

Without elaborated drift estimation methods fiducial marker tracking is used as the state of the art correction technique. Therefore, we use it as reference for our purely SMS data based correction method. In the case of solely applied translational motion the execution of fiducial marker tracking with subsequent correction is applicable without any additional considerations [23, p. 10-11][22]. This changes in the case of applied rotational movement because we found the position of the rotation axis to change in time. This problem challenges the fiducial maker correction as well as the data based correction. Because we wanted to know the optimal reconstructed image we conducted an extended reconstruction based on fiducial marker tracking which used the known angular velocity of the rotational movement. Note, this optimal result does not resemble the result achieved by a normal fiducial correction since we use knowledge of the drift which is usually unknown. We will discuss this in detail later.

3.2.1 Extended reconstruction

The data presented her shows stained β-tubulin in HeLa cells. The dye is Flip 565 (Aberior) which is excited with a light of wavelength 560 nm. The medium is a simple PBS buffer and we use 371 nm for activation since Flip 565 starts in a dark state. We imaged a sequence of 30000 frames with an exposure time of 20 ms. The pixel size of the camera is 130 nm. During the measurement time the rotation stage moved 1.4° with an angular velocity of $\gamma = 1.4/180 \cdot \pi/600$ Hz. The localization procedure is executed and thereby a list of localized marker positions generated. Because the density in the beginning of the measurement is too high we remove the first 1000 frames from the sequence and their according localizations. In the following the first frame is 1001 denoted by $t = 1$.

In a first step we must identify the fiducial markers trajectories. Therefore all fiducials (beads) are identified by their brightness in the first frame of the sequence as they are much brighter than events of single Flip 565 markers. A box of size 9x9 pixel is defined at the location of each bead. Inside these boxes all events are identified in all subsequent frames. These events contain the time dependent bead positions and Flip 565 events as noise. When identifying the bead positions in all subsequent frames we account for its bleaching which decreases its brightness gradually in time.

Due to bleaching the brightness of a bead decreases gradually in time. By identifying the bead position within each frame we determine the bead trajectory of bead i as $\mathbf{u}_i(t)$ at which $\mathbf{u}_{i,t}$ is its value at time t.

We define a maximum and minimum threshold for the bead at the beginning and scale them accordingly to the last known brightness of the fiducial. Thereby, we recursively identify the bead trajectory. Should more than one event lie within the brightness thresholds we choose the brightest. We denote the two dimensional time dependent trajectory of bead i as $\mathbf{u}_i(t)$ at which $\mathbf{u}_{i,t}$ gives the two dimensional vector at time t.

Now a first rough estimation of a fixed rotation center $\boldsymbol{\omega}_0$ is executed. We further

assume the movement is purely rotational. Therefore, each trajectory has a constant distance r_i to the center. Then the center can be found by minimizing

$$R = \sum_{i,t} |\boldsymbol{\omega}_0 - \mathbf{u}_{i,t}|^2 - r_i^2 \tag{3.1}$$

in a non linear least square fit with $\boldsymbol{\omega}_0$ and r_i as fitting parameters.

Next, we consider the case where the beads are driven by rigid translational drift $\mathbf{T}(t)$ and a rotation described by a rotation matrix

$$A(\gamma(t)) = \begin{pmatrix} \cos\gamma(t) & -\sin\gamma(t) \\ \sin\gamma(t) & \cos\gamma(t) \end{pmatrix}$$

at which $\gamma(t)$ is the angular velocity. As the rotation center has a drift $\mathbf{c}(t)$, the time dependent trajectory function of of bead i starting at position $\mathbf{x}_0$ in the first frame $t = 1$ is given by

$$\mathbf{y}_i = A(\gamma(t))(\mathbf{x}_{0,i} + \mathbf{T}(t) - \boldsymbol{\omega_0} - \mathbf{c}(t)) + \boldsymbol{\omega}_0 + \mathbf{c}(t). \tag{3.2}$$

$$\mathbf{c}(t) = \sum_{t'=1}^{t-1} \mathbf{c}_{t'} + \mathbf{c}_t \text{ for } t > 1, \mathbf{c_1} = 0 \tag{3.3}$$

$$\mathbf{T}(t) = \sum_{t'=1}^{t-1} \mathbf{T}_{t'} + \mathbf{T}_t \text{ for } t > 1, \mathbf{T_1} = 0 \tag{3.4}$$

at which $\mathbf{c}(t)$ and $\mathbf{T}(t)$ are defined recursively. Eq. 3.2 is based on a back- and forth coordinate transformation between the coordinates of the camera frame and the coordinate system in which the rotation axis is placed at position $(0, 0)$. The following example explains the individual terms of the equation. In order to calculate the position in frame $t = 2$ the bead is moved from its starting position to the position $\mathbf{x}_{0,i} + \mathbf{T}(2)$. The coordinate transformation is executed by $-\boldsymbol{\omega_0} - \mathbf{c}(2)$ to prepare the subsequent rotation by $A(\gamma(t))$. Finally the vector is back transformed into the coordinate system of the frame by $+\boldsymbol{\omega}_0 + \mathbf{c}(2)$. Because the frame sequence contains 29000 frames we would have to find 28999 entries for $\mathbf{c}(t)$ and $\mathbf{T}(t)$ as free parameters which would be time consuming. Therefore, we reduce computation time by computing averaged $\mathbf{c}(t)$ and $\mathbf{T}(t)$ for e.g. 1000 frames, respectively. That results in 29 entries for $\mathbf{c}(t)$ and $\mathbf{T}(t)$.

Due to this averaging process we do not consider the real trajectory eq. 3.2 anymore but the averaged trajectory at which also $\mathbf{x}_{0,i}$ becomes a free parameter. We can further simplify the problem and reduce computation time by assuming

$$\mathbf{c}(t) = \mathbf{T}(t). \tag{3.5}$$

This is a justified assumption because the microscope is stable on scales > 10 nm and we do not apply any controlled translational motion. Therefore, any observed translational drift > 10 nm should stem from instabilities of the rotation stage because it is the only moving part of the microscope. We will also see in the results that the assumption is justified. Considering the averaging effect by the binning size b by which the trajectory is

divided into intervals j of constant size and the simplification stated in eq.3.5 the averaged trajectory $\bar{\mathbf{y}}$ for frame t is given through

$$\bar{\mathbf{y}}_i(t) = A(\gamma(t))(\mathbf{x}_{0,i} - \boldsymbol{\omega_0}) + \boldsymbol{\omega}_0 + \mathbf{c}(t) \tag{3.6}$$

$$\mathbf{c}(t) = \begin{cases} \sum_{j'=1}^{j-1} \dot{\mathbf{c}}_{j'} b + \dot{\mathbf{c}}_j (t - (j-1)b) \text{ for } j, t > 1 \\ \dot{\mathbf{c}}_j t \text{ for } j = 1, t > 1. \end{cases} \tag{3.7}$$

where $\dot{\mathbf{c}}_j t$ is the velocity vector of the translational drift in interval j. In order to find the free parameters $(\mathbf{x}_{0,i}, \boldsymbol{\omega_0}, \dot{\mathbf{c}}_j), \gamma(t)$ we minimize

$$R_2 = \sum_{i,t} |\mathbf{u}_{i,t} - \bar{\mathbf{y}}_{i,t}|^2$$

in a non linear least square fit. Here $\bar{\mathbf{y}}_{i,t}$ is the value of $\bar{\mathbf{y}}_i(t)$ at time t. In the fit we use the result of the fit in eq. 3.1 as startparameter. Because we know the rotation velocity we set to

$$\gamma(t) = 1.4/180 \cdot \pi/600 \text{ Hz}$$

and allow only a deviation from this value of $\pm 5\%$ in the fitting process. Note, this setting together with the simplification in eq. 3.5 resemble our knowledge of the drift process which usually is not available in a correction. Thus, the calculated corrected image serves not as a reference gained by common bead tracking but as the optimal result (fig. 3.4.2.D and fig. 3.4.2.H). In general the drift is unknown.

3.3 Drift estimation model - reconstruction method

The drift estimation model presented here is taken from [23] which is an expansion of [22]. The drift estimation was expanded from solely rigid translational drift to additional rigid rotational drift as well as scaling. All three disturbances were allowed to occur simultaneously. Furthermore, the model is solely based on the SMS data. Data stemming from beads were removed from the list before the analysis. We model the disturbances as unknown time dependent polynomial functions, translational two dimensional drift denoted by $\delta_t^{\theta_0}$, angular drift denoted by $\rho_t^{\Phi_0}$ and scaling denoted by $\sigma_t^{\alpha_0}$. The parameters α_0, Φ_0, θ_0 are the true parameters of the polynomial functions. The drift smeared position histogram sequence acquired under these disturbances can be modeled as

$$O_{j,t} = \tilde{f}\big(1/\sigma_t^{\alpha_0} \cdot R_{-\rho_t^{\Phi_0}}(x_j - \delta_t^{\theta_0})\big) + \sqrt{\frac{n_T}{\beta_T}} \nu_{j,t} \epsilon_{j,t} \tag{3.8}$$

$$= f(x_j) + \sqrt{\frac{n_T}{\beta_T}} \nu_{j,t} \epsilon_{j,t}. \tag{3.9}$$

Here $O_{j,t}$ denotes the value for pixel $j \in \{1, .., n\}$ in histogram O_t exhibiting overall n pixels, $\nu_{j,t}$ and $\epsilon_{j,t}$ represent the noise level as two independent normal random variables and R is a two dimensional rotation matrix with angle ρ. The sequence of histograms can also be binned with a binning size β_T into a new sequence $\mathbb{T} = \{0, \beta_T/T, 2\beta_T/T, ..., (T -$

$\beta_t)/T\}$ at which each frame contains more localizations than a single raw one, thereby reducing noise. n_T denotes the number of localizations in such a binned frame. We now apply a Fourier transformation defined as

$$\mathcal{F}_f(\omega) = \int_{\mathbb{R}^2} \mathrm{e}^{-2\pi\langle\omega,x\rangle} f(x)\mathrm{d}x$$

to the drift smeared image sequence in eq. 3.8 where $\omega \in \mathbb{R}^2$. This results in

$$G_t(\omega) \approx \mathcal{F}_f(\omega) + W_t(\omega) = (\sigma_t^{\alpha_0})^2 \mathrm{e}^{-2\pi\langle\omega,\delta_t^{\theta_0}\rangle} \mathcal{F}_f(\sigma_t^{\alpha_0} R_{-\rho_t^{\Phi_0}}\omega) + W_t(\omega).$$

where $W_t(\omega)$ is the Fourier transform of the noise term in eq. 3.8. Note, the approximation is caused by the binning process. In the Fourier domain translational drift becomes a phase given by $\mathrm{e}^{-2\pi\langle\omega,\delta_t^{\theta_0}\rangle}$ which can be separated from rotation and scaling by considering

$$|\mathcal{F}_f(\omega)|^2 = (\sigma_t^{\alpha_0})^4 |\mathcal{F}_f(\sigma_t^{\alpha_0} R_{-\rho_t^{\Phi_0}}\omega)|^2.$$

which does not depend on the translational drift $\delta_t^{\theta_0}$. Thereby, we can define two independent contrast functionals $M_T(\Phi,\alpha)$ and $N_T(\theta)$. By minimizing the first contrast functional we find the according unknown parameters of the drift. $M_T(\Phi,\alpha)$ is based on the analytical Fourier-Mellin transform [23, p. 15] and has the following characteristic when used on $|G_t|^2$:

$$\mathcal{AFM}_{|G_t|^2}(u,v) = \mathcal{AFM}_{|F_t|^2}(u,v) + \mathcal{AFM}_{\mathcal{W}_t}(u,v)$$

where $\mathcal{W}_t(\omega) = |W_t(\omega)|^2 + 2\Re(\mathcal{F}_{f_t}(\omega)\overline{W^t(\omega)})$ and $(u,v) \in \mathbb{Z}\times\mathbb{R}$. Using this characteristic we write the contrast functional for rotation and scaling correction as

$$\begin{aligned} M_T(\Phi,\alpha) = \int_{-v_T}^{v_T} \sum_{|u|\le u_T} \frac{\beta_T}{T} \sum_{t\in\mathbb{T}} \Big| &(\sigma_t^{\alpha})^{-iv} \mathrm{e}^{2\pi i u \rho_t^{\Phi}} \mathcal{AFM}_{|G_t|^2}(u,v) \\ &- \frac{\beta_T}{T} \sum_{t'\in\mathbb{T}} (\sigma_{t'}^{\alpha})^{-iv} \mathrm{e}^{2\pi i u \rho_{t'}^{\Phi}} \mathcal{AFM}_{|G_{t'}|^2}(u,v)\Big|^2 \,\mathrm{d}v. \end{aligned} \tag{3.10}$$

Here $(u_T, v_T) > 0$ are suitable chosen cutoffs. By minimizing the functional one receives the estimator $(\hat{\Phi}_T, \hat{\alpha}_T)$ for the unknown parameters (Φ_i, α_0). These estimations are used to calibrate the Fourier image sequence G_t by

$$Z_t(\omega) = (\sigma_t^{\hat{\alpha}_T})^{-2} G_t\big(1/\sigma_t^{\hat{\alpha}_T} \cdot R_{\rho_t \hat{\Phi}_T}\omega.\big) \tag{3.11}$$

The contrast functional for translational drift correction is given by

$$N_T(\theta) = \int_{\Omega_T} \frac{\beta_T}{T} \sum_{t\in\mathbb{T}} \Big|\mathrm{e}^{2\pi i\langle\omega,\delta_t^{\theta}\rangle} Z_t(\omega) - \frac{\beta_T}{T} \sum_{t'\in\mathbb{T}} \mathrm{e}^{2\pi i\langle\omega,\delta_{t'}^{\theta}\rangle} Z_t(\omega)\Big|^2 \,\mathrm{d}\omega \tag{3.12}$$

where Ω_T denotes a suitable chosen cutoff. It delivers a translational drift estimation $\hat{\delta}_t^{\theta}$. Together with the estimators for scaling and rotation the estimation for the drift corrected image is given by

$$\hat{f}_T(x_j) = \int_{\omega_T} \frac{\beta_T}{T} \sum_{t\in\mathbb{T}} \mathrm{e}^{2\pi i\langle\omega, x_j + \hat{\delta_t^{\theta_T}}\rangle} Z_t(\omega)\,\mathrm{d}\omega,\ j \in \{1,...,n\}$$

It has been shown that in the case of a solely translational drift correction a simple bootstrapping algorithm allows to quantify the statistical uncertainty of the drift estimate [22][23, p. 121-124]. Here the uncertainty is defined by the confidence interval in which 95% of the bootstrap replicates of the drift function are found. The estimated image $\hat{f}$ is then blurred with the bootstrap replicates within the interval to calculate the image $\hat{f}_{0.95}$ which contains the 'true' unknown structure with a probability of 0.95 (fig. 3.4.1). Note, the here presented correction method can not estimate the position of the rotation axis and its time dependent movement. Therefore, it is always placed in the middle of the evaluated FOV. This missing estimation will be implented in the near future.

3.4 Results of drift estimation

This section presents the results of our developed purley data based reconstruction method. We discern two cases: First sole translational motion. Second rotational movement of 1.4° plus additional uncontrolled translational movement stemming from instabilities of the rotation stage during rotation. The results for the first case are presented in fig. 3.4.1. We applied controlled translational movement to stained β-tubulin in HeLa cells at which we used a polynomial of first degree in x-direction and a quadratic polynomial in y-direction. The superimposed image A depicts the uncorrected drift smeared image and the inlaid picture is a zoom in of a fiducial marker. B depicts the result obtained by fiducial marker tracking for which the known drift polynomials were fitted to the bead data (A.inlay of blue curve). C shows the result obtained by our drift estimation method $\hat{f}_T$ using contrast functional eq. 3.12 for which the estimated drift function $\hat{\delta}_t^\theta$ is depicted as light blue curve in the inlaid picture of (A). For better comparison the bottom row shows a zoom in of the white box in the corresponding upper pictures. Although the drift estimate of our reconstruction method $\hat{\delta}_t^\theta$ differs slightly from the fiducial marker tracking there is no visible difference between both methods in picture (B) and (C). Therefore, we deduced that our correction method is as good as fiducial marker tracking for translational drift. Furthermore, a simple bootstrapping algorithm for $\hat{\delta}_t^\theta$ allows to deliver a quality seal to our reconstruction method. Therefor, all bootstrap replicates of $\hat{\delta}_t^\theta$ within its found confidence interval are used to blur image C. Therefore, image D covers the true structure with a probability of 0.95. This seal is not obtainable by fiducial marker tracking. Image D also clearly visualizes the uncertainty of our drift estimation because a high uncertainty would result in a 'blurry' image which might not depict highly resolved structures.

For the second case (fig. 3.4.2) illustrates the two steps executed by our correction method: A depicts the uncorrected superimposed image. In a first step we estimated the rotational drift ρ_t^Φ by contrast functional eq. 3.10. We also estimated the scaling σ_t^α although no scaling was applied as controlled movement during the measurement. These estimates were then used for correction which results in the image B. In the second step these estimates were used to calibrate the Fourier transform of the histograms via eq. 3.11 and subsequently estimate the translational drift $\hat{\delta}_t^\theta$ by contrast functional eq. 3.12. The

result is depicted in C. Image D shows the result found by the extended reconstruction method which uses knowledge of the applied movement. The pictures in the bottom row depict a zoom in of the white box in the corresponding upper picture. We deduced that our estimation method indeed corrects for simultaneous rotational and translational drift. Note, the estimation method operates on pixelized histograms based on the localization list of the markers. Therefore, the result also depends on the chosen pixelation. A,B and C use a pixelation of 512×512 which correspnds to ca. 60 nm pixel size in the images. Image D has a pixelsize of 20 nm. Therefore, the better resolved structure in D also stems from the three times smaller pixel size. In order to discuss this effect and to compare our method to fiducial marker tracking see fig. 3.4.3.

Fig. 3.4.3.A depicts the uncorrected superimposed image. B shows a common fiducial marker correction for translational movement which would be usually executed without knowing anything about the drift. C states the result of our correction method. A comparison between C and D shows that our method clearly delivers the better image estimation because it recognizes the rotational drift. Furthermore, C is also very similar to the result of the extended reconstruction shown in D. Again the bigger pixelsize of 60 nm may significantly impact the result. To demonstrate the impact of pixelation we performed our correction method on one quarter of the originally imaged area, shown in G. Again we chose a pixelation of 512×512 which results in a pixelsize of ca. 30 nm due to the reduced corrected sample area. Under these conditions the result looks very similar to the extended reconstruction image shown in D and H at which H is a zoom in of D. Furthermore, it is clearly superior to the common fiducial marker tracking result depicted in F which is a zoom in of B. Moreover, it is worth to mention that our correction method reconstructed a super resolved image with just a fraction of the original data. A correction by fiducial marker tracking solely on the sub fraction of the image is not possible because it does not contain any bead data. Finally, due to the possibility to reconstruct the image on a fraction of the data our method can avoid erroneous data, for instance events of higher order which occured in the upper left corner of image D.

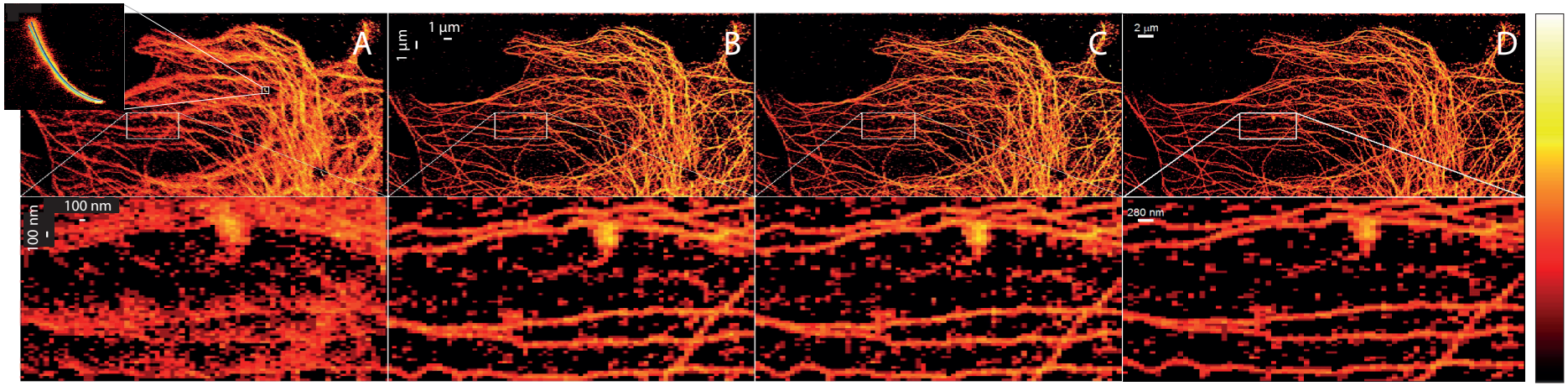

Figure 3.4.1: Image reconstruction for translational drift. A SMS measurement of stained β-tubulin (dye Cage552) in HeLa cells exhibiting overall 40,000 SMS images (51 µm $\times$ 24 µm) was binned into T =2000 frames. The fiducial marker data was removed for the drift estimation and used solely for comparison. A: Superposition of uncorrected data. The inlaid picture shows the trajectory of a fiducial marker. The blue curve is a polynomial fit using the known form of the applied translational movement. The light blue curve is the estimated drift function. B: Reconstruction result by fiducial marker tracking. C: Reconstructed image $\hat{f}_T$ using only the SMS data, no fiducial marker tracking. The reconstruction method is comparable to fiducial marker tracking. D: $\hat{f}_T$ was blurred by the bootstrap replicates within the confidence interval to receive image $\hat{f}_{0.95}$ which shows no visible difference to $\hat{f}_T$. This implicates a high precision of the drift estimate. Furthermore, $\hat{f}_{0.95}$ covers the 'true' structure with a probability of 0.95. Bottom row: Zoom ins of the top picture.

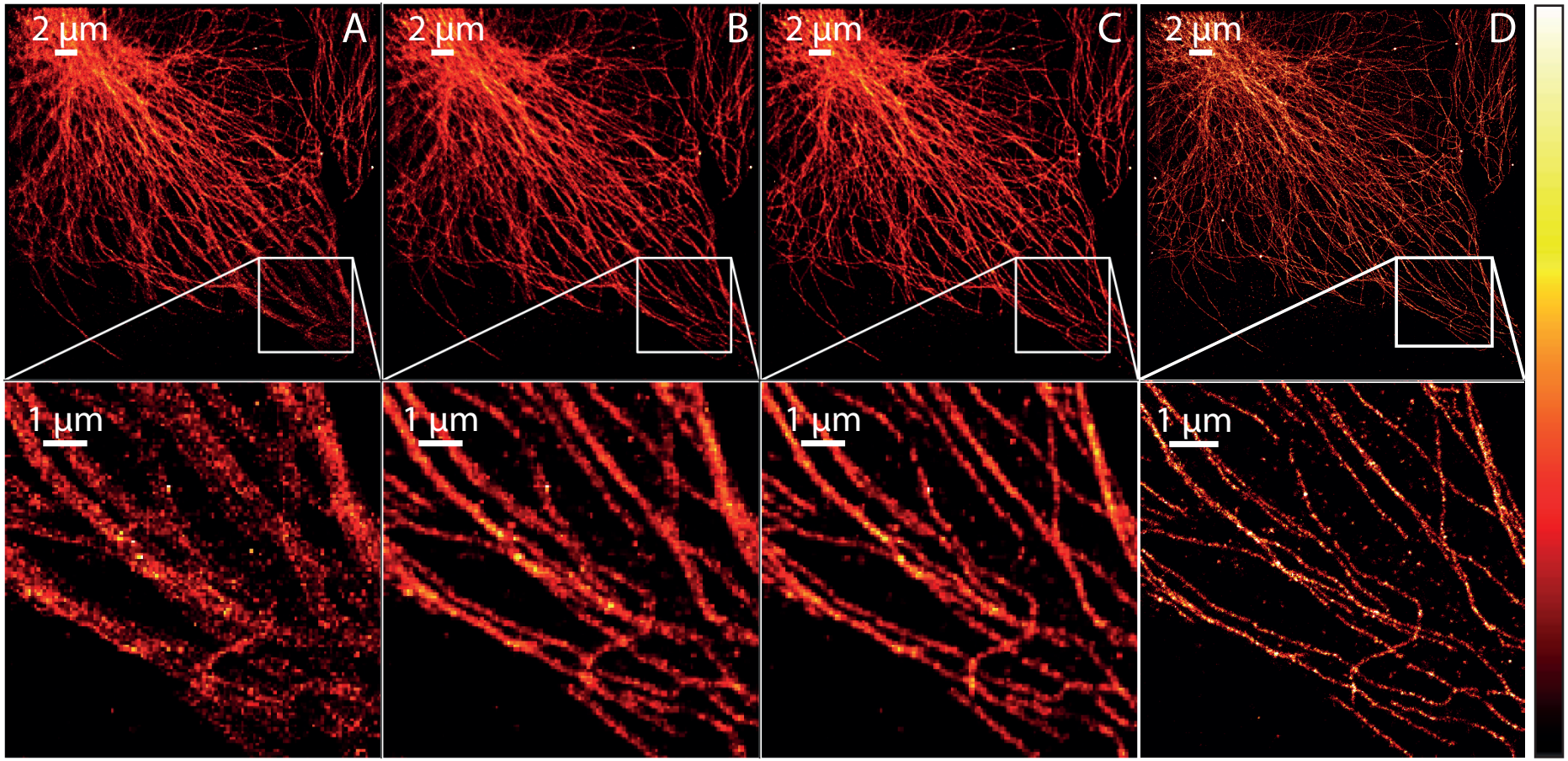

Figure 3.4.2: Image reconstruction for translational and rotational drift. A SMS measurement of stained β-tubulin (dye Flip565) in HeLa cells exhibiting overall 29,000 SMS images (33 µm × 32 µm) was binned into T =100 frames. The fiducial marker data was removed for the drift estimation and used solely for comparison. A: Uncorrected image. B: Image estimation for rotational drift and scaling correction using contrast functional $M_T((\Phi, \alpha))$. C: Image estimation for rotational drift, transaltional drift and scaling correction using contrast functional $M_T((\Phi, \alpha))$ and $N_T(\theta)$. D: Result by extended fiducial marker tracking. This image resembles our knowledge about the applied controlled motion which is usually not available in a common fiducial marker tracking correction. Therefore, it does not state the result obtained by common fiducial marker tracking but the optimal ('true') result.

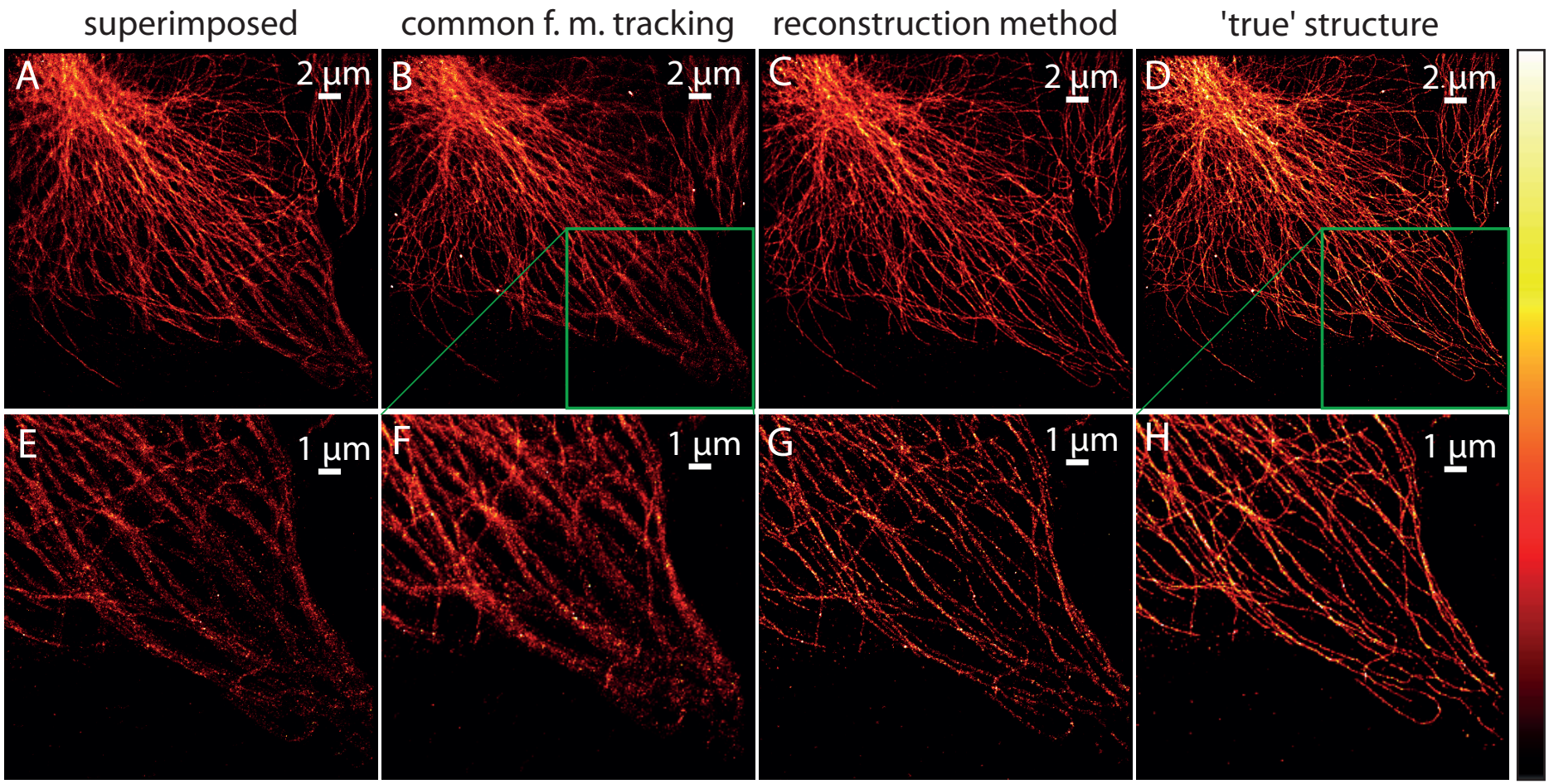

Figure 3.4.3: Image reconstruction for translational drift. A SMS measurement of stained β-tubulin (dye Flip565) in HeLa cells exhibiting overall 29,000 SMS images (33 µm $\times$ 32 µm) was applied to controlled rotational movement of 1.4° and subsequently corrected. (A,E): Uncorrected drift smeared image. Bead data was removed. (B,F): Image corrected by common fiducial marker tracking. The white locations in B stem from the beads. F is a cut out of B. (C,G): Reconstruction method correcting for translational and rotational drift. Note, the reconstruction for C and G are independent. H was reconstructed solely on its shown data. (D,H): Result by extended fiducial marker tracking. This image resembles our knowledge about the applied controlled motion which is usually not available in a common fiducial marker tracking correction. H is a cut out of D.

Chapter 4

Quantitative fluorescence microscopy

Microscopy is an indispensable tool in modern biomedical research. The utilization of fluorescent probes [55] in particular has contributed to its development from a mainly qualitative device to an ever increasing quantitative instrument. For example, fluorescence correlation spectroscopy (FCS) [56] and single-particle tracking [57] can be used to investigate the diffusion and trafficking of molecules [55]. Förster resonance energy transfer (FRET) [58], fluorescence lifetime imaging (FLIM) [59], and fluorescence recovery after photobleaching (FRAP) [60] allow the investigation of conformational changes, molecular interactions and dynamic transport phenomena. As cell biology is transitioning into a quantitative science characterized by increasing integration of modeling into experiment [61], data retrieved from these or other methods are of major importance.

Within this context more and more researchers are interested in counting protein molecules in cells. Such protein numbers are important to define the stoichiometry of functional protein and protein-nucleic acid complexes or to improve structural models. This helps to understand functionality on the molecular scale and provides insights into possible causes of cell diseases [62, 63, 64, 65, 66, 67]. Widely used methods for counting proteins are, inter alia, stepwise photobleaching and ratio comparison to fluorescent standards. Although both methods can utilize standard imaging equipment and do not require specialized analysis software, they are either limited to low protein numbers or rely on trustworthy intensity standards [26]. Recently the upper limit for stepwise photobleaching counting was successfully raised to 20-30 molecules by informing the analysis with the expected physics of the molecules [25]. Still the fundamental problem to reliably identify steps for an increasing number of molecules remains. In addition, these methods are limited by diffraction, which means that they cannot distinguish between structures within an area of about $200 - 250$ nm in diameter. With the advent of 'super-resolution' fluorescene microscopy the diffraction limit has been overcome by switching the signal from individual objects within a diffraction limited region consecutively on and off [68]. Since then, these so-called optical nanoscopes, enable the investigation of cellular structures at

the nanometer scale [69]. To extract quantitative information from super resolved images it is crucial to analyze and exploit both the photophysical mechanisms of the fluorophore and its underlying quantum mechanical behavior. Both determine the observed photon distribution in time and space and by that the super resolved image. [70].

For mapping molecule numbers it is important to differentiate, whether switching of molecular signals is accomplished in a spatially controlled or in a spatially stochastic manner. When, as in STED microscopy [71], the first strategy is applied, there are usually several fluorophores within the focal spot. In this case, the frequency of simultaneous photon arrivals can be used to determine molecule numbers [24]. So far, however, only a very small number of molecules within the focal spot can be counted reliably.

Spatially stochastic switching is applied in single marker switching (SMS) nanoscopy, which subsumes many state-of-the-art techniques known as photoactivated localization microscopy (PALM) [18], stochastic optical reconstruction microscopy (STORM) [15], fluorescence photoactivation localization microscopy (FPALM) [20], PALM with independently running acquisition (PALMIRA) [19], ground state depletion microscopy followed by individual molecule return (GSDIM) [17] or direct STORM (dSTORM) [72]. Here, imaging is performed by assuring that with high probability only a few (random) fluorescent probes are in their on state at any time. Under excitation these probes emit many photons, of which a fraction is detected on an array detector e.g. on a CCD camera. After 1-100 ms, the fluorescent probes switch back to the off state or bleach, so that an adjacent molecule can be read out using the same scheme. The final image is then assembled statistcally by localizing a representative number of molecules and registering them in a position histogram with an average precision which is typically in the range of several 10 nm.

Although individual fluorescent probes are localized within the SMS imaging scheme, counting molecules is not as straightforward as it seems to be. Molecules that have never occupied the bright state will not be registered and therefore lead to undercounting. Furthermore, if several adjacent fluorophores accidentally occupy the bright state simultaneously they will be registered as a single localization which is another source of underestimation [27]. On the other hand, the photophysical properties of fluorophores can cause molecules to repeatedly switch between bright and dark state (blinking), thereby causing overcounting [27] due to multiple localizations of the fluorophore.

A lot of effort has been put especially into resolving the overcounting problem, for example by determining the time interval τ_{crit} between successive blinking events [27, 73]. All localizations separated by times shorter than τ_{crit} are assigned to one fluorophore. A considerable limitation of this method is the need of a priori knowledge of kinetic rates, which must be determined separately. In addition, these rates are not easily transferable from one sample to another, since the photophysical properties of the dyes used in SMS nanoscopy are usually highly dependent on the environment. An approach to overcome this limitation deals with the stochastic nature of photophysical effects by means of a continuous time aggregated Markov model [28]. This Method is not only able to determine

the number of molecules but also the corresponding kinetic constants. This also holds true for other Markov-based approaches [29, 30]. All these approaches to counting molecules are based on the analysis of switching events. Therefore, they are always prone to errors if individual events are not recognized. This is especially the case when many molecules are present within a diffraction limited region or when switching takes place on time scales that are faster or in the range of the image acquisition rate.

Here we introduce an approach to counting molecules based on the analysis of time traces of fluorescence intensity. Our Markov model based method does not require any a priori knowledge of photokinetic rates, nor is it necessary to resolve or recognize individual switching events. It is even not necessary to analyze complete time traces. Although we prove its usability for the widely used Alexa Fluor 647 in a slightly modified GSDIM/dSTORM application, it is not bound to a specific dye or a group of dyes. Furthermore, it is theoretically able to account for 'dark' molecules which have never emitted photons.

4.1 Theoretical framework

4.1.1 Markov model basics

The typical photophysics of a fluorescent SMS probe is depicted in fig. 4.1.1. If it occupies the bright state and is repeatedly excited the probe emits a photon at each spontaneous relaxation until it either irreversibly bleachs by a transition into the bleached state or enters the dark state. From the dark state it can either bleach or reenter the bright state in which it again repeatedly emits photons if it is excited. A transition cycle bright state $\rightarrow$ dark state $\rightarrow$ bright state is called blinking. The fact that blinking can occur illustrates that the behavior of a probe is highly dynamic. Because such state models can explain the time dependent behavior of a probe we will use it to analyze measured fluorescence intensities and deduct the underlying number of fluorescent molecules. In our case the photophysical model is mathematically described by a Markov chain, hence our counting method is based on a Markov model.

Basic knowledge of time-discrete Markov chains is essential to understand our Markov model and our method since in SMS microscopy the imaging camera naturally sets discrete steps for the measured fluorescence trace. Thus, our model considers the occupied state at the end of the camera frames. In the following we will discuss the basics of Markov chains, which we will illustrate by answering two problem-related questions, detailed information is found in [74]: If a single fluorophore starts in the bright state what is the probability to find it in the bright state at the end of the second frame? If a set of m fluorophores starts with a given distribution of the states how many fluorophores populate in average the bright state at the end of the second frame?

Let the states i be elements of the state space I, $i \in I$. A random variable X can take

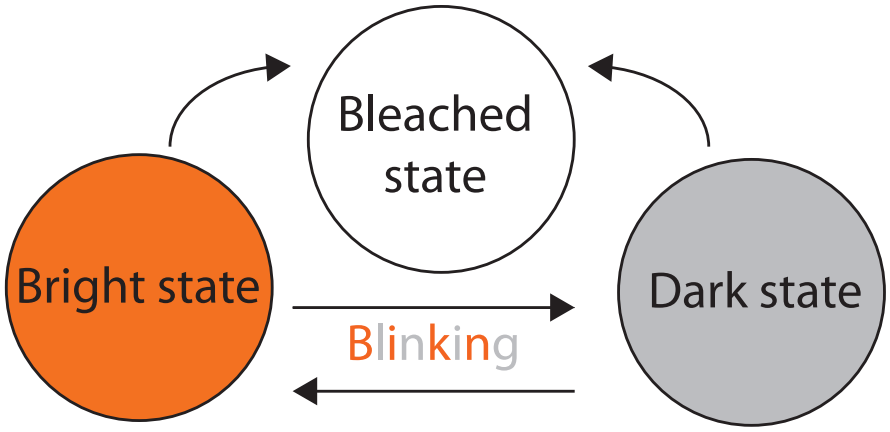

Figure 4.1.1: Typical schematic photophysics of a fluorescent probe for SMS microscopy: Conditioned it is repeatedly excited a fluorescent molecule repeatedly emits photons in the bright state until it either irreversibly bleaches by a transition to the bleached state or enters the dark state. From there it can either bleach or reoccupy the bright state in which it again emits photons if it is excited. A transition cycle bright state → dark state → bright state is called blinking.

values within I. The probability to receive a specific value for X is denoted by

$$\mathbb{P}(X = i) = \lambda_i$$

where λ_i is a measure. We assume that λ is a distribution of X which implicates $\sum_i \lambda_i = 1$. The Markov matrix $P = (p_{i,j} : i, j \in I)$, often called transition matrix, is called stochastic if every row $(p_{i,j}, j \in I)$ is a distribution. For example the Markov matrix for a blinking process, based on the photophysical model shown in Fig. 4.1.2, has the stochastic transition matrix

$$M = \begin{pmatrix} p_{11} & p_{12} & p_{13} \\ p_{21} & p_{22} & p_{23} \\ 0 & 0 & 1 \end{pmatrix}. \tag{4.1}$$

Note, that in the figure the probabilities to remain in the bright state, e.g. p_{11}, are not depicted. We can now define a Markov chain based on the corresponding matrix M: "$(X_n)_{n\geq 0}$ is a Markov chain with initial distribution λ and transition matrix M if

(i) X_0 has distribution λ;

(ii) for $n \geq 0$, conditional on $X_n = i, X_{n+1}$ has distribution $(p_{ij} : i \in I)$ and is independent of $X_0, ..., X_{n-1}$.

We say that $X_n = i, X_{n+1}$ is $Markov(\lambda, M)$." [74, p. 2]. To calculate the probability that a given Markov chains is at a certain state for step n the following theorem is useful [74, p. 2]: " A discrete-time random process $(X_n)_{0\leq n\leq N}$ is $Markov(\lambda, M)$ if and only if for all $i_1, ..., i_N \in I$

$$\mathbb{P}(X_0 = i_1, X_1 = i_2, ..., X_N = i_N) = \lambda_{i_1} p_{i_1 i_2} p_{i_2 i_2} ... p_{i_{N-1} i_N}. \tag{4.2}$$

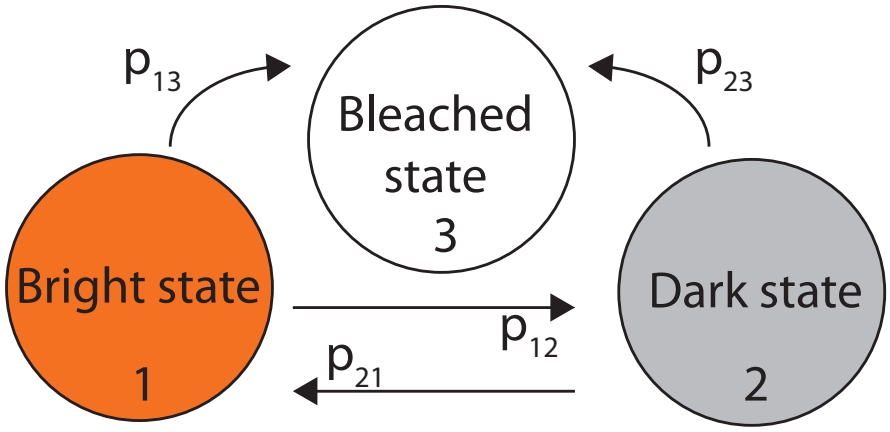

Figure 4.1.2: Connection between photophysics and Markov matrix: The elements p_{ij} of the Markov matrix are transition probabilities of the photophysical model.

Measures and distributions are given by row vectors λ. The measure for state $j \in I$ after one step (frame, transition) is given by

$$(\lambda M)_j = \sum_{i \in I} \lambda_i p_{ij}.$$

Furthermore, M^n denotes n times matrix multiplication of M at which M^0 is the identity matrix. We designate an element of this matrix by $p_{ij}^{(n)} = (M^n)_{ij}$. Measures for an arbitrary number of steps n and starting distribution λ are given by [74, p. 4]

$$\mathbb{P}(X_n = j) = (\lambda M^n)_j \tag{4.3}$$

where conditional probabilities follow as

$$\mathbb{P}(X_{n+m} = j | X_m = i) = p_{ij}^{(n)}. \tag{4.4}$$

With this result we can answer the two questions from the beginning of this section at which we see each step of the discrete chain as a measured frame. Using M from the process in fig. 4.1.2 the probability to find the fluorophore in the bright state after the second step, hence $n = 2$, conditioned it started in the bright state is

$$\mathbb{P}(X_2 = 1 | X_0 = 1) = p_{11}^{(2)} = (p_{11}p_{11} + p_{12}p_{21}).$$

If m fluorophores start with distribution λ the average number of fluorophores in the bright state after the second step for the same M is given by

$$\mathbb{P}(X_2 = 1) = (m\lambda M^2)_1 = m(\lambda_1, \lambda_2, \lambda_3) \cdot \begin{pmatrix} p_{11}p_{11} + p_{12}p_{21} \\ p_{21}p_{11} + p_{22}p_{21} \\ 0 \end{pmatrix}$$

$$= m\lambda_1(p_{11}p_{11} + p_{12}p_{21}) + m\lambda_2(p_{21}p_{11} + p_{22}p_{21}).$$

Linear algebra delivers a useful expression: If matrix M for the K-state chain has K distinct eigenvalues λ then $p_{ij}^{(n)}$ can be written [74, p. 8] by

$$p_{ij}^{(n)} = a_1\lambda_1^n + ... + a_K\lambda_K^n. \tag{4.5}$$

The a_k depend on the starting distribution. Note, this is the sum of K exponentials and it allows to calculate any measures $\mathbb{P}$ for a Markov chain using eq. 4.3 and eq. 4.4. Unfortunately, this result is not sufficient on its own because it does not make any statement about emitted photon numbers.

4.1.2 Markov model for a single fluorophore

A rigorous mathematical analysis of our counting Markov model can be reviewed in [31]. The work at hand gives a shortened overview and at some points additional explanation. Due to the exposure time t_{exp} of the camera in a SMS measurement the detected fluorescence of a target of interest is naturally binned into discrete steps at which we call its time dependent fluorescence Y_t a fluorescence trace which contains photon numbers. The trace is analyzed by or Markov model to evaluate the underlying fluorophore number. For this purpose the model must be able to describe the measured photon numbers. This is done via modelling the distribution of emitted photons Y during one frame. Here Y is a random variable denoting the number of emitted photons. Furthermore, the counting model must consider the binning of the trace, due to the exposure time t_{exp} of the camera, and the resultant resolvable and unresolvable photodynamics. A fluorophore emits a single photon on a timescale of 1 ns [75] and it emits typically thousands of photons before it leaves the bright state. We can only detect photodynamics on timescales slower than t_{exp}. Hence, we cannot observe any transition faster than t_{exp}. To incorporate this condition we split our Markov model in a long time model and a short time model. All fast dynamics are integrated within the bright state and treated by the short time model, represented in Markov matrix M_2. Although we cannot resolve the dynamics within the bright state we are able to decide whether a fluorophore stays in the bright state or leaves it. The long time model, represented in Markov matrix M_1, works on the slow dynamics resolved by the subsequent frames at which it describes the occupied state at the end of each frame. By modelling the occupied state at the end of each frame the discrete nature of the measured fluorescence trace Y_t is accounted for. Finally a connection between the photon distribution of emitted photon numbers during one frame Y and the Markov process described by both matrices M_1, M_2 needs to be established.

In summary we need the distribution of emitted photons Y during one frame, M_1, M_2 and a connection between them.

Long time model

The long time model consists of exactly one bright state, an arbitrary amount of dark states and for convenience one bleached state. We index the states with numbers in the given order so that the bright state is denoted by 1 and the bleached state by the highest number r. Note, within the long time model the bright state cannot be left. The bleached state is defined by the fact that it can never be left in our Markov model. The bright state can only be left in the short time model. So the stochastic $r \times r$ Markov matrix M_1 looks

like

$$M_1 = \begin{pmatrix} 1 & 0 & \dots & \dots & 0 \\ p_{21} & p_{22} & \dots & p_{2,r-1} & p_{2,r} \\ \vdots & \vdots & \ddots & \vdots & \vdots \\ p_{r-1,1} & p_{r-1,2} & \dots & p_{r-1,r-1} & p_{r-1,r} \\ 0 & \dots & & 0 & 1 \end{pmatrix}.$$

Short time model and photon distribution

As mentioned before the short time model shall decide whether a fluorophore stays in or leaves the bright state at the end of a frame. For this purpose it is not necessary to model the fast transition rates within the bright state. If p_{11} denotes the probability that the fluorophore stays in the bright state then $p_{12} = 1 - p_{11}$ is the probability that the fluorophore leaves the bright state. Furthermore, we define that the fluorophore leaves the bright state only via a single dark state of the long time model DL, also called exit state, here indexed by 2. We will see, that this enables a simple connection of the photon distribution with the short time model. Hence, the stochastic $r \times r$ Markov Matrix M_2 looks like

$$M_2 = \begin{pmatrix} p_{11} & p_{12} & 0 & \dots & 0 \\ 0 & 1 & 0 & \dots & 0 \\ \vdots & & \ddots & & \vdots \\ & & & 1 & 0 \\ 0 & \dots & & 0 & 1 \end{pmatrix}.$$

Note, this exit state construction neglects a direct transition from the bright state to the bleached state and to other dark states in the long time model. We now connect both matrices to model the Markov process via $M = M_2 \cdot M_1$. Still the Markov matrix on its own does not make any statement about measured photon numbers. For this purpose lets consider the less general case of $r = 4$ applied to our short time model: It exhibits the states S_0 and S_1 and the before mentioned exit state. Further we introduce an unresolvable short living dark state DS. All four states are depicted in fig. 4.1.3.

The unresolvable states are subsumed within the bright state, hence we also call them internal states. The internal dark state DS is physically reasonabe because many fluorophores show an unstable fluorescent behavior. For instance, in a timespan of several µs they may undergo photoinduced isomerization and back-isomerization of which one isomer is non fluorescent [76]. We will see, that the internal dark state crucially influences the number of emitted photons. Lets call an uninterrupted cycling between S_0 and S_1 a 'miniburst'. It is interrupted by a transition to DS. The life time of DS is much longer than the time of a miniburst. Otherwise a miniburst would not be interrupted. Then the number of emitted photons for one miniburst follow a geometric distribution

$$\mathrm{Geom}(Y = k, p) = (1 - p)^k p$$

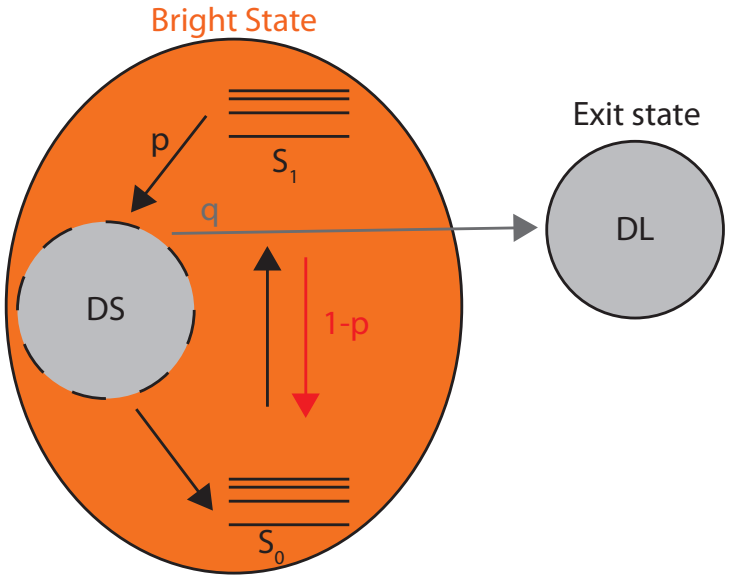

Figure 4.1.3: Short time model: To model a photon distribution it is necessary to examine the internal states of the bright state B. The fluorophore is excited by a transition from S_0 to a vibrational state of S_1 and emits a photon (red arrow) by transitions from S_1 to a vibrational state of S_0. We further introduce an internal dark state DS. The fluorophore 'successfully' transitions to DS with probability p. From DS it may 'successfully' transition to the exit state with probability q. From there it cannot return to the bright state within the same frame.

where $p \in (0,1)$ is the chance for a 'successful' transition to DS, $(1-p)$ is the chance for a 'failed' cycle completion to S0 and k denotes the number of such cycles, hence the number of emitted photons. If the fluorophore resides in DS it has three options. It can leave the bright state by a transition to the exit state with probability $q \in (0,1)$, stay in DS or return to S_0 and start a new miniburst. Therefore, the number of miniburts B during an exposure time of the camera is also a random variable. Thus the total number of emitted photons during one frame is given by the sum of B geometrically distributed random variables which is a negative binomial distribution with parameters p and B:

$$\mathrm{NB}(Y = k, B, p) = \binom{k+B-1}{k} p^B (1-p)^k. \tag{4.6}$$

Here p is the same parameter as in $\mathrm{Geom}(Y)$ and k denotes the number of emitted photons during one frame. This is the before mentioned searched distribution. In order to model the number of minibursts B within one frame we consider two different cases for which we denote the number of minibursts as B'. For the first case assume that the bright state cannot be left, $q = 0$. In this case B' would be given by a binomial distribution. Each time the fluorophore arrives in DS a Bernoulli experiment takes place which consists of the question: Does the fluorophore 'successfully' leave or stay in DS? The probability for a success is a constant each time. The number of successful trials out of overall n trials would be the number of minibursts. But the number of overall trials n is high in our experimental setting because the transition rates within the bright state are much faster than the exposure time of one frame. Also the probability to leave DS via a transition

into the ground state S_0 is small because DS would not be a long living state otherwise.

Therefore, the number of minibursts B' would be given by a Poisson distribution for $q = 0$, $\mu > 0$ and random variable Z:

$$\text{Poisson}(Z = B', \mu) = \frac{\mu^{B'}}{B'!} e^{-\mu}.$$

Note, Z is the number of minibursts under the condition that the fluorophore stays in the bright state during the considered frame. If the fluorophore is allowed to leave the bright state the high number of trials n might not happen. Consider the case that the fluorophore leaves the bright state after a few minibursts. Then each miniburst is a failure described by a geometric distribution with random variable G

$$\text{Geom}(G = B', q) = (1 - q)^{B'} q.$$

We take the minimum of the two independent random variables Z and G to determine B:

$$B = \min(Z, G).$$

This definition implies that we independently roll the number of minibursts with a poisson distribution and with a geometric distribution and then take the smaller value as B. Therefore, B depends on (q, μ), hence the number of photons Y in one frame depends on (p, q, μ). These parameters also determine the probability to leave the bright state, denoted by $p_{12} \in M_2$: The fluorophore leaves the bright state during the frame only under the condition $Z > G$. The probability for such an event [31] is

$$p_{12} = \mathbb{P}(Z > G) = \sum_{z=0}^{\infty} \mathbb{P}(Z = z)\mathbb{P}(G < z) = 1 - e^{-(1-q)\mu} = 1 - p_{11}. \tag{4.7}$$

This is the before mentioned connection between the short time model and the number of emitted photons Y. From the defined distributions of B and Y their expectation values and variances follow as [31]:

$$\mathbb{E}(B) = \frac{q}{1-q}\Big(1 - e^{-(1-q)\mu}\Big)$$
$$\text{Var}(B) = \mathbb{E}(B) + 2\Big(\frac{q}{1-q}\Big)^2\Big(1 - e^{-1(1-q)\mu} - (1-q)\mu e^{-(1-q)\mu}\Big) - \mathbb{E}(B)^2$$

$$\mathbb{E}(Y) = \mathbb{E}(\mathbb{E}(Y|B)) = \frac{p}{1-p}\mathbb{E}(B)$$
$$\text{Var}(Y) = \text{Var}(\mathbb{E}(Y|B)) + \mathbb{E}(\text{Var}(Y|B)) = \Big(\frac{p}{1-p}\Big)^2 \text{Var}(B) + \frac{p}{(1-p)^2}\mathbb{E}(B).$$

$\mathbb{E}(Y)$ is the expected number of photons from one fluorophore during one frame if it starts in the bright state. It is the expectation value of the negative binomial distribution given in eq. 4.6. $\text{Var}(Y)$ is the variance of that distribution. They are the first and second moments of eq. 4.6. Note that our model also allows too calculate higher moments.

Up to this point, we treated Y as the number of emitted photons. Although the emitted photon numbers are fundamentally different from the detected photon numbers,

it can be seen that within the framework of our model the kind of derived distributions does not change [31], provided the excess noise of the EMCCD camera is taken into account (section 4.3.7). Therefore, in the following Y describes the detected photon numbers. Although we cannot predict the complete negative binomial distribution for Y we can state all its moments based on (p, q, μ) [31]. The model also delivers a connection between the moments and the short time model M_2 via eq. 4.7. Due to this connection you can also base the moments of Y on (p, q, p_{12}). Furthermore, the Markov process is described by the combination of short time and long time model $M = M_2 M_1$. Finally, albeit we used the simplification $r = 4$ to derive the distribution of Y, the distribution can be modeled in the same way for an arbitrary r [31]. Still a statement for time dependent expected photon numbers is missing.

Time dependent expected photon numbers

We now want to answer the following question: Given that one fluorophore starts in the bright state how many photons do you expect for frame t? To answer this question we have to calculate $\mathbb{E}(Y_t)$ using our modeled photon numbers Y and the Markov matrix $M = M_2 M_1$ to describe the time dependent process of the fluorophore. Recalling the result of eq. 4.4 we know that the conditional probability to find the fluorophore in the bright state is given by $p_{11}^{(t)}$ and the solution can be expressed by the sum of r exponentials eq. 4.5. Thus the number of expected photons for frame $t \in [1, \infty)$ is given by the product of $\mathbb{E}(Y) \cdot p_{11}^{(t)}$

$$\begin{aligned} \mathbb{E}(Y_t) &= \mathbb{E}(Y) \sum_{k=1}^{r} \alpha_k^0 \lambda_k^{t-1} \\ &= \mathbb{E}(Y) \sum_{k=1}^{r-1} \alpha_k^0 \lambda_k^{t-1} \end{aligned} \tag{4.8}$$

where λ_k are the r eigenvalues of M. Note, the short motivation for this equation is the result of a rigorous mathematical analysis. The last statement used the fact that λ_r equals 1 due to the bleached state which implies $\alpha_r^0 = 0$. At one point the fluorophore is in the bleached state, described by distribution vector $\nu_{\text{bleached}} \in \mathbb{R}^r$ and stays there forever. Then the statement

$$\nu_{\text{bleached}} M = \nu_{\text{bleached}} \cdot \mathbb{1}$$

must be valid. The coefficient α_r is zero because the bleached state does not emit any photons. We note that although eq. 4.8 was justified phenomenologically, the same result is obtained by a strict mathematical analysis.

We now consider the more general case, that the fluorophore may start in any state expressed by the distribution row vector $\nu_0 \in \mathbb{R}^r$. Recalling eq. 4.3 we know the answer for the question of expected photon numbers in frame t is given by

$$\mathbb{E}(Y_t) = \mathbb{E}(Y)(\nu_0 M^{(t)})_1.$$

A rigorous mathematical analysis [31] shows that this breaks down to

$$\mathbb{E}(Y_t) = \mathbb{E}(Y) \sum_{k=1}^{r-1} (\nu_{01}\alpha_k^0 + (1-\nu_{01})\alpha_k^1)\lambda_k^{t-1}. \tag{4.9}$$

Here $\nu_{01} = (\nu_0)_1$ is the probability to start in the bright state and α_k^0, α_k^1 are coefficients depending on ν_0. Even without rigorous analysis it is obvious that additional coefficients must arise in comparison to a single starting state which we assumed for eq. 4.8. Furthermore, the rigorous analysis delivers statements about the time dependent variance $\mathrm{Var}(Y_t)$ and even covariance $\Sigma_{t,t'}$ for two arbitrary time points t, t'.

$$\Sigma_{t,t'} = \begin{cases} \mathrm{Var}(Y_t) = \Big((\theta_3+1)\mathbb{E}(Y_1^0) + f^2 - \mathbb{E}(Y_t)\Big)\mathbb{E}(Y_t) & \text{for } t = t' \\ \Big(\Big(\theta_2 - (1-\theta_2)\frac{p_{11}}{1-p11}\Big)\mathbb{E}(Y_{t-t'}^0) + \frac{1-\theta_2}{1-p_{11}}\mathbb{E}(Y_{t-t'+1}^0) - \mathbb{E}(Y_t)\Big)\mathbb{E}(Y_{t'}) & \text{for } t > t' \end{cases} \tag{4.10}$$

Here the terms $\theta_3 = \frac{\mathrm{Var}(Y)}{\mathbb{E}(Y)^2} - \frac{1}{\mathbb{E}(Y)}$ and $\mathbb{E}(Y_t^0) = \mathbb{E}(Y)\sum_{k=1}^{r-1}\alpha_k^0\lambda_k^{t-1}$ describe the relative excess variance and the number of expected photons for frame t given that the fluorophore starts in the bright state, respectively. If Y is given by a Poisson distribution θ_3 would be zero otherwise $\theta_3 > 0$. The excess noise factor $f^2 = 2$ incorporates the additional noise induced by the amplification register of an EMCCD camera [77]. The parameter θ_2 is fully determined by p_{11}:

$$\theta_2 = -\frac{p_{11}\log p_{11}}{1-p_{11}}.$$

In our Markov model p_{11} is determined by $(\alpha, \lambda, \nu_{01})$ through

$$p_{11} = \frac{\nu_{01}}{\sum_{k=1}^{r-1}\frac{\alpha_k}{\lambda_k}}.$$

Thereby, the free parameters are $(\alpha, \lambda, \mathbb{E}(Y), \nu_{01})$ and their number shrinks if the fluorophore starts in the bright state, $\nu_{01} = 1$. We use this mathematical advantage in our counting study. In the next step we consider m fluorophores. Note, the physical unit in eq. 4.10 of the variance is not directly recognizable as photons squared. This is caused by the characteristics of the Poisson distribution

$$\mathrm{Poisson}(X = x) = \frac{\lambda^x}{x!} \cdot \mathrm{e}^{-\lambda}$$
$$\mathbb{E}(X) = \lambda = \mathrm{Var}(X).$$

Therefore, we simply set the unit to photons squared. For the same reason θ_3 is dimensionless.

4.1.3 Markov model for m fluorophores

We have constructed statements about the expected time dependent photon numbers eq. 4.9 and its covariance eq. 4.10 for one fluorophore. We now expand the model to the more general case of $m \geq 1$ fluorophores. Under the condition that the m fluorophores

fluoresce independently the rigorous analysis shows that all called equations simply scale with m [31]:

$$\mathbb{E}(Y_t) = m\mathbb{E}(Y)\sum_{k=1}^{r-1}(\nu_{01}\alpha_k^0 + (1-\nu_{01})\alpha_k^1)\lambda_k^{t-1} \tag{4.11}$$

$$\Sigma_{t,t'} = \begin{cases} \mathrm{Var}(Y_t) = \frac{1}{m}\Big((\theta_3+1)\mathbb{E}(Y_1^0) + mf^2 - \mathbb{E}(Y_t)\Big)\mathbb{E}(Y_t) & \text{for } t = t' \\ \frac{1}{m}\Big(\Big(\theta_2 - (1-\theta_2)\frac{p_{11}}{1-p11}\Big)\mathbb{E}(Y_{t-t'}^0) + \frac{1-\theta_2}{1-p_{11}}\mathbb{E}(Y_{t-t'+1}^0) - \mathbb{E}(Y_{t'})\Big)\mathbb{E}(Y_{t'}) & \text{for } t > t' \end{cases} \tag{4.12}$$

at which $\mathbb{E}(Y_t^0) = m\mathbb{E}(Y)\sum_{k=1}^{r-1}\alpha_k^0\lambda_k^{t-1}$.

Counting m fluorophores starting in the bright state

As we have expressions for the expected time dependent photon numbers eq. 4.11 and its covariance eq. 4.12 we still need to explain how to calculate m for a measured fluorescence trace Y_t of m fluorophores. Theoretically the maximum likelihood principle would be best to jointly estimate the free parameters $(\alpha, \lambda, \mathbb{E}(Y), \nu_{01})$. Unfortunately, it consists of an astronomically large number of terms such that we were unable to evaluate it even numerically [31]. Therefore, we firstly sought to reduce the number of unknown parameters and secondly approximated the likelihood method. The former is achieved by assuming all fluorophores start in the bright state, $\nu_0 = (1,0,0,0)$, which reduces the complexity of the problem because eq. 4.11 simplifies to

$$\mathbb{E}(Y_t) = m\mathbb{E}(Y)\sum_{k=1}^{r-1}\alpha_k^0\lambda_k^{t-1} = \sum_{k=1}^{r-1}\alpha_k'\lambda_k^{t-1}.$$

This implicates for $t = 1$:

$$m = \frac{\sum_{k=1}^{r-1}\alpha_k'}{\mathbb{E}(Y)}. \tag{4.13}$$

This equation allows us to calculate m for known parameters $(\alpha_k', \lambda_k, \mathbb{E}(Y))$. The latter was achieved by using a pseudo log-likelihood method to estimate $(\alpha_k', \lambda_k, \mathbb{E}(Y))$ [31]. We now shift the focus on the counting experiments.

4.2 Results

4.2.1 Counting Alexa Fluor 647 fluorophores

As we have stated how to calculate fluorophore numbers m from a measured fluorescence trace Y_t we discuss how to verify the results. Verification is achievable by test subjects which exhibit a fluorophore distribution of known shape. For this purpose DNA origami structures are a suitable tool [78]. They consist of DNA bundles in different arrangements. The arrangement is defined by staple strands which connect the DNA strands with each

other in a predetermined way to form the so called scaffold. We use a 12-helix bundle (12HB) with a length of 200 nm. These helices are connected by staple strands to each other to form the scaffold. Fluorophores can be attached to the scaffold by exchanging staple strands with dye-labeled staple-strands. This method is called internal labeling. The labeling efficiency for the origami structures depends on the labeling efficiency of the staple itself and the efficiency of integration into the scaffold. Another way of labeling is to attach binding-sites to each staple and use a complementary strand attached with a fluorophore. This method is called external labeling and comes cheaper but with a lower labeling efficiency than internal labeling. However it is important to understand that whatever method is used not every designed binding position on the origami structure is labeled with a fluorophore because the labeling efficiency is not 100%. Therefore, the number of labeled fluorophores for an origami design is best described by a distribution. Assuming a constant labeling efficiency p for every binding spot of overall n spots the probability to label m fluorophores on one origami structure is given by a binomial distribution

$$\mathrm{Bin}(X = m|p, n) = \binom{n}{m} p^m (1-p)^{n-m}$$

where X is a random variable. To write down a distribution for the ideally counted fluorophore numbers $\widehat{M_{id}}$ of A evaluated origami structures of the same design we have to consider that $X = 0$ is not a reasonable counting result because unlabeled origami structures do not emit any photons. Therefore, these origami structures are indistinguishable from the background and must be ecxludeded as counting results which leads to a conditional binomial distribution:

$$\widehat{M_{id}}(X = m|p, n) = A \cdot \frac{\mathrm{Bin}(X = m|p, n)}{1 - \mathrm{Bin}(X = 0|p, n)} \quad \text{for } m > 0. \tag{4.14}$$

Finally, these test subjects can be immobilized on a BSA-biotin layer by means of two neutravidin molecules attached to the scaffold. Thus they are comfortably found on the cover slip surface.

4.2.2 Photophysics of Alexa Fluor 647 and experimental setup

Our Markov model is not bound to a specific dye and can be adapted to an arbitrary amount of states involved in the photophysical model of the evaluated fluorophore. Note, that the states in the Markov model must not necessarily resemble the states in the real photophysical process. If the photophysical process exhibits several dark states with similar life times the Markov model model will subsume them into a single dark state because they are indistinguishable by our analysis. Although our model is designed with a single bright state it may be successful for a dye exhibiting more than one conditioned the bright states are similar enough. We chose to work with Alexa Fluor 647 because it is a widely used imaging dye due to its high amount of emitted photons per switching event and slow bleaching rate [39]. We found that the photophysical model presented in

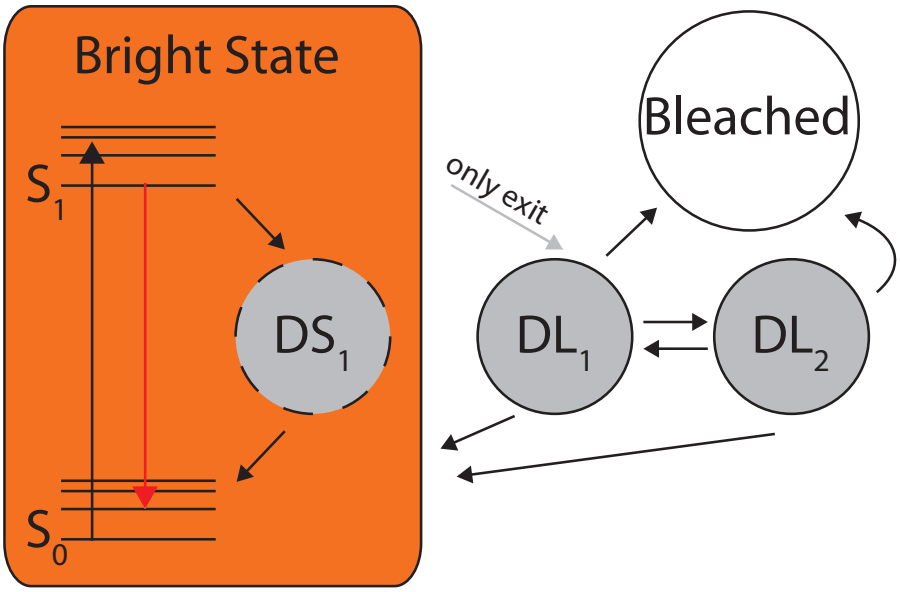

Figure 4.2.1: Photophysical model of Alexa Fluor 647: We use thee dark states DS, DL1, DL2 (grey) which differ strongly in their life times: $\tau_{\mathrm{DS}} \ll \tau$, $\tau_{\mathrm{DL}_1} \geq \tau$ and $\tau_{\mathrm{DL}_2} \gg \tau$. τ=15 ms is the exposure time of a camera frame. Fluorophores fluoresce by transitions from S_1 to vibrational states of S_0, $S_1 \rightarrow S_0$ (red arrow) and can bleach with a transition to the bleached state. Note that all transitions among S_1, S_0, DS are much faster than τ. Thereby, they could not be resolved in our measurements and were treated as a single bright state B (orange). So we used in total four states in our Markov model.

fig. 4.2.1 describes the dye well. Fluorophores fluoresce only by the transition $S_1 \rightarrow S_0$. DL_1 and DL_2 are dark states of our long time model. Because we have used the thiol βME as a buffering ingredient, it is likely that either DL_1 or DL_2 is a thiolated dark state. Here thiolated means, that a βME molecule could have been added to the polymethine bridge via photoabsorption [79, 80]. The bleached state can never be left and DS denotes an internal dark state.

Furthermore, the states differ strongly by their lifetimes. This impacted the measurable photodynamics because the exposure time of our EMCCD camera was set to $\tau = 15$ ms. Therefore, we subsumed the unresolvable dynamics within the bright state B (orange). The lifetime of S_1 is known to be 1.04 ns in a water solution [75]. The lifetime of dark state DS, $\tau_{\mathrm{DS}} \ll \tau$, was unknown. Within DS and B we subsumed all unresolved photophysical processes, e.g. photoinduced isomerization and back-isomerization [76] and possibly another bright state due to encounter complexes formed with the thiol in the buffer medium [80]. Although these processes could not be resolved the existence of DS in our model is experimentally justified due to fluorescence measurements of single Alexa Fluor 647 fluorophores. DS increases the variance of fluorescence photons compared to a model without DS. Transitions among the bright state B, DS_1, DS_2 and the bleached state represent the slow dynamics on timescales ≥ 15 ms. So the number of states r equals four. Note that the chosen number of dark states in the long time model is supported by our study of single Alexa 647 fluorophores.

In our counting study we have imaged immobilized, Alexa 647 labeled origami struc-

tures in a modified GSDIM application. We recorded 20000 subsequent frames with an exposure time of 15 ms. The dye was excited by a continuous 639 nm laser, S0→S1 within B, and activated by a continuous 405 nm UV laser, transition DS_2→B. The modification refers to two experimental conditions: First we used a 5s UV pulse to transfer ideally all fluorophores into the bright state B just before we switched on the excitation light. Second we timed the start of the excitation laser 50 μs after the beginning of a camera frame. The first point ensured that all fluorophores started in the bright state which simplified mathematical analysis within the Markov model, see eq. 4.11. The second point ensured that the very first frame of excited fluorophores could be treated like all subsequent frames since all of them were exposed for 15 ms. Since the Markov model evaluated all frames under the condition of an unchanged environment this is important for the counting analysis. In fig. 4.2.2 a schematic example for a counting measurement is depicted. All fluorophores start in the bright state B. After some time enough dye molecules have entered the dark states and the bleached state such that localization can be performed. All data obtained so far is usually discarded in a common GSDIM measurement. Our Markov model uses this data to determine the number of fluorophores.

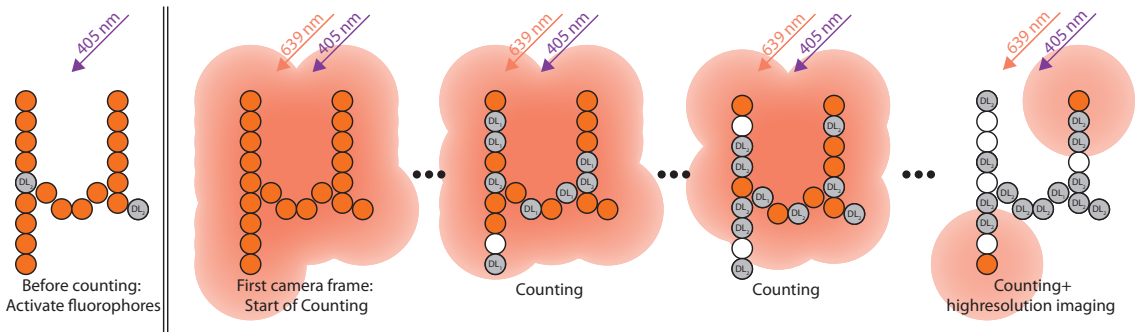

Figure 4.2.2: Example for a counting measurement: Before the measurement is started all fluorophors occupying the thiolated state DL_2 are transferred to the bright state by an UV pulse. Thus, all fluorophores start in the bright state (orange) when the measurement starts. In each frame they can either stay or enter a new state according to our photophysical model. Dark states are shown in grey. As time progresses fluorophores especially aggregate in the long living dark state DL_2 and the bleached state (white). When an adequate number of them are in a dark state or the bleached state the subsequent frames can also be used for localization.

4.2.3 Evaluation process

In fig. 4.2.3 an overview of important steps of our evaluation process is depicted. The first frame indicated the positions of the immobilized origami structures. These positions were the centers of possible evaluation regions, each exhibiting a size of 7x7 pixel, if the regions did not overlap each other. We call the background corrected fluorescence within such a region during all measured frames after activation of the excitation laser the fluorescence trajectory Y_t of fluorescence trace. So each defined evaluation region corresponded to a unique fluorescence trace. We then evaluated Y_t within all selected regions by means of our Markov model to determine the corresponding number of fluorophores. An example

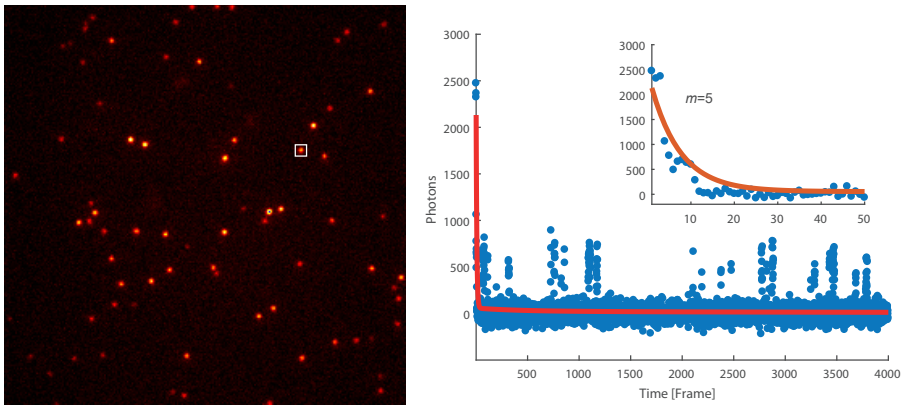

Figure 4.2.3: Left: The first frame of excited fluorophores (33 µm × 33 µm) indicate positions of immobilized origami structures which are possible centers of an evaluation region with a size of 7x7 pixels. If those regions do not overlap each other we chose them for evaluation. The white box indicates a chosen evaluation region. The depicted origami structures have six binding positions for Alexa Fluor 647, origami design (I). Right: Depicted is the corresponding background corrected fluorescence trace Y_t of the indicated evaluation region (blue points) and the result of the evaluation process: The triple exponential function (red line) and the counted fluorophore number m. The inset shows a zoom in on the first 50 frames.

for the evaluation result is depicted in fig. 4.2.3. The background correction is explained in detail in section 4.3.4. Finally, it was even not necessary to evaluate the complete trace. We evaluated only a sub fraction of $n = 4000$ frames of a total of $N = 16040$ frames. These evaluated frames were given by

$$t = \begin{cases} k \text{ for } 0 < k \leq 20 \\ 19 + (k-19)^{\beta} \text{ for } 20 < k \leq n \end{cases}$$

where $\beta = \frac{\log(N-19)}{\log(n-19)}$. This proceeding is possible because our Markov model evaluates the frequency of the bright state occupation in conjunction with the number of detected photons. Therefore, not each transition from or into the bright state must be recognized. This is an advantage compared to other counting methods, which evaluate events, because the reliable registration of an event becomes more difficult as the number of simultaneously fluorescing molecules increases.

4.2.4 Study of single Alexa Fluor 647 fluorophores and counting experiment with known molecule number

In a first step we studied single Alexa Fluor 647 fluorophores attached to DNA origami structures which had several advantages: First these fluorophores certainly fluoresced independently because the observed distances between two origami structures were longer than 200 nm. Second from the study of their fluorescence traces Y_t we were able to determine the number of dark states in the long time model. Third we could also determined the excess variance θ_3 of Alexa Fluor 647 for our experimental setup. Fourth we performed a simulated counting test of known underlying fluorophore number with such traces. Fifth

an analysis of the averaged fluorescence trace stemming from many fluorophores and its variance revealed excellent agreement between observation and model prediction.

As exemplified in fig. 4.2.3 the fluorescence traces show fluorescence in one or more subsequent frames, called a burst, which are separated by random off-times T_{off} during which the fluorophores have not occupied the bright states. The distribution of off times T_{off} can be described by the sum of n exponentials where n also denotes the number of distinguishable dark states involved in the blinking process [27]. We determined that the sum of two exponentials was sufficient to describe the observed distribution of off times shown in fig. 4.2.4 and tab. 4.1. The off times were measured within 457 different fluorescence traces, hence 457 origami structures. Since the triple exponential function only slightly improved the data result, R^2 grows from 0.96 to 0.97, we deduced that two dark states are sufficient for the photophysical model of Alexa Fluor 647. Including the bright and bleached state the total number of involved states r in eq. 4.11, eq. 4.12 and eq. 4.13 is consequently four.

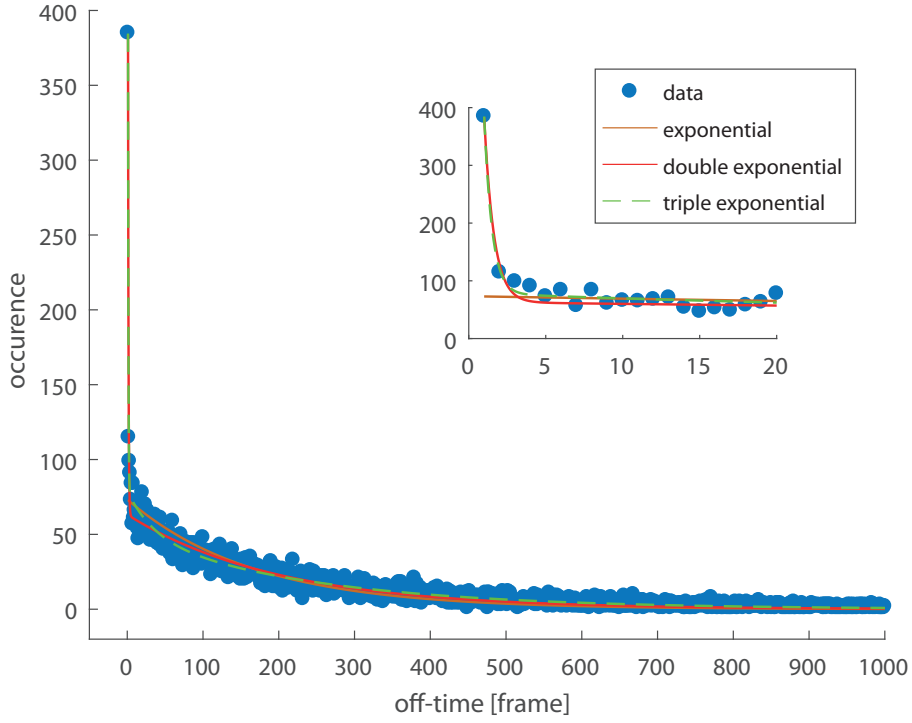

Figure 4.2.4: The distribution of off-times T_{off} (blue dots) of single Alexa Fluor 647 fluorophores for 457 origami structures (IV), hence 457 different fluorescence traces Y_t, is well described by a double exponential fit (red line) or triple exponential fit (green dashed line). Since the double exponential describes the distribution adequately, see also tab. 4.1, we deduce that the number of distinguishable dark states equals two. The inset is a zoom in on the first 20 frames which shows that the single exponential fit (brown) fails to describe $T_{off} \leq 2$.

The excess variance $\theta_3 = \frac{\mathrm{Var}(Y)}{\mathbb{E}(Y)^2} - \frac{1}{\mathbb{E}(Y)}$ was determined within every individual fluorescence trace Y_t by calculating its expectation value $\mathbb{E}(Y)$ and variance $\mathrm{Var}(Y)$. Although the EMCCD-camera introduced additional noise this approach is valid, see section 4.3.7. The resulting distribution of θ_3 is depicted in fig. 4.2.5 and its expectation value is 0.1 which we have used in all counting measurements. Furthermore, this value justifies the

function	parameter	value	95% confidence band
$f = ae^{bx}$	a	73	(71, 76)
	b[1/frame]	$-6.0 \cdot 10^{-3}$	$(-6.3 \cdot 10^{-3}, -5.6 \cdot 10^{-3})$
	R^2	0.72	
$g = ae^{bx} + ce^{dx}$	a	63	(62, 64)
	b[1/frame]	$-5.1 \cdot 10^{-3}$	$(-5.2 \cdot 10^{-3}, -5.0 \cdot 10^{-3})$
	c	1559	(1398, 1720)
	d[1/frame]	-1.6	(-1.7, -1.5)
	R^2	0.96	
$h = ae^{bx} + ce^{dx} + ke^{mx}$	a	29	(27, 32)
	b[1/frame]	$-2.9 \cdot 10^{-2}$	$(-3.4 \cdot 10^{-2}, -2.3 \cdot 10^{-2})$
	c	2147	(1831, 2464)
	d[1/frame]	-1.9	(-2.1, -1.8)
	k	50	(47, 52)
	m[1/frame]	$4.1 \cdot 10^{-3}$	$(4.2 \cdot 10^{-3}, 3.9 \cdot 10^{-3})$
	R^2	0.97	

Table 4.1: Fitting results for the off-times T_{off} of single Alexa Fluor 647 fluorophores using an exponential, double exponential and triple exponential function. The double exponential fit g significantly improves the data description compared to a single exponential fit f as indicated by R^2. The triple exponential fit g slightly improves the description compared to a double exponential fit.

existence of DS_1 in our model. A value close to or equal to zero implies $\mathrm{Var}(Y) = \mathbb{E}(Y)$ which is the case if Y follows a Poisson distribution. However, a Poisson distribution is reasonable if no internal dark state exists and a small transition probability to the exit state and many excitations of a fluorophore during one frame is assumed, see fig. 4.2.1. Both assumptions are adequate for a good fluorophore.

We also tested the Markov model prediction of the variance for the single fluorophore traces Y_t according to eq. 4.12. For this purpose we averaged all single fluorophore traces and fitted eq. 4.11 to determine the parameter $(\alpha_k, \lambda_k, \mathbb{E}(Y))$. The parameter m and ν_{01} equaled one because we work with traces of single fluorophores. With the found parameters we plotted a model prediction of the variance and compared it with the observed variance depicted in fig. 4.2.6. The model prediction and observed variance are in good agreement which implies that our Markov model successfully describes the relation between fluorescence and its variance for single Alexa Fluor 647 molecules.

We also performed a counting test with known molecule number by repeatedly adding up six and fifty traces from a pool of 255 different single fluorophore traces, respectively fig. 4.2.7.A. For the first we used a measured origin trace Y_t only one time such that the added traces $Y_{t,6}$ do not share the same origin trace. For the latter we randomly chose fifty origin traces so that the added traces $Y_{t,50}$ may share one or several origin traces. Then we estimated the number of fluorophores for the added traces by means of our Markov model.

The results are depicted in fig. 4.2.7.B. The mean values of both counting distributions are close to the expected counting result, mean($Y_{t,6}$)=7 and mean($Y_{t,50}$)=52, so we deduce that our model successfully counts independent fluorescing molecules. Furthermore, it is worth mentioning that the added traces exhibit increased noise compared to the source traces due to the adding. Albeit this obstacle the results are quiet good and a molecule

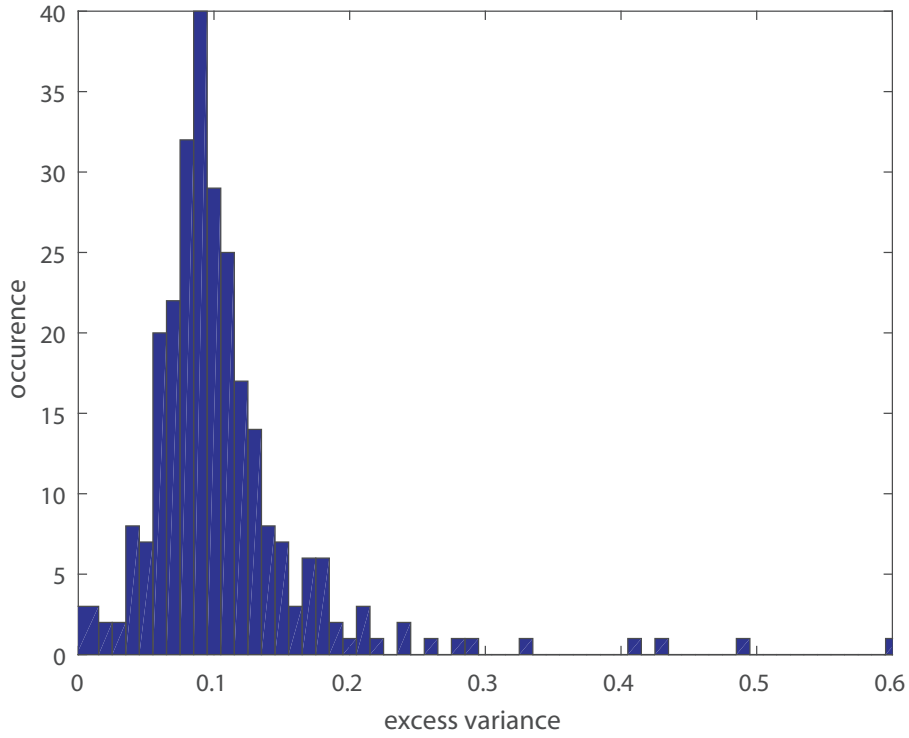

Figure 4.2.5: Distribution of determined excess variances θ_3 of single Alexa Fluor 647 fluorophores: From each individual fluorescence trace Y_t a value for its excess variance is determined by calculating the expectation value $\mathbb{E}(Y)$ and variance $\mathrm{Var}(Y)$ of the fluorescence trace. The mean value of the shown distribution using values $\theta_3 < 0.3$ is $\mathrm{mean}(\theta_3) = 0.1$

estimation for a measured trace should perform even better because of the better signal-to-noise ratio.

Note, $Y_{t,6}$ and $Y_{t,50}$ needed additional background correction which is explained in section section 4.3.5. In the next experiment we examined the more realistic case of adjacent fluorophores which were separated by distances in the nm regime.

4.2.5 Influence of intermolecular distance

From the distances larger than 200 nm between fluorophores in the simulated counting experiment we reduced the inter fluorophore distances d to the nm regime, 6.5 nm$< d <$ 18 nm by using a specific origami design (III) depicted in fig. 4.2.8. It exhibits two quotas of binding positions which are 120 nm apart. Each quota contains 11 binding positions whose exact position on the origami scaffold is only known by the supplier Gattaquant. Therefore, we do not know the specific distances between the binding positions. We performed the evaluation process mentioned in section 4.2.4 on measured fluorescence

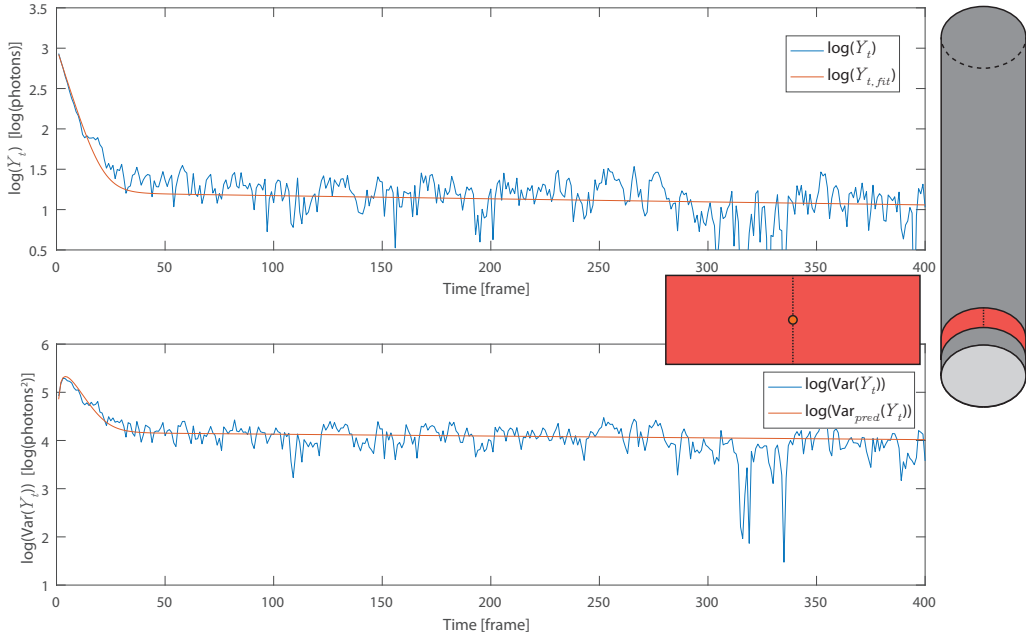

Figure 4.2.6: Top: The blue line depicts the averaged fluorescence trace of origami design (IV) exhibiting one binding position, hence a single or no fluorophore. The orange line is a fit to the data to determine the parameters $(\alpha_k, \lambda_k, \mathbb{E}(Y))$ of eq. 4.11 at which $\{m, \nu_{01}\} = 1$ is known. Bottom: With the fitted parameters we plot the prediction of the fluorescence variance according to eq. 4.12 (orange) and find it in good agreement with the observed variance (blue).

traces of this origami design. The resulting distribution of fluorophore numbers $\widehat{M}$ is depicted in fig. 4.2.8.

Due to the stochastic nature of the labeling process of each origami structure $\widehat{M}$ should ideally be equal to $\widehat{M_{id}}$ given by eq. 4.14. In order to explain this deviation we supposed that the fluorophores interacted with each other due to the inter binding spot distances in the nm regime. On this scale a possible process for interaction between dye molecules is FRET [32, p. 263]. Because our Markov Model does not account for interactions the resulting counting distribution $\widehat{M}$ would not resemble the real distribution of fluorophore numbers.

In order to test this hypothesis we examined fluorophores with known distances between them by means of four origami designs. They exhibited maximal two fluorophores due to two binding spots on the scaffold. The distances between the spots were 4 nm (V), 6.5 nm (VI), 14 nm (VII), 120 nm (VIII) for the specific origami designs, respectively. If our hypothesis is true, the empirical variance of all averaged fluorescence curves of an origami design should be insufficiently explained by our Markov model for small intermolecular distances. Here, unlike for the single fluorophore measurements the number of fluorophores was either one or two due to the stochastic nature of the labeling process. Therefore, an averaged fluorescence trace of designs (V,VI,VII,VIII) had an underlying

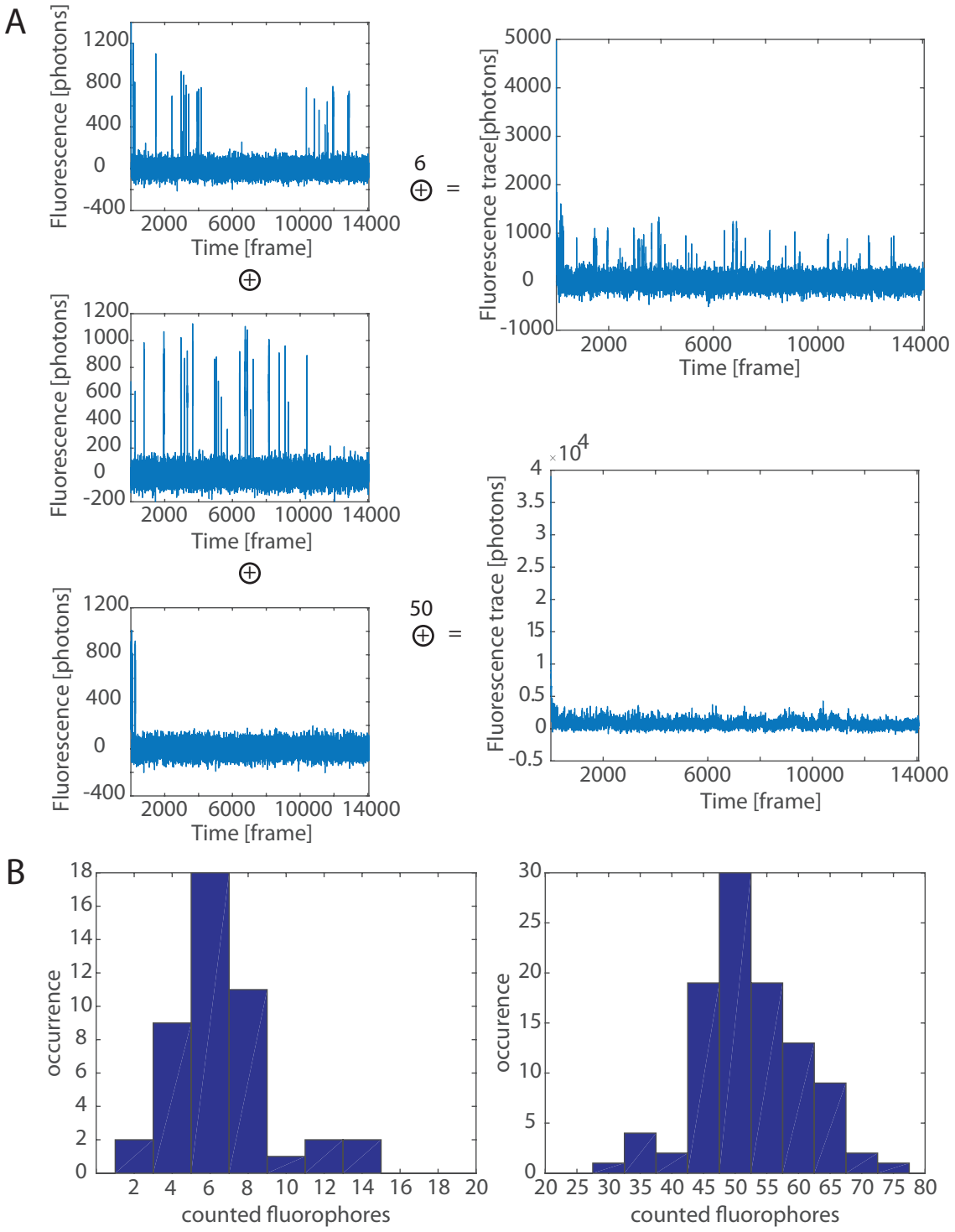

Figure 4.2.7: A: The left side depicts different several single fluorophore traces Y_t. Adding six and fifty of such traces results in $Y_{t,6}$ and $Y_{t,50}$, respectively. The added traces are depicted on the right side and illustrate the increased noise compared to the source traces due to the adding process. B.left: Histogram of counting results for overall 45 $Y_{t,6}$. The single fluorophore traces were chosen in a way that $Y_{t,6}$ do not share one or several source traces. The expected counting result is 6 and the mean of the depicted distribution is 7. B.right: Histogram of counting results for overall 100 traces $Y_{t,50}$ of which each was generated by adding 50 random single fluorophore traces. The expected counting result is 50 and the mean of the depicted distribution is 52.

molecule distribution M for which we had to adapt eq. 4.11 and eq. 4.12 accordingly [31]:

$$\mathbb{E}(Y_t) = \mathbb{E}(M)\mathbb{E}(Y)\sum_{k=1}^{r-1}\alpha_k^0\lambda_k^{t-1} \tag{4.15}$$

$$\begin{aligned}\mathrm{Var}(Y_t) = &\frac{1}{\mathbb{E}(M)}((\theta_3+1)\mathbb{E}(Y_1^0)+\mathbb{E}(M)f^2-\mathbb{E}(Y_t))\mathbb{E}(Y)\\ &+\mathrm{Var}(M)(\mathbb{E}(Y_t)/\mathbb{E}(M))^2\end{aligned} \tag{4.16}$$

with the expectation value $\mathbb{E}(M)$ and variance $\mathrm{Var}(M)$. Assuming a conditional binomial distribution for the probability to successfully label m fluorophores M is given by eq. 4.14 where $n = 2$ denotes the number of dye conjugated staple strands, A the number of evaluated origami structures of the specific design, X the random variable and p the labeling efficiency. Then expectation value and variance follow as

$$\mathbb{E}(M) = \frac{np}{1-(1-p)^n}$$

$$\mathrm{Var}(M) = \frac{np(1-p)+(np)^2}{1-(1-p)^n} - E(M)^2$$

and are fully determined by p and n. Note, because these designs exhibited maximal two fluorophores we were able to determine the labeling efficiencies p for these origami designs and subsequently calculate $\mathbb{E}(M)$ and $\mathrm{Var}(M)$, see section 4.3.6. The results are listed in tab. 4.2.

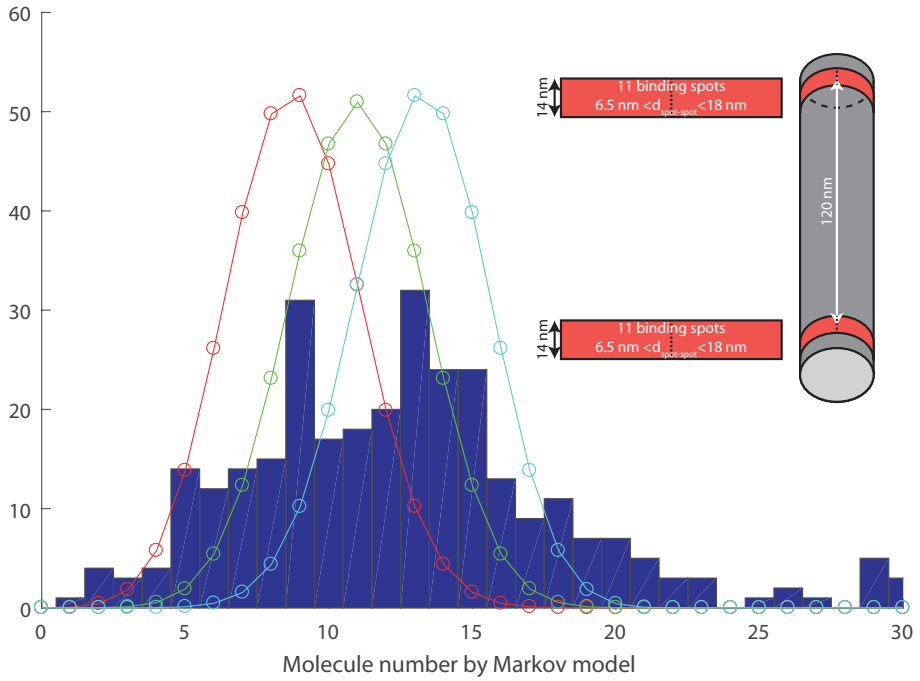

Figure 4.2.8: Illustrated are the counting results $\widehat{M_{III}}$ for $A = 303$ origami structures (III) and its design. The design exhibits overall 22 binding spots allocated within two quotas which contain 11 binding spots each. The minimum distance between two labeled fluorophores is 6.5 nm. $\widehat{M_{III}}$ cannot be described by any Binomial distribution $A \cdot \mathrm{Bin}(X = m|n = 22, p)$ resembling the stochastical labeling process of the given origami design.

origami design	p	$\mathbb{E}(M)$	$\mathrm{Var}(M)$
O-V	0.74	1.6	0.24
O-VI	0.69	1.5	0.25
O-VII	0.40	1.2	0.19
O-VIII	0.43	1.3	0.2

Table 4.2: Determined labeling yields p and corresponding expectation value and variance of the conditional distribution M.

Note, each origami design was measured on a different day under slightly different buffer conditions. These day to day differences of the buffer medium cause varying fluorophore properties, e.g. $\mathbb{E}(Y)$, for the different designs. Therefore, a comparison of fluorophore properties between different designs is not valid for our data. This is not a problem because we relate the fluorescence and its variance only for origami structures of the same design, hence the same buffer conditions.

A fit of the averaged fluorescence trace according to eq. 4.15 then delivered the missing parameters $(\alpha_k^0, \lambda_k, \mathbb{E}(Y))$ which subsequently enabled us to plot the predicted variance according to eq. 4.16 and to compare it with the observed variance. The results are depicted in fig. 4.2.9, fig. 4.2.10, fig. 4.2.11, fig. 4.2.12 and are based on 317, 382, 535 and 489 origami structures, respectively. For inter binding spot distances smaller than 14 nm the Markov model describes the variance during the first frames of the measurements unadequately. As time progresses the prediction becomes correct which is a reasonable result if you presume that fluorophores only interact with each other while simultaneously occupating the bright state. The first frames have a high probability to find both fluorophores in the bright state because both start in it. As time progresses it becomes more likely to observe just one fluorophore in the bright state which is the fundamental principle of GSDIM. Then the two fluorophores presumably cease to interact. For distances longer than or equal to 14 nm our Markov model predictions of the variance are in good agreement with the observation. This result indicates that Alexa Fluor 647 molecules fluoresce dependently for sufficiently small distances between fluorophores. Further it supports our hypothesis of interacting molecules in the experiment with origami design (IV).

Based on this results we analyzed origami designs of sufficiently large inter binding spot distances to perform counting experiments with independent fluorophores.

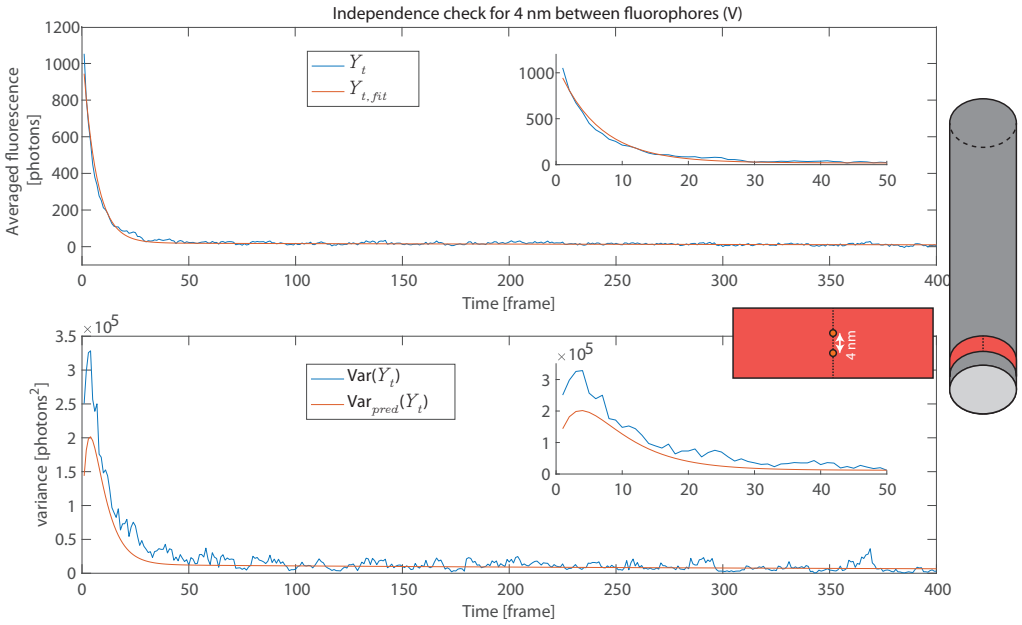

Figure 4.2.9: Top: Averaged fluorescence trace of origami design (V) depicted in blue. The orange line represents a fit to the fluorescence according to our Markov model eq. 4.11. The inlaid picture shows the first 50 frames. Bottom: Variance of the averaged fluorescence (blue) and the prediction of the variance (orange) according to Markov model eq. 4.12. Because unknown parameters are determined by the fluorescence fit the prediction is based on the fit. Our Markov model inadequately predicts the variance.

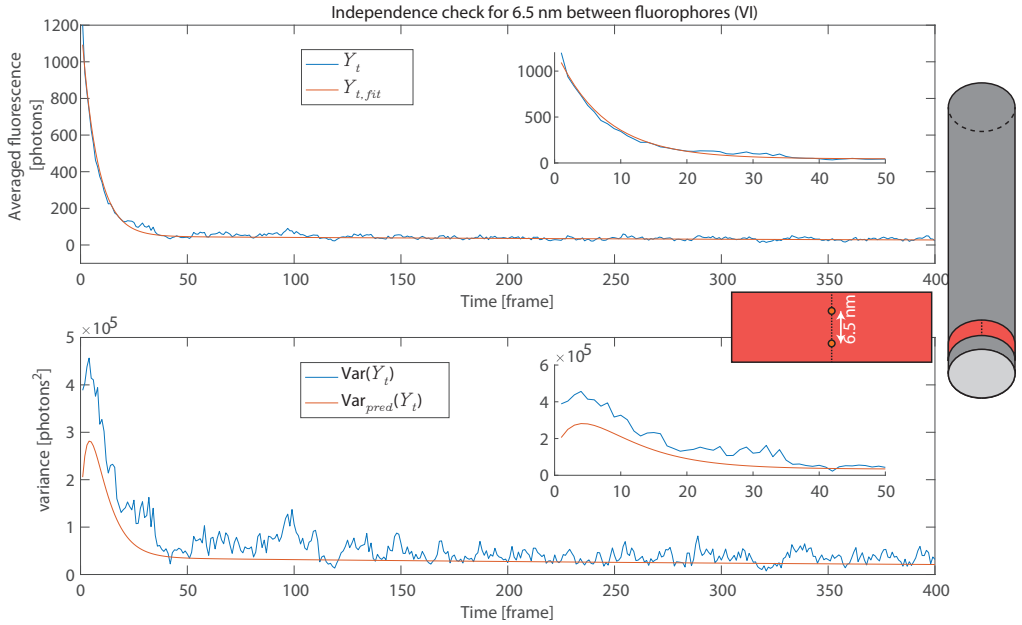

Figure 4.2.10: Top: Averaged fluorescence trace of origami design(VI) depicted in blue. The orange line represents a fit to the fluorescence according to our Markov model eq. 4.11. The inlaid picture shows the first 50 frames. Bottom: Variance of the averaged fluorescence (blue) and the prediction of the variance (orange) according to Markov model eq. 4.12. Because unknown parameters are determined by the fluorescence fit the prediction is based on the fit. Our Markov model inadequately predicts the variance.

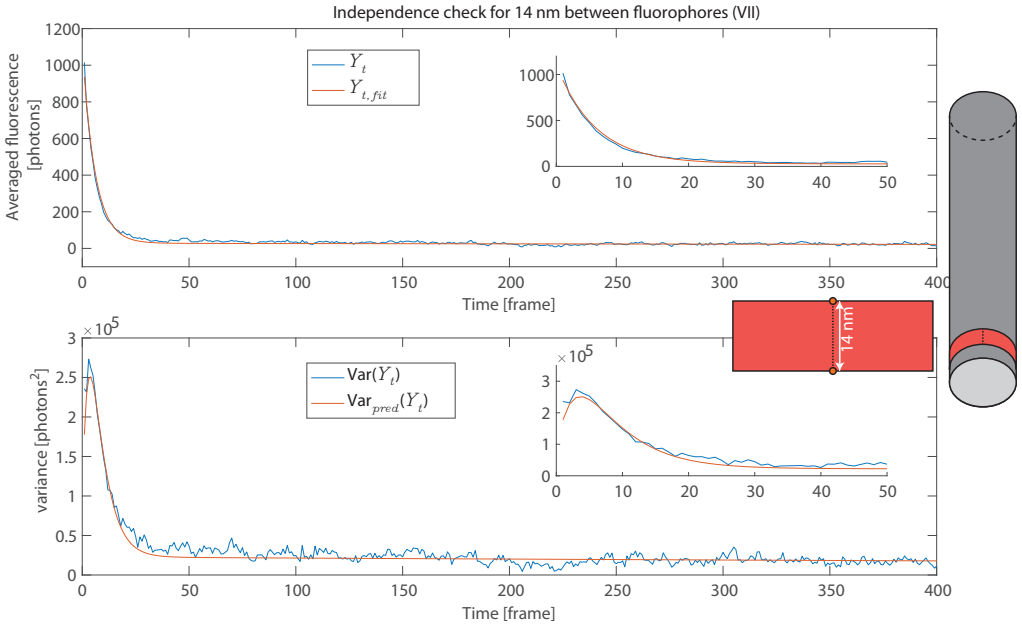

Figure 4.2.11: Top: Averaged fluorescence trace of origami design (VII) depicted in blue. The orange line represents a fit to the fluorescence according to our Markov model eq. 4.11. The inlaid picture shows the first 50 frames. Bottom: Variance of the averaged fluorescence (blue) and the prediction of the variance (orange) according to Markov model eq. 4.12. Because unknown parameters are determined by the fluorescence fit the prediction is based on the fit. Our Markov model adequately predicts the variance.

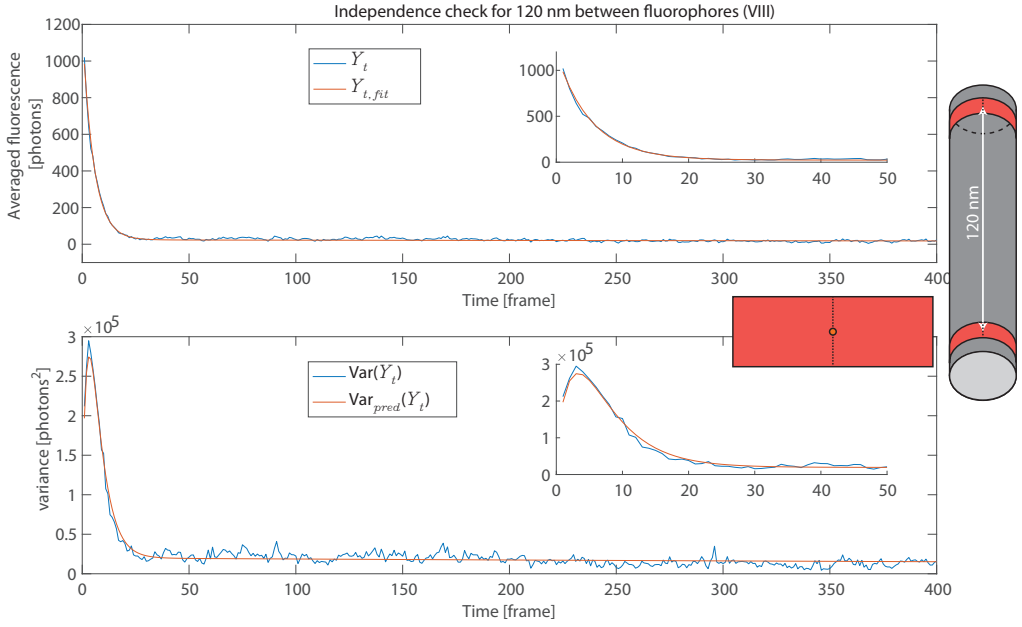

Figure 4.2.12: Top: Averaged fluorescence trace of origami design (VIII) depicted in blue. The orange line represents a fit to the fluorescence according to our Markov model eq. 4.11. The inlaid picture shows the first 50 frames. Bottom: Variance of the averaged fluorescence (blue) and the prediction of the variance (orange) according to Markov model eq. 4.12. Because unknown parameters are determined by the fluorescence fit the prediction is based on the fit. Our Markov model adequately predicts the variance.

4.2.6 Unbiased counting experiment with adjacent fluorophores

Based on the results in fig. 4.2.9, fig. 4.2.10, fig. 4.2.11 and fig. 4.2.12 we analyzed origami designs exhibiting inter binding spot distances larger or equal to 14 nm because according to our hypothesis of interacting fluorophores estimations of molecule numbers should be successful for these designs. In order to perform an unbiased counting experiment we analyzed origami designs (I) and (II) exhibiting inter binding spot distances of 14 nm and 28 nm, respectively. The overall binding spots, six for design (I) and four for design (II), are equally apportioned among two quotas which are 120 nm apart on the scaffold.

The pseudo log-likelihood estimation yielded the counting results $\widehat{M_I}$ and $\widehat{M_{II}}$ (blue) for the respective designs depicted in fig. 4.2.13 at which the first result is based on 297 origami structures and the second on 380. $\widehat{M_I}$ and $\widehat{M_{II}}$ are in good agreement with their respective ideal condotional binomial distribution given by eq. 4.14. This ideal distributions were determined by fitting the unknown labeling efficiency p of eq. 4.14. Because the estimated results are well described by expected conditional binomial distributions we stress that our model successfully counts independent fluorescing fluorophores. The results also show that our counting method is error-prone, because all counts with $m = 0$ must be wrong since we have detected fluorescence in the first frame. The difference between the conditional binomial distribution and the estimation result must not be an error because the labeling efficiency p for each spot of an specific origami design must not be the same. In such a case the expected result would look differently.

Furthermore, we applied a simplified estimation based on eq. 4.13 using

$$m_G = \frac{I(t=1)}{\overline{I}_{\text{blink}}}.$$

Here the sum $\sum \alpha_k^{'}$ is substituded by the measured brightness $I(T = 1)$ in the first frame and $\mathbb{E}(Y)$ is substituded by the average blink photon number $\overline{I}_{\text{blink}}$. The latter is calculated by averaging all registered events within one trace at which we discarded the first frame of a burst because according to the definition of $\mathbb{E}(Y)$ it is the expected photon number conditioned the fluorophore starts in the bright state. This is not necessarily fulfilled for the first frame of a blink. The results of the simplified estimator $\widehat{M_{I,s}}$ and $\widehat{M_{II,s}}$ (orange) are depicted in fig. 4.2.13 which are very close to the pseudo log-likelihood results. Note, albeit a simplified estimation is straight forward to use, on its own it lacks the ability to make any statement about mutual independence of the molecules on which it is based. The Markov model delivers such a statement, illustrated in fig. 4.2.9, fig. 4.2.10, fig. 4.2.11, fig. 4.2.12. Although in the case of mutual independence the results for both methods are similar this is not the case for biased counting depicted in fig. 4.2.14. Therefore, similar results of both methods could be used as an additional indicator to verify unbiased counting in future experiments.

There are several possible causes of failure in our pseudo log-likelihood estimation: First our evaluation method is not perfect and has some internal error. For instance the algorithm for maximizing the pseudo log-likelihood does not find the global minimum. We also know that the results are sensitive to an offset in the fluorescence traces Y_t. Thus an

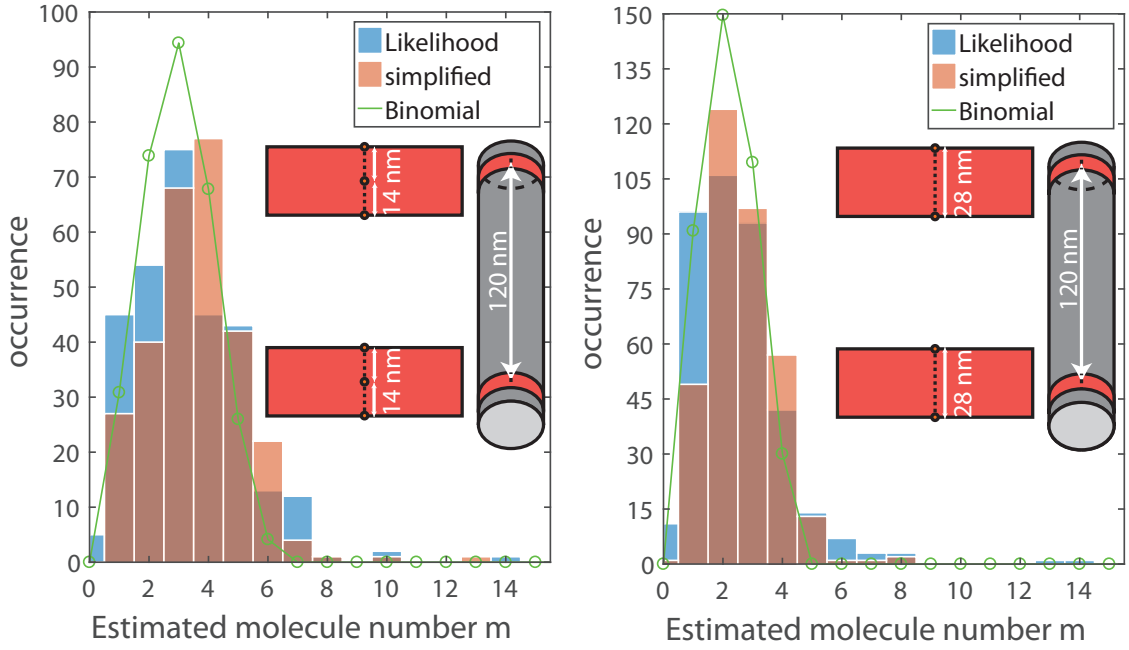

Figure 4.2.13: Estimated molecule numbers for origami designs (I) and (II) exhibiting 6 (left) and 4 (right) labeling positions. The blue $\widehat{M_I}$, $\widehat{M_{II}}$ and the orange histograms $\widehat{M_{I,s}}$, $\widehat{M_{II,s}}$ show the results of the pseudo log-likelihood and the simplified estimator, respectively. The green plot resembles a conditional binomial fit to the pseudo log-likelihood result with the labeling efficiency p as free parameter according to eq. 4.14 and yielded $p_I = 0.49$ for n=6 and $p_{II} = 0.52$ for n=4.

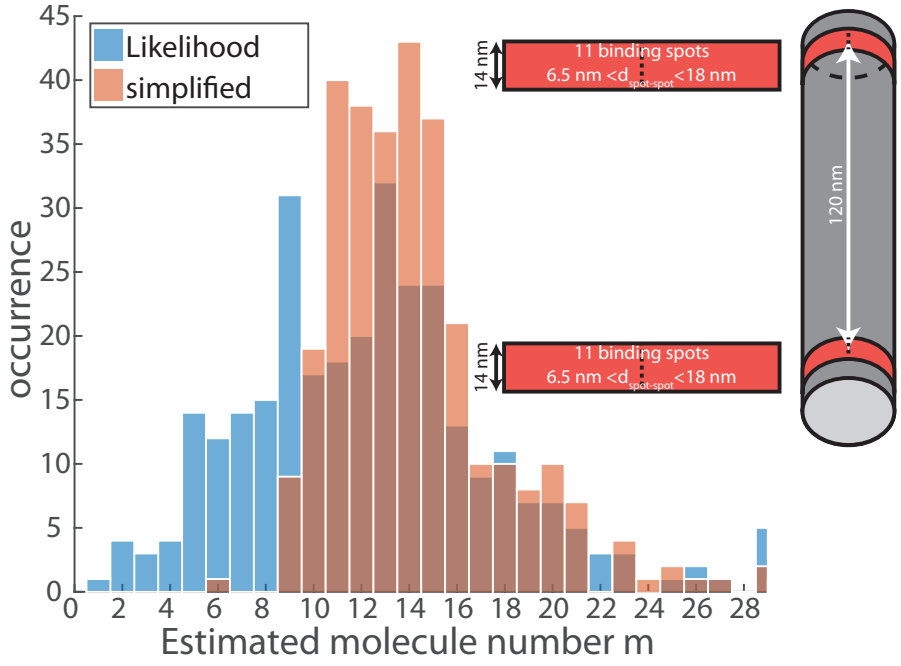

Figure 4.2.14: Biased estimated molecule numbers for origami design (III) and its design. The blue $\widehat{M_{III}}$ and the red histograms $\widehat{M_{III,s}}$ show the results of the pseudo log-likelihood and the simplified estimator, respectively. $\widehat{M_{III}}$ and $\widehat{M_{III,s}}$ differ strongly from each other in contrast to the unbiased counting results.

insufficient background correction influences the result. Another error source is an incomplete transfer of molecules from the dark states to the bright state before the beginning of an measurement, thereby violating our assumption that all fluorophors start

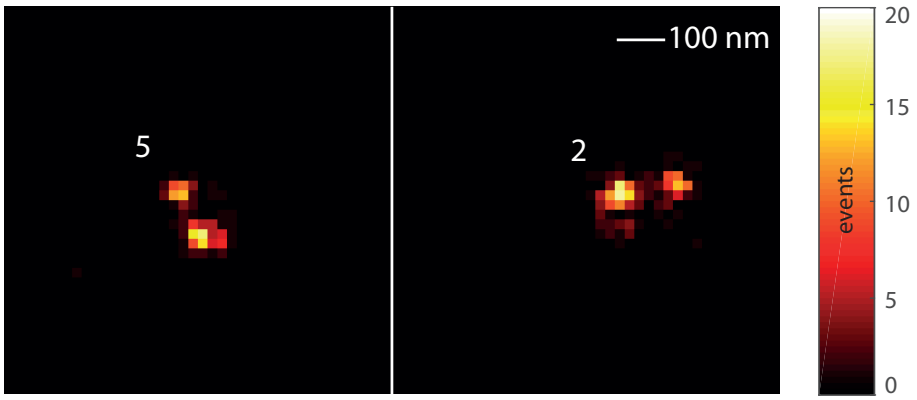

Figure 4.2.15: Two evaluation regions with corresponding counted fluorophore number of origami design (I). Each origami exhibits overall six binding positions for fluorophores.

in the bright state. Our estimation method also assumes that the experimental environment condition do not change in time. Therefore, a varying laser power of excitation and activation can influence the result.

As shown in fig. 4.2.2 we connected molecule counting with high resolution imaging by labeling the high reolution image of an evaluation region with the corresponding determined molecule number. This is shown in fig. 4.2.15 for two evaluation regions of origami design (I). It illustrates that the widely used position histograms give a wrong impression of the fluorophore numbers within the super-resolution image. Although the number of localizations (events) is similar in both images the number of molecules differ by more than a factor of two. Thus, the possible misinterpretation demonstrates the need for quantitative analysis in super-resolution techniques.

4.3 Materials and methods

4.3.1 Fluorescence microscope and measurement protocol

For imaging we used an inverted, modified Leica DM IRE2 microscope. Two continous wave lasers generated the excitation wavelength 639 nm (LightCube Revolution 770, HB-Laser) and the activation wavelength 405 nm (OBIS 405 LX,Coherent). Both wavelengths were combined by a dichroic mirror (zt 442 RDC, AHF). Fluorescence light was separated by a dichroic mirror (zt 642 rdc, AHF), too. The intensities at the center of the Gaussian shaped excitation and UV beam inside the objective plane were ca. 0.6 kW/cm^2 and 0.07 kW/cm^2, respectively. For imaging we used an oil immersion objective with an numerical aperture of 1.4 (UPLSAPO 100xO, Olympus). A band pass filter (705/100 ET, AHF) in front of the recording EMCCD-camera (iXon 897,Andor) defined our spectral detection bandwith and a notch filter (zet635NF,AHF) blocked the excitation wavelength additionally. The magnification of the optical detection system was adjusted such that one pixel of the EMCCD accorded to a lateral distance of 130 nm within the image plane. Due to an electronically tunable bandpass filter (AOTFncC-VIS-TN, AA Optoelectronics) we could reliably switch on the excitation laser in a time window of ca. 10 µs which was important

for our measuring protocol. A safeguard slit confined the excitation and activation light within the imaged field of view (FOV) of 33 µm × 33 µm inside the observation plane. Thus, fluorophores outside the FOV were protected from the laser illumination, particularly from laser induced bleaching. The centers of the Gaussian shaped laser beams are placed roughly int he middle of the FOV. After imaging we turned off all lasers and moved the specimen ca. 120 µm to a new position in which the fluorophores have not been subjected to laser illumination. Then a new counting measurement started consisting of 20000 frames and an exposure time of 15 ms and a dead time of 500 µs between two frames. Within the first ca. 25 s the camera adjusted to its background level while excitation and activation lasers were turned off. Then we started the UV laser for ca. 5 s to activate all fluorophores before we turned on the excitation laser and let both run independently. Also the excitation laser was timed to start ca. 50 µs after the EMCCD-camera began to record a new frame. Note, although we measured 20000 frames the counting estimation discards the first 1940 frames in which the camera bckground adjusted to a constant level. It also discards the last 4000 frames because they were not needed. Therefore a measured time trace consisted of 14060 frames.

4.3.2 Sample preparation

The objective slides (VWR) and the cover slips (VWR) were wiped with acetone (Morphisto) and then cleaned by a plasma cleaner (femto, diener electronic) in an oxygen environment for 30 min. To immobilize the DNA Origami structures (Gattaquant) we followed 'Imobilization in a flow chamber' [78]: BSA-Biotin (Sigma), Neutravidin (Thermo Scientific), $MgCl_2$ 12.5 mM (magnesium chloride hexahydrate, Sigma). Furthermore, for every sample exhibiting immobilized origami structures we simultaneously prepared a second sample in the same way but did not deposit any origami structures. Thus, the second sample served as a control for any impurity in the preparation process.

4.3.3 Imaging buffer

For best performance of Alexa Fluor 647 we have used a similar imaging buffer as reported in [39]. It consisted of 1M Tris-HCl ph 8.0 (Life-Technologies), glucose oxidase 0.5 mg ml^{-1} (Sigma), catalase 40 µg ml^{-1} (Sigma), glucose 10 (w/v)% (Sigma), βME 143 mM (Sigma) and $MgCl_2$ 12.5 mM (magnesium chloride hexahydrate, Sigma). The buffer was prepared just before the measurement. Tris-HCL and catalase were stored at 8 °C , glucose oxidase stored at -20 °C and the βME stored at 20 °C.

4.3.4 Background correction

We have corrected all our data for a time dependent background level B_t mainly produced by the Gaussian shaped beam profile of the excitation, see fig. 4.3.1. A region with increased background caused by a UV-reflex was discarded for both counting evaluation and background correction. The correction was performed as follows:

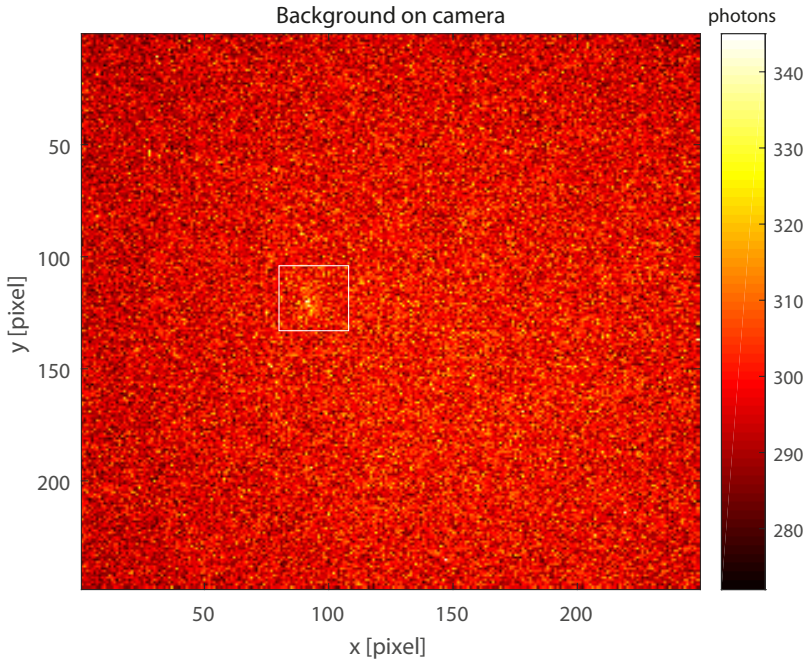

Figure 4.3.1: A measured frame showing no signal but only background caused mainly by the excitation laser. The white box includes a UV reflex. We have discarded all data within the box for background correction. Thus, we also did not use any Alexa Fluor 647 signals originating from that region.

The first frame in which the specimen was illuminated by excitation light, fig. 4.2.3, was used to identify all pixels with high signal. These identified pixels were then removed from all subsequent frames of the measurement such that only background signal remained in the data. For the remaining pixels a two dimensional polynomial of third degree

$$P_t(x,y) = a_1x^2 + a_2y^2 + a_3xy + a_4x + a_5y + a_6 \\ +a_7x^3 + a_8y^3 + a_9x^2y + a_{10}y^2x$$

was then fitted to every frame to determine a possible time varying background, see fig. 4.3.2. Thus, $P_t(x,y)$ is a global averaged approximation for all locations (x,y) in the FOV but the counting analysis was performed locally for each evaluation region of 7x7 pixel. Therefore, the background level for an evaluation region was best approximated by

$$B_t = -\sum_{i=1}^{49} P_t(x_i,y_i) - \mu,$$

where μ differs for every region but is constant over time. It was obtained by plotting the globally corrected fluorescence trace within an evaluation region $Y_t' = Y_{t,measured} - \Sigma_{i=1}^{49} P_t(x_i,y_i)$ for all t in a histogram and fitting a Gaussian $G(\mu,s^2)$, μ expectation value and s standard deviation, to the resulting distribution. An example is given in fig. 4.3.3. The distribution clearly shows a dominant noise mode and a minor signal mode which is reasonable since the plotted fluorescence trace Y_t' (inlaid picture) consists mainly from noise and a comparably small amount of fluorescence signal. Finally the background

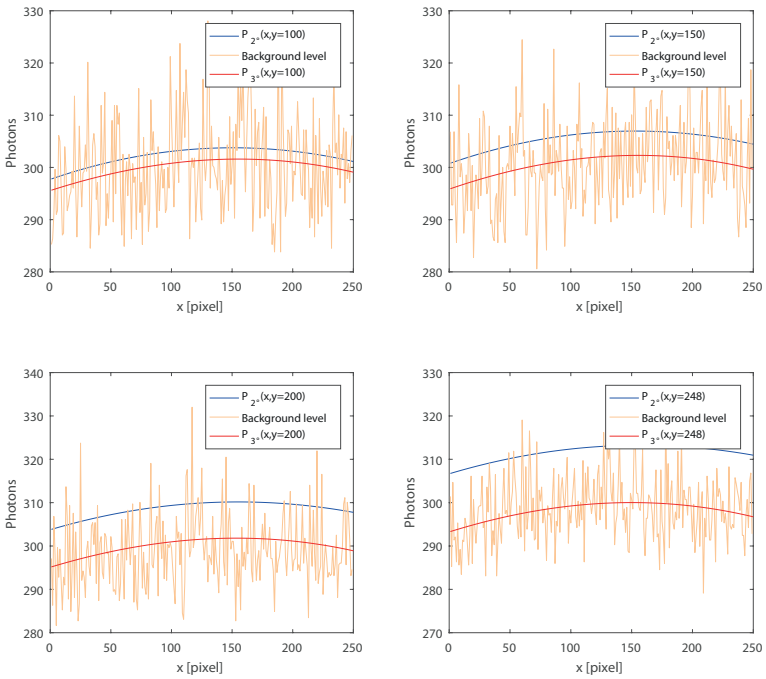

Figure 4.3.2: All graphs show fits of the background level of the camera frame shown in fig. 4.3.1 for different x-profiles in the field of view, $y = 100, 150, 200, 248$. The polynomial of third degree $P_{3^\circ}(x, y)$ describes the average background level adequate and is clearly superior to the polynomial of second degree $P_{2^\circ}(x, y)$.

corrected fluorescence within an evaluation region is given by

$$Y_t = Y_{t,measured} + B_t.$$

4.3.5 Background correction for added fluorescence traces

Although the so far presented background correction is matured for measured fluorescence traces it is not sufficient for added fluorescence traces. A background corrected trace still has a small offset because the determination of the local correction term μ has an noise stemming from the Gaussian fit of the noise mode. Therefore, by adding several source traces into an added trace the remaining offsets are added, too. We correct this offset in a similar way as before: Fitting a Gaussian $G(\mu_{add}, s^2_{add})$ to the noise mode of the added trace. But the added trace differs from its source traces: First the resulting noise mode is broader because the variances are added, too. Second this broader noise mode overlaps with the more distinct signal mode caused by the increased number of 6 or 50 fluorophores underlying the added trace fig. 4.3.4. Both effects lead to an asymmetrical photon distribution in which the noise and the signal mode are not clearly distinguishable. Therefore, the signal mode cannot be ignored in the fitting process anymore as can be seen in fig. 4.3.3. Because we are solely interested in the mean value μ_{add} of the Gaussian noise mode we exploit its symmetrical shape by fitting mainly its negative half in which no

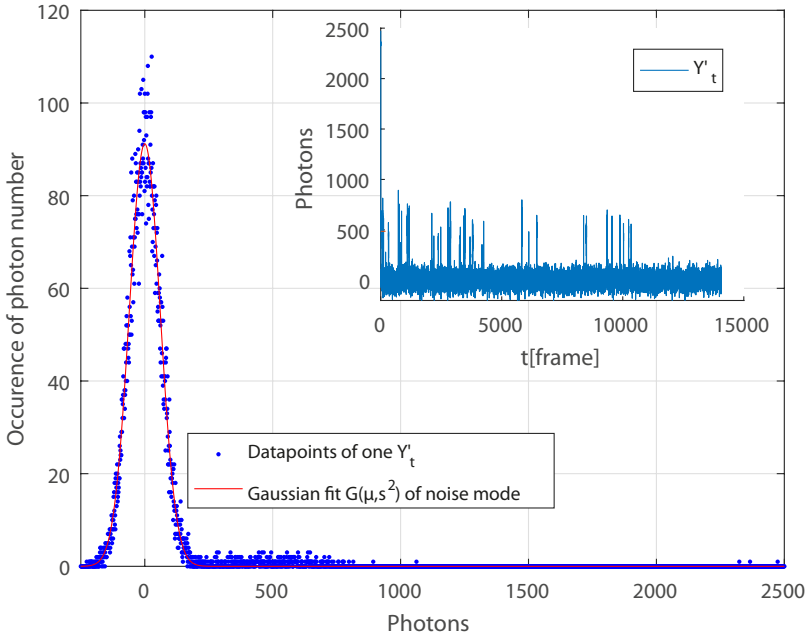

Figure 4.3.3: Histogram of the globally corrected fluorescence Y_t' within an evaluation region. We fit the noise mode with a Gaussian $G(\mu, s^2)$ to determine a local correction term μ. This is repeated for every evaluation region. Inlaid picture top right: Globally corrected time varying fluorescence Y_t' of the histogram in the outer picture.

interfering noise signal is present. In order to further increase the quality of the fit we also include all values up to a cut off value of 150 photons such that the estimation contains the peak value of the Gaussian noise mode. The cut off value is based on knowledge of the background corrected source traces Y_t which have usually a standard deviation of $s = 50$ photons. This implicates that ca. 99% of the noise contribution is found ca. in the photon interval $[-3s, 3s]$ since it is given by a Gaussian distribution $G(\mu, s^2)$. Furthermore, the noise mode is dominant on that interval for a source trace compared to the signal mode, see fig. 4.3.3. Thereby, choosing 150 photons as cut off value in the before mentioned fit of an added trace ensures we mainly fit noise. We also choose a bin size of 10 photons to average the data. The found μ_{add} in the case of 50 added single fluorophore traces are shown in fig. 4.3.4. The mean of the distribution is $1.3 \cdot 50$ photons which means that a background corrected single fluorophore trace Y_t has in average a remaining offset of 1.3 photons.

4.3.6 Determination of labeling efficiency for maximal two fluorophores for origami designs (V,VI,VII,VIII)

We tested the assumption of independent fluorophores with origami designs (V,VI,VII,VIII) which exhibit two binding positions. For this the labeling efficiencies had to be determined independently from our Markov model.

The idea is to analyze the measured brightness N of an origami structure in the first frame and explain it with the expected binomial distribution of the labeled fluorophores.

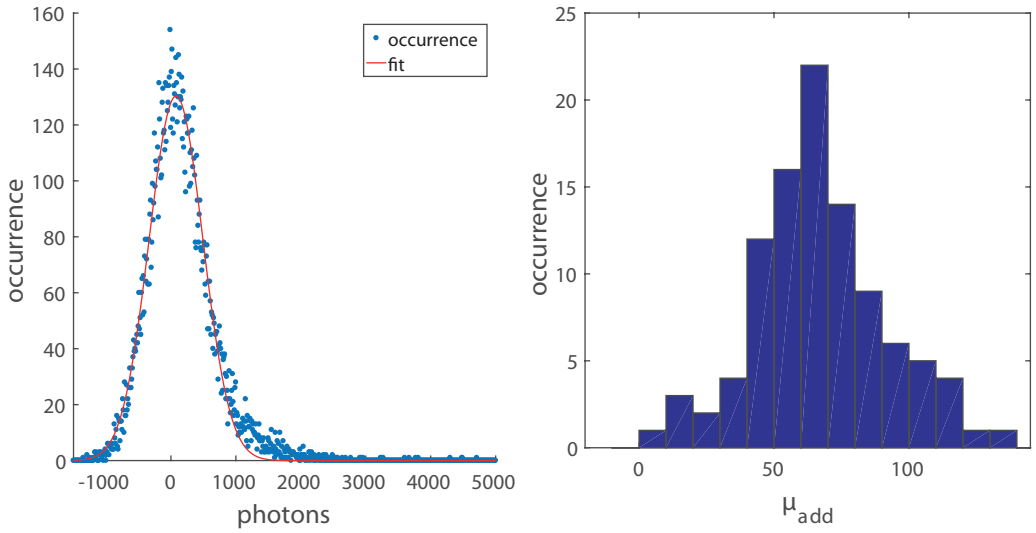

Figure 4.3.4: Left: Asymmetrical photon distribution shown for a added fluorescence trace of 50 single fluorophore traces. Because noise mode overlaps with the signal mode we restrict the Gaussian fit $G(\mu_{add}, s^2_{add})$ to the interval [-1500,..,150] at which 150 photons is roughly the $3s$ value of the noise mode $G(\mu, s^2)$ in an original trace. Below this upper limit the influence of the signal mode is negligible. Right: Histogram of all found μ_{add}. Its expectation value is $1.3 \cdot 50$ photons which means that a background corrected single fluorophore trace has in average a remaining offset of 1.3 photons.

To compare the brightness of different origami structures with each other we have to correct the measured values N for their position in the field of view of the camera since the excitation beam has a Gaussian shape. Simply confining the ROI to a small region in the FOV is not an adequate solution because it drastically reduces the available data. Although the before mentioned background correction via a polynomial function enables an estimation of the excitation beam position, it is not necessarily a good estimation of its shape because the background signal is not consequently linear to the excitation intensity. But the photon emission rate of Alexa Fluor 647 is linear to the excitation intensity [39] and therefore the measured brightness values are linear, too. Therefore, we use single fluorophore data stemming from origami design (IV) to estimate the position of the beam.

In the first step we corrected measured photon numbers N stemming from the named origami design for their position in the field of view. We determined the shape of the excitation beam by measuring the number of emitted photons N, summed over 7×7 region, (brightness) of single fluorophores in our field of view during the first frame. For this purpose we used origami design (IV) which exhibits one binding position. Hence, the measured brightness surely stems from a single fluorophore, depicted as blue dots in fig. 4.3.5, which we described by a two dimensional Gaussian distribution:

$$N_{IV}(x, y) = \frac{A}{2\pi r_x r_y} \exp -\left(\frac{(x - x_0)^2}{2r_x^2} + \frac{(y - y_0)^2}{2r_y^2}\right).$$

Here r_x, r_y are the standard deviation, x_0, y_0 the center of the excitation beam and A a fit parameter. The fit results are listed in tab. 4.3. Thereby, we correct the measured photon numbers N for

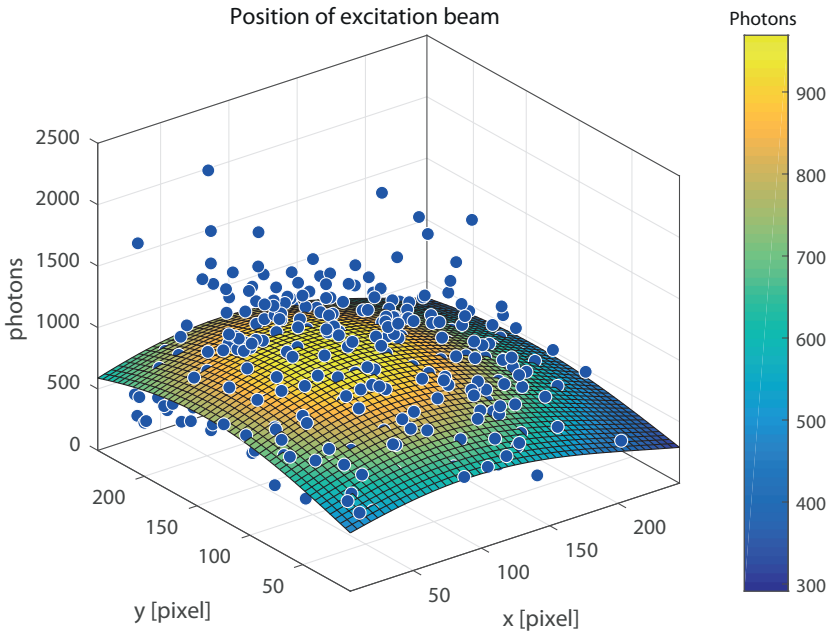

Figure 4.3.5: Depicted is the background corrected photon numbers (blue dots) in the first frame for single Alexa Fluor 647 fluorophores. We have fitted a two dimensional Gaussian (colored surface) over its position in the camera field of view which approximates the Gaussian shaped excitation illumination.

parameter	value	95% confidence band
A[photons $\cdot$ pixel^2]	$1.1 \cdot 10^8$	$(9 \cdot 10^7, 1.3 \cdot 10^8)$
r_x[pixel]	126	(107, 145)
r_y[pixel]	142	(118,166)
x_0[pixel]	92	(82,103)
y_0[pixel]	143	(132,154)

Table 4.3: Determination of excitation beam position.

their detected position x', y' within the field of view by

$$N_c = N \cdot \frac{N_{IV}(x_0, y_0)}{N_{IV}(x', y')} = N \cdot \kappa.$$

Because the position of the excitation beam did not change for measurements of origami designs (V,VI,VII,VIII) we have corrected the measured photon numbers in the same way. To minimize possible deviations from a Gaussian shaped excitation we narrowed the region of considered origami structures to the center of the Gaussian by demanding $\kappa \leq 1.25$. The corrected photon numbers, stemming from the first frame, were plotted for each design in a histogram, see fig. 4.3.6. We then fitted each histogram by a binomially weighted sum of two Normal distributions assuming a constant labeling probability p for both binding

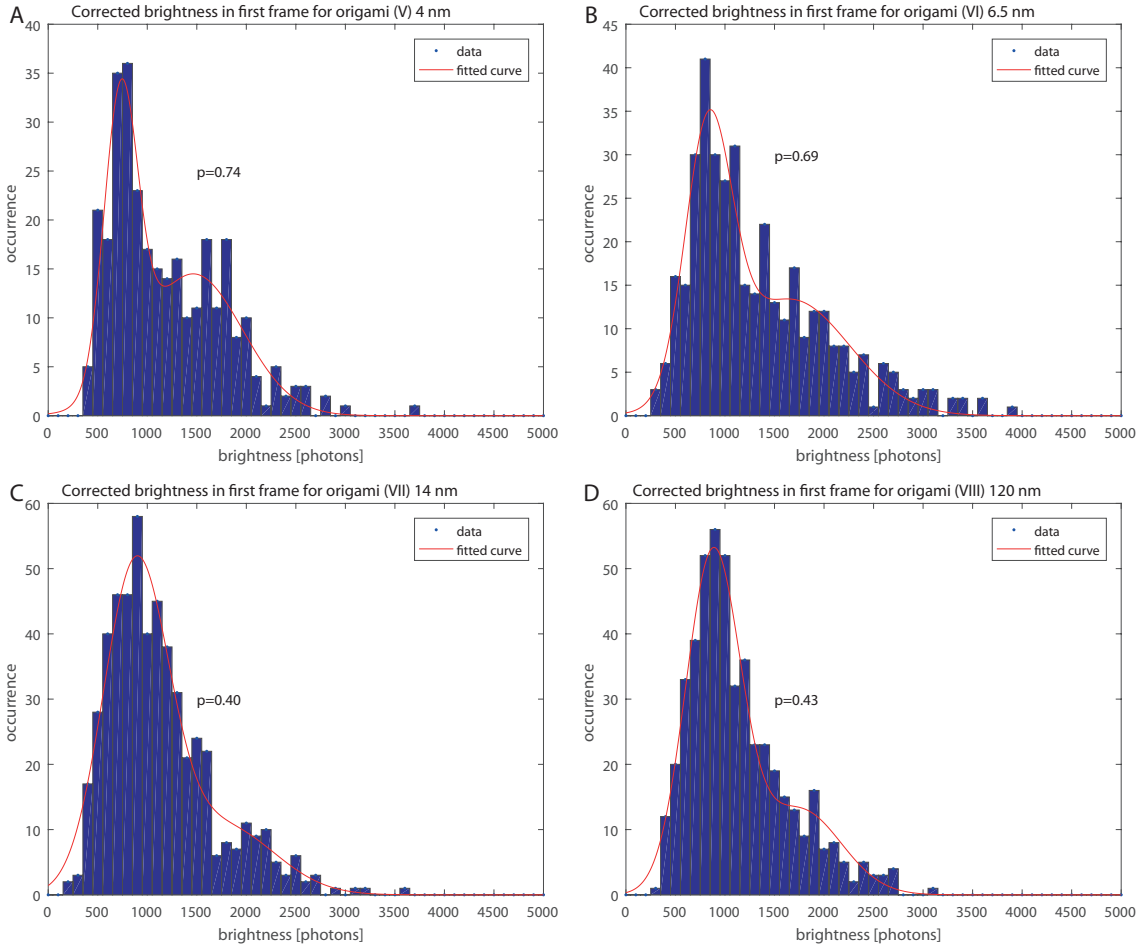

Figure 4.3.6: Plotted are the histograms H_{N_c} of the corrected photon numbers from the first image after activation of the excitation laser for origami designs (V), (VI), (VII), (VIII) in A, B, C, D, respectively. Hence we fitted the sum of two binomial weighed Normal distributions of which the former one resembles all origami structures carrying just one fluorophor and the latter one two fluorophores. Their proportion is linked to the labeling efficiency p, which we have determined by the fit.

positions on the origami design

$$\begin{aligned} H_{N_c}(x) &= A \cdot \Big(\mathrm{Bin}(X=1|p,n=2) \cdot \mathcal{N}_1 + \mathrm{Bin}(X=2|p,n=2) \cdot \mathcal{N}_2 \Big) \\ &= A \cdot \Big(\frac{2p(1-p)}{\sqrt{2\pi c_1^2}} \exp - \frac{(x-\mu_1)^2}{2c_1^2} + \frac{p^2}{\sqrt{2\pi c_2^2}} \exp - \frac{(x-2\mu_1)^2}{2c_2^2} \Big). \end{aligned}$$

Here μ_1 is the expected number of photons of one fluorophore in the first frame, c_1, c_2 the variance of the corresponding Normal distribution and A a fit parameter. Because the resulting p is part of the Markov model equations eq. 4.15 and eq. 4.16 which assume independently fluorescing fluorophores we do the same here. Hence, two fluorophores emit in average twice as much photons as one fluorophore. Therefore, we set the expectation value of the second Gaussian $\mu_2 = 2\mu_1$. The results of the fits are listed in tab. 4.4.

origami design	parameter	value	95% confidence band
(V) 4 nm	A[photons]	$3.28 \cdot 10^4$	$(3.05 \cdot 10^4, 3.51 \cdot 10^4)$
	b_1[photons]	732	(707, 757)
	c_1[photons]	170	(144,196)
	c_2[photons]	498	(394,602)
	p	0.74	(0.67,0.81)
	R^2	0.92	
(VI) 6.5 nm	A[photons]	$4.1 \cdot 10^4$	$(3.8 \cdot 10^4, 4.4 \cdot 10^5)$
	b_1[photons]	831	(797, 866)
	c_1[photons]	235	(200,269)
	c_2[photons]	594	(456,731)
	p	0.69	(0.61,0.77)
	R^2	0.93	
(VII) 14 nm	A[photons]	$8.5 \cdot 10^4$	$(6.9 \cdot 10^4, 3.51 \cdot 10^5)$
	b_1[photons]	883	(849, 916)
	c_1[photons]	330	(301,359)
	c_2[photons]	523	(325,721)
	p	0.40	(0.29,0.51)
	R^2	0.96	
(VIII) 120 nm	A[photons]	$7.3 \cdot 10^4$	$(6.3 \cdot 10^4, 8.3 \cdot 10^5)$
	b_1[photons]	878	(851, 904)
	c_1[photons]	276	(256,296)
	c_2[photons]	418	(292,544)
	p	0.43	(0.34,0.52)
	R^2	0.97	

Table 4.4: Fitparameter results of labeling efficiency determination.

4.3.7 EMCCD camera

For our counting analysis we worked on photon numbers which we calculated from the measured digital values C from the EMCCD camera. The following is based on [53, 77].

An EMCCD camera consists of an array detector, a readout register, a multiplication register and an electrons to voltage converter. Inside the array detector photons generate photoelectrons which are transferred into the readout register. For better noise performance the charges are then multiplied within the multiplication register before they are converted into voltage. This process has several noise sources: Thermal electrons also known as dark current S_{dark}. For cooling temperatures of ca. -100 °C and small exposure times this source is negligible. The voltage conversion process introduces a readout noise. For CCD-cameras this is the limiting noise. Thus, the total variance on the camera output is given by

$$\sigma_{tot}^2 = A^2(\sigma_{signal}^2 + \sigma_{dark}^2 + \sigma_{read}^2)$$

where σ_{signal} is the noise of the signal S. A is the total video chain gain which includes the on-chip to voltage conversion factor. An EMCCD has a better noise performance than a conventional CCD because the electron multiplication register renders the readout noise negligible. Multiplication is executed by impact ionisation when transferring the charges to the next element of the register. If the probability to generate an additional electron is 1.5% 600 elements have a total gain of $M = g^N = (1.015)^{600} \approx 7500$. Unfortunately, the multiplication process introduces new noise called excess noise which is accounted for by the excess noise factor f. The factor is defined through

$$f^2 = \frac{\sigma_{out}^2}{\sigma_{in}^2}$$

where σ_{in} is the noise before the multiplication process and σ_{out} after it. Therefore, an ideal EMCCD would have an excess noise factor of 1. Note, that the excess noise factor $f(E)$ depends on the number of multiplication elements which are set by the typically user-selectable EMGain = E. The function $f(E)$ is known [53] and quickly approaches $f = \sqrt{(2)}$ for $E > 10$. Using $S = \sigma_{signal}^2$, $S_{dark} = \sigma_{dark}^2$ and the definition of f the total noise of an EMCCD can be written as

$$\sigma_{tot}^2 = f^2 A^2 M^2 (S + S_{dark}) + A^2 \sigma_{read}^2 \tag{4.17}$$

$$= f^2 AM S_{out} + A^2 \sigma_{read}^2 \tag{4.18}$$

This equation is useful for determining the searched relation between digital counts C and the signal S. Strictly speaking, S is the number of detected photons, not the number of photons falling on the detector since the camera has not a quantum efficiency of 1. For our application we do not need to know the exact photon numbers of the signal [31], thus we write

$$C = AM \cdot S.$$

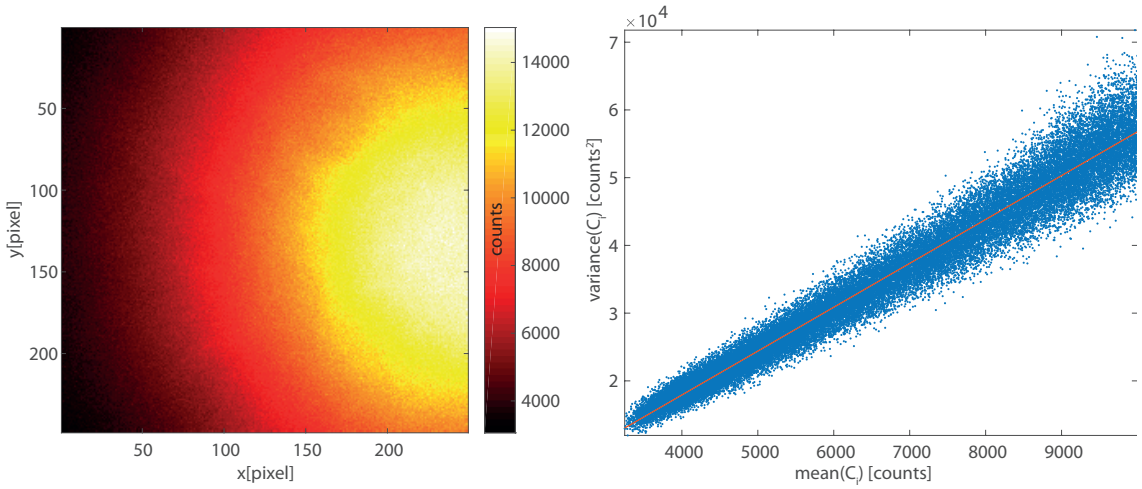

Figure 4.3.7: Photon counts relation. Left: A 532 nm laser excites a thick fluid Rhodamine B layer whose fluorescence is detected by an EMCCD-camera with an EMGain of 40. Shown is the first of 500 imaged frames. For each pixel $j \in [1; ..; 249\text{x}248]$ the detected fluorescence stems from a constant excitation intensity during the 500 frames. Right: To convert measured digital values C into detected photon numbers S we use the known linear relation between the detected variance and the signal S. Therefore, we calculate the variance and the mean for each pixel and execute a linear regression whose slope delivers the conversion factor.

In order to determine AM we have illuminated a specimen exhibiting a thick fluid layer of Rhodamine B with 532 nm light and imaged 500 frames for constant EMGain, see fig. 4.3.7.

In the dye solution bleached fluorophores in the FOV were continously replaced by unbleached fluorophores from outside the FOV. This ensured that bleaching induced signal decrease was minimized during the measurement. Although the local excitation intensity in each pixel is constant over the course of the observation, the measured digital count values C_i, $i \in [1; ..; 500]$, are not caused by the named noise sources. Therefore, we calculate the mean(C_i) and a corresponding variance $\text{Var}(C_i) = \sigma_{tot}^2$. Their relation is described by eq. 4.18 in which $S_{out} = \text{mean}(C_i)$, see fig. 4.3.7. Furthermore, the camera images the Gaussian shaped profile of the laser on 512 × 512 pixels such that many different values of S_{out} were available. A linear fit delivered fAM as slope b. Because $f(E)$ is known we have subsequently calculated the searched factor AM.

$$AM = \frac{b}{f^2} = \frac{b}{u}$$

$$\Delta(AM) = \sqrt{\left(\frac{\Delta b}{u}\right)^2 + \left(\frac{b \cdot \Delta u}{u^2}\right)^2}$$

This process was then executed two times for each of the 17 different EMGain values to characterize our camera, see tab. 4.5 and fig. 4.3.8. We found that eq. 4.18 is not true within the whole dynamic 14 bit range of our EMCCD-camera, $C \in [0; ...; 2^{14}]$ fig. 4.3.8. Deviations can occur for $C > 8000$ counts at which the exact value depends on the chosen EMGain. Therefore, we restricted the fit region and did not operate our camera in that non-linear dynamic range during our measurements as a non linear behavior of the camera

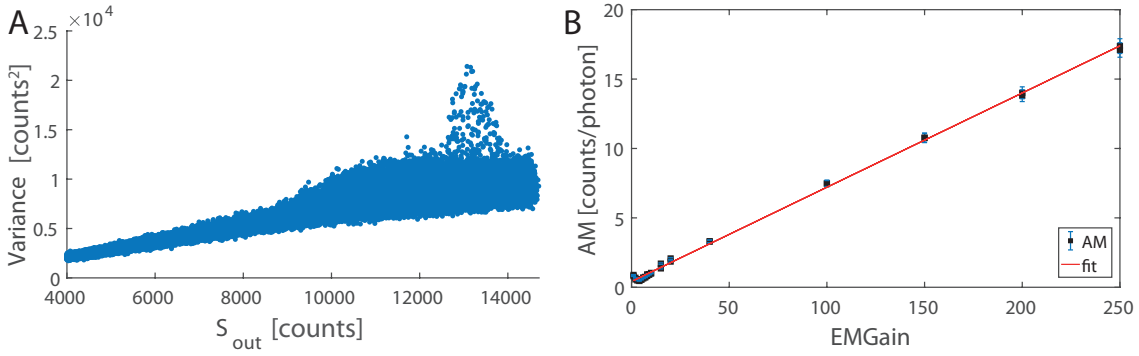

Figure 4.3.8: Left: Nonlinear dynamic range. The measured total variance σ^2_{tot} of the EMCCD camera is not linear to the output signal S_{out} over the whole dynamic range of 14 bit. We have not operated the camera in that non linear range in our measurements because it would result in a nonlinear relation between molecule number and detected photons otherwise. Right: Conversion factor AM. We found the expected linear relation between EMGain and conversion factor AM for our EMCCD-camera. The fitted function allows to convert digitial count numbers to photon numbers for arbitrarily chosen EMGain.

would result in wrong molecule numbers.

Furthermore, the excess noise has impact on the excess variance parameter θ_3 of our Markov model. Since θ_3 is derived from a detected fluorescence trace and depends on the variance $\mathrm{Var}(Y)$ and expectation value $\mathbb{E}(Y)$ of the number of emitted photons per frame, the conversion process from detected photons to output signal has to be considered. Due to the limited solid angle of the objective lens we do not detect all emitted photons. In addition the camera sensor detects a subfraction of the incoming photons described by its limited quantum efficiency. As stated in section 4.1.2 these effects are negligible for our counting Markov model. However, the multiplication effect in the EMGain register of the EMCCD-camera introduces additional noise according to eq. 4.17. This effect is incorporated in our model equation eq. 4.10 and it has to be accounted for if θ_3 is determined from the output signal S_{out} of an EMCC-camera [31]:

$$\begin{aligned} \mathbb{E}(Y) &= \mathbb{E}(S_{out}) \\ \theta_3^{S_{out}} &= \frac{\mathrm{Var}(S_{out})}{\mathbb{E}(S_{out})} - \frac{1}{\mathbb{E}(S_{out})} = \frac{f^2-1}{\mathbb{E}(Y)} + \theta_3 \end{aligned}$$

Since $\mathbb{E}(Y)$ is several hundreds of photons for Alexa Fluor 647 the approximation $\theta_3 \approx \theta_3^{S_{out}}$ is valid in our measurements. Note, θ_3 and $\theta_3^{S_{out}}$ are dimensionless due to the chracteristics of the Poisson distribution.

4.3.8 Origami designs and data processing

This section gives an overview of the examined origami designs, the corresponding performed experiments and the necessary data processing.

The first step in data processing was to choose the evaluated area on the camera. Its field of view (FOV) , 250 x 250 pixel, is depicted in fig. 4.2.3 which was limited by a rectangle slit in an intermediate plane of the microscope. Because we wanted to evaluate origami structures with a roughly constant excitation intensity we chose an area centered

EMGain	$b = f^2AM$	Δb	S_{max}	f^2	$\Delta(f^2)$	$AM = \frac{b}{f^2}\ \frac{\text{Counts}}{\text{Photon}}$	$\Delta(AM)$
1	0,88978	0,00288	8000	1	0,03	0,889	0,026
2	1,01644	0,00371	10000	1,48	0,05	0,686	0,023
3	0,80733	0,00183	10000	1,65	0,05	0,489	0,014
4	0,78458	0,00216	8000	1,73	0,04	0,453	0,010
5	1,02528	0,00248	10000	1,78	0,04	0,576	0,013
6	1,27882	0,00338	10000	1,81	0,04	0,706	0,015
7	1,37507	0,00365	10000	1,83	0,04	0,751	0,016
8	1,5055	0,00356	10000	1,85	0,04	0,813	0,017
9	1,76328	0,00611	10000	1,86	0,04	0,948	0,020
10	1,84703	0,00641	10000	1,87	0,04	0,987	0,021
15	2,59569	0,00684	10000	1,91	0,06	1,359	0,042
20	3,5536	0,01274	10000	1,92	0,06	1,850	0,058
40	6,46495	0,01031	12000	1,95	0,06	3,315	0,102
100	14,61538	0,02179	12000	1,96	0,06	7,456	0,228
150	21,14067	0,02662	16384	1,96	0,06	10,786	0,330
200	27,05295	0,03384	16384	1,96	0,06	13,802	0,422
250	34,0558	0,04177	16384	1,96	0,06	17,375	0,532
1	0,80052	0,00275	8000	1	0,03	0,800	0,024
2	0,83681	0,00277	10000	1,48	0,05	0,565	0,019
3	0,92851	0,00304	10000	1,65	0,05	0,562	0,017
4	0,87851	0,00336	8000	1,73	0,04	0,507	0,011
5	0,96707	0,00219	10000	1,78	0,04	0,543	0,012
6	1,14901	0,00254	10000	1,81	0,04	0,634	0,014
7	1,29171	0,00264	10000	1,83	0,04	0,705	0,015
8	1,71925	0,00598	10000	1,85	0,04	0,929	0,020
9	1,6815	0,00371	10000	1,86	0,04	0,904	0,019
10	1,9374	0,00489	10000	1,87	0,04	1,036	0,022
15	3,2581	0,00735	10000	1,91	0,06	1,705	0,053
20	3,98927	0,00791	10000	1,92	0,06	2,077	0,065
40	6,41696	0,01002	12000	1,95	0,06	3,290	0,101
100	14,69056	0,02195	12000	1,96	0,06	7,495	0,229
150	21,0721	0,02665	16384	1,96	0,06	10,751	0,329
200	27,46216	0,034	16384	1,96	0,06	14,0117	0,429
250	33,51045	0,0407	16384	1,96	0,06	17,097	0,523

Table 4.5: Determination of photon count conversion AM

at the maximum intensity of the excitation profile. Then we chose the borders of the are such that the excitation intensity was $> 80\%$ of its peak value. For origami designs (I,II,III) this area is a circle with radius 80 pixel. For origami designs (IV,V,VI,VII,VIII) the area was slightly elliptical. We took these different approaches because for the latter the estimation of the beam profile is more trustworthy but not transferable to the first, see section 4.3.6- Furthermore, these approaches excluded possible fringe effects.

The second step was to identify origami structures within the evaluation area. Since the signal to noise ratio was at least five for the fluorescence signal of a single fluorophore compared to the background noise we identified origami structures as bright spots in our first frame. We could exclude dirt as signal origin due to the preparation protocol of our specimen.

The third step was to define regions of 7 $\times$7 pixel for each identified origami structure. If these regions did not overlap each other they were evaluation regions for our Markov model. Each evaluation region then defined a corresponding unique fluorescence trace $Y_{t,measured}$.

The fourth step was to globally correct all $Y_{t,measured}$ for the background noise, decribed in section 4.3.4, given by a third degree polynomial. Then we independently corrected the different fluorescence traces again for a remaining background offset. The background were not fully compensated by the global background correction because the polynomial is a fit over the whole FOV of 250 x 250 pixel and had a varying difference to the real background within the different evaluation regions of 7 x 7 pixel. After this process we received the fully background corrected fluorescence traces Y_t of single origami structures. Note, in the evaluations of added fluorescence functions we had to repeat the last step because a small offset remained within each Y_t.

origami design	n_b[nm]	d_b[nm]	d_q[nm]
(I)	6	14	120
(II)	4	28	120
(III)	22	unknown	120
(IV)	1		
(V)	2	120	120
(VI)	2	120	120
(VII)	2	120	120
(VIII)	2	120	120

Table 4.6: origami designs. n_b denotes the number of binding positions, d_b the minimum distance between two binding spots, d_q the distance between the two quotas.

Chapter 5

Discussion

In the context of this thesis, experiments were developed and performed to verify and improve statistical methods for the qualitative and quantitative analysis of SMS microscopy data. The part related to qualitative analysis presented a new method for drift correction which is solely based on the drift-compromised SMS data and does not need additional marking structures. In contrast to a previous correction method which also works on compromised SMS data but is based on cross correlations, the method presented here can additionally correct for rotational drift and scaling, whereby all three disturbances may occur simultaneously. In order to prove the feasibility of the new correction method, we performed a test on SMS data which were compromised in a controlled way and compared the results with those obtained by common fiducial marker tracking correction. We distinguished between two cases. In the first case, the data stem from measurements in which the sample was moved in the lateral direction during image acquisition. Here, our drift correction performed at least as good as conventional fiducial marker tracking. In addition, we were also able to determine the uncertainty of our drift estimation by using a bootstrapping approach. This uncertainty could be readily visualized by blurring the drift-corrected image with the difference with respect to all possible drift functions which fall within a confidence interval of 0.95. Therefore, this blurred image covers the true structure with a probability of 0.95. To date, no other drift correction method has been able to provide such a quality seal. In the second case of controlled data degradation, the sample has been rotated during image acquisition. However, mechanical instabilities of the rotation stage caused the controlled rotation to be superimposed with a random translation and thus a movement of the rotation axis. Hence, common fiducial marker tracking was not able to reconstruct the high-resolution image. We have therefore initially extended this method in such a way that rotations are also taken into account (extended fiducial reconstruction). However, we needed to use a priori information about the movement, which is normally not available. Consequently, the corrected image is not a benchmark for our drift estimation and mainly serves as ground truth. Our SMS data based correction performed satisfactorily and did not quite reach the quality of the extended fiducial reconstruction. This is mainly due to the fact that it assumes a fixed pivotal point, which was not the case for the experiments. Therefore, it can be expected that the quality of the

results can be significantly improved if a movement of the pivotal point is included in the statistical model in the future. However, it is remarkable that the data based correction produced distinct high-resolution images, even if only a fraction of the available data was used for drift determination. This is fundamentally different to fiducial marker tracking, which delivers very quickly false results when too much of the bead data is discarded. Perspectively, the bootstraping based quality seal must be incorporated in the correction for rotation and scaling. These results are an important step towards the determination of local movements in living cells using SMS microscopy. Reaching this goal seems possible, because the localized molecules originate from the density distribution of the overall population which one should be able to determine. However, this requires modification of our model, as it currently only describes global drift.

In the part related to quantitative SMS microscopy, we followed an entirely new approach to determine molecule numbers in GSDIM/PALM/STORM microscopy. In contrast to previous studies which evaluate blinking events, we have developed a complete statistical model of the imaging process. This model is based on a discrete-time Markov chain to derive a statement about expected time dependent photon numbers and the corresponding covariance. Furthermore, we integrated influences stemming from the imaging process, e.g. the excess noise of an EMCCD camera.

Since our evaluation is based on the analysis of time dependent fluorescence traces, it is insensitive against errors which, for example, are based on the non-recognition or incorrect allocation of blinking events. Our model evaluates the frequency of the bright state occupation in conjunction with the number of detected photons. It is even not necessary to detect each transition into or from the bright state. This characteristic is best illustrated by the fact that we evaluate only a fraction of 4000 frames from a trace which contains in total 16040 frames. This proceeding is motivated by saving computation time. By bringing the fluorophores into a well-defined initial state by means of an optimized recording protocol it was possible to simplify the data evaluation even further, as fewer parameters had to be determined.

Since our method is not based on the identification of blinking events, it is unproblematic if several molecules are simultaneously in the bright state within a diffraction-limited range. This is contrary to e.g. a previously published Markov model [28] or bleaching based counting [25] where exactly this issue represents a limitation. Contrary, our model is capable to count both - low and high numbers of molecules. This has been exemplified by a single fluorophore study of Alexa Fluor 647. In that study the model successfully analyzed added fluorophore traces from single molecules and estimated the underlying low and high molecule numbers correctly. These results were impressive because the signal-to-noise ratio of such added traces is much worse as compared to single traces recorded from several molecules. Therefore, it is justified to assume that molecule estimations will perform even better for real data and that a much larger number of molecules than tested in this study can be reliably counted. The single molecule traces were also used for the verification of our model equations. For this purpose we averaged the traces, thereby

receiving an empirical variance. By comparing the empirical variance with its model prediction we found them in excellent agreement. An important characteristic of both tests is the large distance of > 200 nm between the individual fluorophores. Therefore, we could be sure that the fluorophores were mutually independent, which is a basic assumption of our Markov model.

After model verification we analyzed an origami design exhibiting inter molecule distances smaller than 14 nm and in total 22 binding spots. Assuming an identical labeling efficiency p for each spot the expected counting result should resemble a conditioned binomial distribution. Unfortunately, this was not the case. As an explanation we proposed the hypothesis that the model condition of mutual independence of the fluorophores was violated due to the small inter molecule distances. To test this hypothesis we analyzed origami designs exhibiting two binding spots with distances of 4 nm, 6.5 nm, 14 nm and 120 nm. Similar to the model verification study, we averaged the fluorescence traces of a specific design and determined an empirical variance. The empirical variance was then subsequently compared with its model based prediction. Here we also had to take into account that the analyzed origami structures carried either one or two fluorophores. Therefore, we incorporated the, independently determined, labeling efficiency p into the model equations. We found excellent agreements between model and empirical data for binding spot distances of 14 nm and 120 nm. However, for distances of 4 nm and 6.5 nm the empirical variance was considerably higher than the predicted one for the first ca. 20 frames of the measurement. This is particularly interesting because in the beginning of the experiment the probability to find both fluorophores in the bright state is highest, as the experiment has been designed such that all Alexa Fluor 647 molecules start in the bright state. These results therefore strongly support our hypothesis of interacting fluorophores for small inter molecule distances. An analysis of the underlying photophysical mechanism was not subject of this work. However, since effects like self-quenching have been observed in a wide range of fluorescent dyes [81] and Alexa 647 is known to exhibit only limited quenching characteristics [82], we conclude that the observed effect should also occur with other dyes, especially at the high labeling densities required for super-resolution microscopy [83]. Therefore, we consider a respective analysis to be mandatory when molecule numbers are determined.

Based on this result we performed counting experiments for inter molecule distances larger or equal to 14 nm. Therefore, we analyzed origami designs exhibiting inter binding spot distances of 14 nm and 28 nm. The former one exhibited overall six binding spots and the latter four. For these inter molecule distances we found that our counting results were well described by a conditioned binomial distribution. Due to the origami architecture, it was not possible to attach more than a maximum of six fluorophores to the structure at sufficiently large distance. Nevertheless, our single molecule results indicate that reliable counting can also be expected for a larger number of molecules.

In a nutshell our model assumes mutual independence of the molecules. As long as this assumption is fulfilled (unbiased counting) it provides excellent results for both, small

and high numbers of molecules. As soon as the assumption of mutual independence is not valid, our model leads to incorrect results (biased counting). This is most likely also the case for any other method known from the literature, as these are implicitly based on the same assumption. Nevertheless, our model provides, to our knowledge for the first time, the possibility to detect this interference directly on basis of the measured data. By analyzing the variance between recordings of identical objects, it can be verified whether this quantity is correctly reproduced by the model. Thereby, the consistency of the corresponding molecule estimations is verified.

We also developed a simplified estimator which approximates the model results for unbiased counting. It just requires knowledge of the initial photon numbers in the first frame (brightness) and the average number of emitted photons during a burst conditioned the fluorophore occupied the bright state at the beginning of the frame. Although this estimator is computationally inexpensive it lacks the ability to verify the consistency of the results. However, it can probably be used in the future as an indicator of unbiased counting since the study on the influence of the molecular distance on the counting result has shown that the results of the Markov analysis and the simplified estimator only match if the counting is correct.

The Markov model presented is extremely general and can easily be adapted to other dyes. Although the diagram of states used is photophysically motivated, it does not have to strictly represent the precise photophysics of the fluorophore. Rather, it represents a class of molecules because states with similar lifetimes can be combined into a single one. Also, molecules with the same number of states but with different transition rates can be described by the same model, since all necessary parameters are solely estimated from the experimental data. The next important step is certainly to adapt the model such that the interactions between closely spaced fluorophores is taken into account. Another possible step is to search for a dye that, like Alexa 647, starts in a bright state but shows no or weak interaction with itself. Finally, we would like to note that our Markov model can also be easily applied to other forms of fluorescence microscopy, such as widefield or confocal microscopy, as it does not depend on the analysis of single molecule blinks. Anyhow, this study is an important step towards unbiased molecule counting in superresolution microscopy and offers the possibility to verify the reliability of the results without any further experiments.

Bibliography

[1] Eugene Hecht. *Optik*. Oldenbourg Verlag München Wien, 4th printing edition, 2002.

[2] Max Born. *Principles of Optics*. Pergamon Press, 4th edition edition, 1970.

[3] R. N. Wilke, M. Priebe, M. Bartels, K. Giewekemeyer, A. Diaz, P. Karvinen, and T. Salditt. Hard x-ray imaging of bacterial cells: nano-diffraction and ptychographic reconstruction. *Opt. Express*, 20(17):19232–19254, Aug 2012.

[4] Hisako Nakano and Kunio Shinohara. X-ray-induced cell death: Apoptosis and necrosis. *Radiation Research*, 140(1):1–9, 1994.

[5] Stefan W Hell. Microscopy and its focal switch. *Nature Methods*, 6:24–32, 02 2009.

[6] Stefan W. Hell and Jan Wichmann. Breaking the diffraction resolution limit by stimulated emission: stimulated-emission-depletion fluorescence microscopy. *Optics Letters*, 19(11):780–782, Jun 1994.

[7] T. A. Klar, S. Jakobs, M. Dyba, A. Egner, and S. W. Hell. Fluorescence microscopy with diffraction resolution barrier broken by stimulated emission. *Proceedings of the National Academy of Sciences of the United States of America*, 97(15):8206–8210, 2000.

[8] S. W. Hell and M. Kroug. Ground-state-depletion fluorscence microscopy: A concept for breaking the diffraction resolution limit. *Applied Physics B Lasers and Optics*, 60(5):495–497, May 1995.

[9] Stefan W. Hell. Toward fluorescence nanoscopy. *Nature Biotechnology*, 21(5):1347, October 2003.

[10] M. Hofmann, C. Eggeling, S. Jakobs, and S. W. Hell. Breaking the diffraction barrier in fluorescence microscopy at low light intensities by using reversibly photoswitchable proteins. *Proceedings of the National Academy of Sciences of the United States of America*, 102(49):17565–17569, 2005.

[11] Stefan W. Hell, Marcus Dyba, and Stefan Jakobs. Concepts for nanoscale resolution in fluorescence microscopy. *Current Opinion in Neurobiology*, 14(5):599 – 609, 2004.

[12] Stefan W. Hell. Strategy for far-field optical imaging and writing without diffraction limit. *Physics Letters A*, 326(1):140 – 145, 2004.

[13] Mats G. L. Gustafsson. Nonlinear structured-illumination microscopy: Wide-field fluorescence imaging with theoretically unlimited resolution. *Proceedings of the National Academy of Sciences of the United States of America*, 102(37):13081–13086, 2005.

[14] Rainer Heintzmann, Thomas M. Jovin, and Christoph Cremer. Saturated patterned excitation microscopy—a concept for optical resolution improvement. *Journal of the Optical Society of America A*, 19(8):1599–1609, Aug 2002.

[15] Michael J. Rust, Mark Bates, and Xiaowei Zhuang. Sub-diffraction-limit imaging by stochastic optical reconstruction microscopy (STORM). *Nature Methods*, 3(10):793–796, 2006.

[16] Mike Heilemann, Sebastian van de Linde, Mark Schüttpelz, Robert Kasper, Britta Seefeldt, Anindita Mukherjee, Philip Tinnefeld, and Markus Sauer. Subdiffraction-resolution fluorescence imaging with conventional fluorescent probes. *Angewandte Chemie International Edition*, 47(33):6172–6176, 2008.

[17] Jonas Fölling, Mariano Bossi, Hannes Bock, Rebecca Medda, Christian A. Wurm, Birka Hein, Stefan Jakobs, Christian Eggeling, and Stefan W. Hell. Fluorescence nanoscopy by ground-state depletion and single-molecule return. *Nature Methods*, 5:943–945, 2008.

[18] E. Betzig, G. H. Patterson, R. Sougrat, O. W. Lindwasser, S. Olenych, J. S. Bonifacino, M. W. Davidson, J. Lippincott-Schwartz, and H. F. Hess. Imaging intracellular fluorescent proteins at nanometer resolution. *Science*, 331(5793):1642–1645, 2013.

[19] Alexander Egner, Claudia Geisler, Claas von Middendorff, Hannes Bock, Dirk Wenzel, Rebecca Medda, Martin Andresen, Andre C. Stiel, Stefan Jakobs, Christian Eggeling, Andreas Schönle, and Stefan W. Hell. Fluorescence nanoscopy in whole cells by asynchronous localization of photoswitching emitters. *Biophysical Journal*, 93(9):3285–3290, 2007.

[20] Samuel T. Hess, Thanu P. K. Girirajan, and Michael D. Mason. Ultra-high resolution imaging by fluorescence photoactivation localization microscopy. *Biophysical Journal*, 91(11):4258 – 4272, 2006.

[21] Claudia Geisler, Thomas Hotz, Andreas Schönle, Stefan W. Hell, Axel Munk, and Alexander Egner. Drift estimation for single marker switching based imaging schemes. *Optics Express*, 20(7):7274–7289, Mar 2012.

[22] Alexander Hartmann, Stephan Huckemann, Jörn Dannemann, Oskar Laitenberger, Claudia Geisler, Alexander Egner, and Axel Munk. Drift estimation in sparse sequential dynamic imaging, with application to nanoscale fluorescence microscopy. *Journal of the Royal Statistical Society: Series B (Statistical Methodology)*, 78(3):563–587, 2015.

[23] Alexander Hartmann. *Estimating rigid motion in sparse sequential dynamic imaging: with applicaction to nanoscale fluorescence microscopy.* PhD thesis, Georg-August-Universität-Göttingen, 2016.

[24] Haisen Ta, Jan Keller, Markus Haltmeier, Sinem K. Saka, Jürgen Schmied, Felipe Opazo, Philip Tinnefeld, Axel Munk, and Stefan W. Hell. Mapping molecules in scanning far-field fluorescence nanoscopy. *Nature Communications*, 6(7977), 2015.

[25] Konstantinos Tsekouras, Thomas C. Custer, Hossein Jashnsaz, Nils G. Walter, and Steve Pressé. A novel method to accurately locate and count large numbers of steps by photobleaching. *Molecular Biology of the Cell*, 27(22):3601–3615, 2016.

[26] Valerie C. Coffman and Jian-Qiu Wu. Counting protein molecules using quantitative fluorescence microscopy. *Trends in Biochemical Sciences*, 37(11):499–506, 2012.

[27] S.-H. Lee, J. Y. Shin, A. Lee, and C. Bustamante. Counting single photoactivatable fluorescent molecules by photoactivated localization microscopy (PALM). *Proceedings of the National Academy of Sciences of the United States of America*, 109(43):17436–17441, 2012.

[28] Geoffrey C. Rollins, Jae Yen Shin, Carlos Bustamante, and Steve Pressé. Stochastic approach to the molecular counting problem in superresolution microscopy. *Proceedings of the National Academy of Sciences of the United States of America*, 112(2):E110–E118, 2014.

[29] Christos Karathanasis, Franziska Fricke, Gerhard Hummer, and Mike Heilemann. Molecule counts in localization microscopy with organic fluorophores. *ChemPhysChem*, 18(8):942–948, 2017.

[30] Gerhard Hummer, Franziska Fricke, and Mike Heilemann. Model-independent counting of molecules in single-molecule localization microscopy. *Molecular Biology of the Cell*, 27(22):3637–3644, 2016.

[31] T. Aspelmeier, A. Egner, C. Geisler, O. Laitenberger, and A. Munk. Counting molecues in single marker switching microscopy (in preparation). Technical Report x, 2018.

[32] Lukas Novotny. *Principles of Nano-Optics.* Cambridge University Press, 32 Avenue of the Americas, New York, NY 10013-2473, USA, 4th printing edition, 2012.

[33] C. J. R. Sheppard and T. Wilson. The image of a single point in microscopes of large numerical aperture. *Proceedings of the Royal Society of London A: Mathematical, Physical and Engineering Sciences*, 379(1776):145–158, 1982.

[34] Jörg Enderlein. Theoretical study of detection of a dipole emitter through an objective with high numerical aperture. *Optics Letters*, 25(9):634–636, May 2000.

[35] Wolfgang Demtröder. *Experimentalphysik 2.* Springer-Verlag Berlin Heidelberg New York, 3th printing edition, 2004.

[36] Daniel Aquino Maier. *Single Marker Switching Nanoscopy with 4Pi Detection: Superior Nanometric 3D Resolution.* PhD thesis, Ruperto-Carola University of Heidelberg, Germany, 2011.

[37] Phil Holzmeister, Andreas Gietl, and Philip Tinnefeld. Geminate recombination as a photoprotection mechanism for fluorescent dyes. *Angewandte Chemie International Edition*, 53(22):5685–5688, 2014.

[38] Sebastian van de Linde, Ivan Krstić, Thomas Prisner, Sören Doose, Mike Heilemann, and Markus Sauer. Photoinduced formation of reversible dye radicals and their impact on super-resolution imaging. *Photochemical & Photobiological Sciences*, 10:499–506, 2011.

[39] Graham T. Dempsey, Joshua C. Vaughan, Kok Hao Chen, Mark Bates, and Xiaowei Zhuang. Evaluation of fluorophores for optimal performance in localization-based super-resolution imaging. *Nature Methods*, 8(12):1027–1036, 2011.

[40] B. Pawley. *Handbook of biological confocal microscopy.* Springer, 3rd edition edition, 2002.

[41] Claudia Geisler. *Fluorescence nanoscopy in three dimensions.* PhD thesis, Mathematisch-Naturwissenschaftlichen Fakultäten der Georg-August-Universit¨at zu Göttingen, 2009.

[42] C. Eggeling, J. Widengren, R. Rigler, and C. A. M. Seidel. Photobleaching of fluorescent dyes under conditions used for single-molecule detection: Evidence of two-step photolysis. *Analytical Chemistry*, 70(13):2651–2659, 1998. PMID: 21644785.

[43] Christian Steinhauer, Carsten Forthmann, Jan Vogelsang, and Philip Tinnefeld. Superresolution microscopy on the basis of engineered dark states. *Journal of the American Chemical Society*, 130(50):16840–16841, 2008. PMID: 19053449.

[44] Benjamin Harke, Jan Keller, Chaitanya K. Ullal, Volker Westphal, Andreas Schönle, and Stefan W. Hell. Resolution scaling in STED microscopy. *Optics Express*, 16(6):4154–4162, Mar 2008.

[45] Valentin Magidson and Alexey Khodjakov. Chapter 23 - circumventing photodamage in live-cell microscopy. In Greenfield Sluder and David E. Wolf, editors, *Digital Microscopy*, volume 114 of *Methods in Cell Biology*, pages 545 – 560. Academic Press, 2013.

[46] Stefan Bretschneider, Christian Eggeling, and Stefan W. Hell. Breaking the diffraction barrier in fluorescence microscopy by optical shelving. *Physical Review Letters*, 98:218103, May 2007.

[47] Jennifer-Rose Krüger. *Tomographic STED Microscopy*. PhD thesis, Georg-August-Universität Göttingen, 2017.

[48] Norman Bobroff. Position measurement with a resolution and noise-limited instrument. *Review of Scientific Instruments*, 57(6):1152–1157, 1986.

[49] E. Betzig. Proposed method for molecular optical imaging. *Optics Letters*, 20(3):237–239, Feb 1995.

[50] A. Sharonov and R. M. Hochstrasser. Wide-field subdiffraction imaging by accumulated binding of diffusing probes. *Proceedings of the National Academy of Sciences of the United States of America*, 103(50):18911–18916, 2006.

[51] Russell E. Thompson, Daniel R. Larson, and Watt W. Webb. Precise nanometer localization analysis for individual fluorescent probes. *Biophysical Journal*, 82(5):2775–2783, 2002.

[52] Claas von von Middendorff. *Experimental Stochastics in High-Resolution Fluorescence Microscopy*. PhD thesis, Heidelberg, 2008.

[53] M. S. Robbins and B. J. Hadwen. The noise performance of electron multiplying charge-coupled devices. *IEEE Transactions on Electron Devices*, 50(5):1227–1232, may 2003.

[54] David Baddeley, Mark B. Cannell, and Christian Soeller. Visualization of localization microscopy data. *Microscopy and Microanalysis*, 16(1):64–72, 2010.

[55] Ben N. G. Giepmans. The fluorescent toolbox for assessing protein location and function. *Science*, 312(5771):217–224, apr 2006.

[56] Samuel T. Hess, Shaohui Huang, Ahmed A. Heikal, and Watt W. Webb. Biological and chemical applications of fluorescence correlation spectroscopy: a review†. *Biochemistry*, 41(3):697–705, jan 2002.

[57] Carlo Manzo and Maria F. Garcia-Parajo. A review of progress in single particle tracking: from methods to biophysical insights. *Reports on Progress in Physics*, 78(12):124601, oct 2015.

[58] Elizabeth A. Jares-Erijman and Thomas M. Jovin. FRET imaging. *Nature Biotechnology*, 21(11):1387–1395, nov 2003.

[59] Chen Y. Dong, Todd French, Peter T. C. So, C. Buehler, Keith M. Berland, and Enrico Gratton. Fluorescence-lifetime imaging techniques for microscopy. In *Methods in Cell Biology*, pages 431–464. Elsevier, 2003.

[60] Jennifer Lippincott-Schwartz, Erik Snapp, and Anne Kenworthy. Studying protein dynamics in living cells. *Nature Reviews Molecular Cell Biology*, 2(6):444–456, jun 2001.

[61] A. Mogilner, J. Allard, and R. Wollman. Cell polarity: Quantitative modeling as a tool in cell biology. *Science*, 336(6078):175–179, 2012.

[62] Sarah Erlemann, Annett Neuner, Linda Gombos, Romain Gibeaux, Claude Antony, and Elmar Schiebel. An extended γ-tubulin ring functions as a stable platform in microtubule nucleation. *The Journal of Cell Biology*, 197(1):59–74, 2012.

[63] R. Reyes-Lamothe, D. J. Sherratt, and M. C. Leake. Stoichiometry and architecture of active dna replication machinery in *Escherichia coli*. *Science*, 328(5977):498–501, 2010.

[64] M. Yano, K. Ono, T. Ohkusa, M. Suetsugu, M. Kohno, T. Hisaoka, S. Kobayashi, Y. Hisamatsu, T. Yamamoto, M. Kohno, N. Noguchi, S. Takasawa, H. Okamoto, and M. Matsuzaki. Altered stoichiometry of FKBP12.6 versus ryanodine receptor as a cause of abnormal ca2 leak through ryanodine receptor in heart failure. *Circulation*, 102(17):2131–2136, 2000.

[65] T. J. Morin and W. R. Kobertz. Counting membrane-embedded kcne β-subunits in functioning k+ channel complexes. *Proceedings of the National Academy of Sciences of the United States of America*, 105(5):1478–1482, 2008.

[66] J. D. Osteen, K. J. Sampson, and R. S. Kass. The cardiac iks channel, complex indeed. *Proceedings of the National Academy of Sciences of the United States of America*, 107(44):18751–18752, 2010.

[67] K. Nakajo, M. H. Ulbrich, Y. Kubo, and E. Y. Isacoff. Stoichiometry of the kcnq1 - kcne1 ion channel complex. *Proceedings of the National Academy of Sciences of the United States of America*, 107(44):18862–18867, 2010.

[68] Stefan W. Hell. Microscopy and its focal switch. *Nature Methods*, 6(1):24–32, 2009.

[69] Andrew M. Sydor, Kirk J. Czymmek, Elias M. Puchner, and Vito Mennella. Super-resolution microscopy: From single molecules to supramolecular assemblies. *Trends in Cell Biology*, 25(12):730–748, dec 2015.

[70] Timo Aspelmeier, Alexander Egner, and Axel Munk. Modern statistical challenges in high-resolution fluorescence microscopy. *Annual Review of Statistics and Its Application*, 2:163–202, 2015.

[71] Thomas A. Klar, Egbert Engel, and Stefan W. Hell. Breaking abbe's diffraction resolution limit in fluorescence microscopy with stimulated emission depletion beams of various shapes. *Physical Review E*, 64(6), nov 2001.

[72] Sebastian van de Linde, Anna Löschberger, Teresa Klein, Meike Heidbreder, Steve Wolter, Mike Heilemann, and Markus Sauer. Direct stochastic optical reconstruction microscopy with standard fluorescent probes. *Nature Protocols*, 6:991–1009, 2011.

[73] Paolo Annibale, Stefano Vanni, Marco Scarselli, Ursula Rothlisberger, and Aleksandra Radenovic. Quantitative photo activated localization microscopy unraveling the effects of photoblinking. *PLoS ONE*, 6(7):17436–17441, 2011.

[74] James R. Norris. *Markov Chains*. Cambridge University Press, 32 Avenue of the Americas, New York, NY 10013-2473, USA, 15th printing edition, 2009.

[75] Volker Buschmann, Kenneth D. Weston, and Markus Sauer. Spectroscopic study and evaluation of red-absorbing fluorescence dyes. *Bioconjugate Chemistry*, 14(1):195–204, 2003.

[76] Jerker Widengren and Petra Schwille. Characterization of photoinduced isomerization and back-isomerization of the cyanine dye cy5 by fluorescence correlation spectroscopy. *The Journal of Physical Chemistry A*, 104(27):6416–6428, 2000.

[77] Michael Hirsch, Richard J. Wareham, Marisa L. Martin-Fernandez, Michael P. Hobson, and Daniel J. Rolfe. A stochastic model for electron multiplication charge-coupled devices - from theory to practice. *PLOS ONE*, 8(1):e53671, 2013.

[78] Jürgen J. Schmied, Mario Raab, Carsten Forthmann, Enrico Pibiri, Bettina Wünsch, Thorben Dammeyer, and Philip Tinnefeld. DNA origami-based standards for quantitative fluorescence microscopy. *Nature Protocols*, 9(6):1367–1391, 2014.

[79] Tyler J. Chozinski, Lauren A. Gagnon, and Joshua C. Vaughan. Twinkle, twinkle little star: Photoswitchable fluorophores for super-resolution imaging. *FEBS Letters*, 588(19):3603–3612, 2014.

[80] Graham T. Dempsey, Mark Bates, Walter E. Kowtoniuk, David R. Liu, Roger Y. Tsien, and Xiaowei Zhuang. Photoswitching mechanism of cyanine dyes. *Journal of the American Chemical Society*, 51(131):18192–18193, 2009.

[81] Zahra Zolmajd-Haghighi and Quentin S. Hanley. When one plus one does not equal two: Fluorescence anisotropy in aggregates and multiply labeled proteins. *Biophysical Journal*, 106(7):1457–1466, 2014.

[82] George P. Anderson and Nandan L. Nerurkar. Improved fluoroimmunoassays using the dye alexa fluor 647 with the RAPTOR, a fiber optic biosensor. *Journal of Immunological Methods*, 271(1):17 – 24, 2002.

[83] Hari Shroff, Catherine G. Galbraith, James A. Galbraith, and Eric Betzig. Live-cell photoactivated localization microscopy of nanoscale adhesion dynamics. *Nature Methods*, 5:417–423, 2008.

Acknowledgments

PD Dr. Alexander Egner Thank you for giving me the opportunity to work in your group, thereby laying the foundation of this work. I am especially grateful for the scientific discussions in which you persisted in a clear analysis and a well based argumentation of mine, thereby expanding my rhetorical and cognitive skills.

Prof. Dr. Tim Salditt I am very grateful you accepted to be second referee, thereby enabling this work.

Prof. Dr. Axel Munk Your mathematical expertise was an irreplaceable requirement for the success of my work. You also happily offered to sit in my thesis committee. I am deeply grateful for both.

I also thank the other members of my thesis committee, namely **Dr. Rehfeldt**, **Prof. Dr. Jakobs** and **Prof. Dr. Ropers**.

Dr. Claudia Geisler Thank you for your never faltering supervision in which you never tired to listen, explain and help. You shared my delightment after a success and damped unhappy experiences such that working days got brighter. I am deeply grateful for the uncounted discussions of my work in which you exceled to complete the picture without receiving all pieces.

René Dear table neighbor, I owe you uncounted (bad) word jokes as well as mind breaking catchy tunes. There are many more reasons I am happy for my office companionship: Hints and practical help in Matlab, your willingness to repeatedly point out searched materials, unlimited supplies of coffee, cookies and tea; funny table games and finally none the less your kind personality. Let me partially repay my debt. What starts with E, ends with E, and has only one letter in it? Envelope. Got it?

Francesco Someone once acknowledged you as all-mighty PostDoc. You are indeed. Whenever I wanted to talk about some results you listened, however unrelated to your current task. I wish I'd have traveled more often the long way to your office to pick up some sweets and encouraging words.

Britta Thanks for your encouraging words, your excellent notes for preparing a talk as well as your interest in my work.

Julia Thank you for your willingness to execute a time consuming boring task. I also enjoyed our table football breaks.

Jennifer Thank you for your light hearted presence. I always smiled hearing a whistled tune coming from the floor.

Anne Hein Thank you for your explanations of mathematical problems regarding the drift estimation model as well as your kind and helpful attitude.

Thomas Staudt Your astonishing speed to master an alien Julia code has greatly helped to complete my work for which I am very grateful.

Dr. Alexander Hartmann I enjoyed our mathematical and non-mathematical discussions as well as your humor, regarding math, people and etc.

Dr. Timo Aspelmeier. This work greatly benefitted from your expertise to understand physical problems and foresee and solve practical ones regarding data evaluation and none the less to develop a counting Markov model. I extraordinary benefitted from our mathematical discussions which never failed to please due to your kind self.

Optical nanoscopy & LLG A big thanks is owed to my group, present and former members, for establishing a nice and helpful working environment. This also holds true for the whole LLG. Special thank goes to Uwe Lampe. You always ordered missing materials as fast as possible and shared several entertaining stories.

My family The best one could wish for. Without you this work would not exist. I am deeply grateful for having you all, especially my mother who always helped and believed in me. Special thanks to my brother for desired distractions and exhilarant talks.

My daughter Crown of my life. Your laugh in the morning is irreplaceable and never fails to lift my mood. I am deeply grateful you accompany my life.

My wife What shall I say? There is far too much to say and far too much I am not able to express in words. You enriched my life in various ways, gave me hold and managed to ease my mind even in the longest and darkest tunnel stemming from this work or anywhere else. This thesis owes you as much as me since I met you I experience the real meaning of balance. I owe you the happiest moments of my life.

Eidesstattliche Erklärung

Hiermit erkläre ich, dass ich die vorliegende Arbeit selbstständig angefertigt, nicht anderweitig zu Prüfungszwecken vorgelegt und keine anderen als die angegebenen Hilfsmittel verwendet habe. Sämtliche wissentlich verwendeten Textausschnitte, Zitate oder Inhalte anderer Verfasser wurden ausdrücklich als solche gekennzeichnet.

_____ Göttingen, den

Oskar Laitenberger

List of Publications

1. Alexander Hartmann, Stephan Huckemann, Jörn Dannemann, **Oskar Laitenberger**, Claudia Geisler, Alexander Egner and Axel Munk. Drift estimation of in sparse sequential dynamic imaging, with application to nanoscale fluorescence microscopy. *Journal of the Royal Statistical Society: Series B (Statistical Methodology),* 78(3):563-587, 2015.
2. **Oskar Laitenberger**, Timo Aspelmeier, Claudia Geisler, Axel Munk and Alexander Egner. Towards unbiased quantitative fluorescence microscopy. (in preparation)
3. Timo Aspelmeier, Alexander Egner, Claudia Geißler, **Oskar Laitenberger**, Axel Munk. Counting molecues in single marker switching micorscopy (in preparation)